Data-Driven Non-Intrusive Surrogate Modeling and Optimization of Selective Laser Melting Using Machine Learning Methods

by

SHUBHAM CHAUDHRY

MANUSCRIPT-BASED THESIS PRESENTED TO ÉCOLE DE TECHNOLOGIE SUPÉRIEURE IN PARTIAL FULFILLMENT FOR THE DEGREE OF DOCTOR OF PHILOSOPHY
Ph.D.

MONTREAL, AUGUST 2, 2023

ÉCOLE DE TECHNOLOGIE SUPÉRIEURE
UNIVERSITÉ DU QUÉBEC

BOARD OF EXAMINERS

THIS THESIS HAS BEEN EVALUATED

BY THE FOLLOWING BOARD OF EXAMINERS

Mr. Azzeddine Soulaïmani, Thesis supervisor
Department of Mechanical Engineering, École de technologie supérieure

Mr. Simon Joncas , Chair, Board of Examiners
Department of Systems Engineering, École de technologie superieure

Mr. Hakim Bouzid, Member of the Jury
Department of Mechanical Engineering, École de technologie superieure

Mr. Mohammad Jahazi, Member of the Jury
Department of Mechanical Engineering, École de technologie superieure

Mr. Francisco Chinesta, External Examiner
Department of Mechanical Engineering, ENSAM, Paris

THIS THESIS WAS PRESENTED AND DEFENDED

IN THE PRESENCE OF A BOARD OF EXAMINERS AND THE PUBLIC

ON "JULY 7, 2023"

AT ÉCOLE DE TECHNOLOGIE SUPÉRIEURE

ACKNOWLEDGEMENTS

I would wish to convey my earnest gratitude to my supervisor, Prof. Azzeddine Soulaïmani, whose expertise, counsel, and patience added considerably to my research experience. I appreciate all his efforts, especially in transferring his knowledge to me, adjusting my writing and supporting me financially during my Ph.D. I am thankful to him for believing in my accomplishments and providing me with every opportunity to assimilate. His encouragement helped me throughout my research study. I would also like to thank my colleagues Gullnaz Shahzadi, and Azzedine Abdedou for their constant support and motivation during my Ph.D. journey. Also, special thanks to my jury members Prof. Mohammad Jahazi, Prof. Hakim Bouzid, Prof. Francisco Chinesta, and Prof. Simon Joncas for evaluating my Ph.D. thesis, valuable feedback and suggestions.

Last but not least, I want to thank my parents, Mr. Siya nand, Ms. Urmila and my siblings Navneet Kumar, Dr. Shikha Choudhary, for their outstanding support, kindness, love and constant motivation throughout this journey. Their belief in me has been an endless source of motivation, and I owe much of my success to their presence in my life. I am really lucky to have you all.

To my parents, who have been my pillars of strength from the very beginning, I cannot thank you enough for your constant encouragement, sacrifices, and belief in my abilities. Your guidance and unwavering faith in me have been instrumental in shaping me into the person I am today. I am blessed to have you as my parents.

To my dear sister and brother, you have been my closest confidants and best friends. Your support, understanding, and encouragement have meant the world to me. Your willingness to lend a helping hand and provide much-needed breaks during stressful times have made this journey more manageable and enjoyable.

To my jiju (DSP. Prince Singhal) and bahabi (Dr. Damini), your presence in my life has been a wonderful addition to our family. Thank you for embracing me as your own and always being

there with your kind words and support. Your belief in my abilities has boosted my confidence, and I am grateful for the warmth and love you bring into our family.

I would also like to acknowledge the extended family members and friends who have been a source of inspiration and motivation during this journey. Your constant encouragement and well wishes have kept me going, and I am thankful for your presence in my life.

To everyone who has played a role in my journey, whether big or small, thank you from the bottom of my heart. Your love, support, and belief in me have been the driving force behind my success. As I embark on the next chapter of my life, I carry with me the lessons learned and memories created during this Ph.D. journey, and I am excited about the future that lies ahead.

French title

SHUBHAM CHAUDHRY

RÉSUMÉ

L'objectif de la thèse présentée est la modélisation numérique et l'optimisation du processus de fabrication additive (AM) par laser (Selective Laser Melting SLM). Les utilisateurs du procédé de fusion sélective au laser (plus généralement de fabrication additive) dépendent principalement des expériences pour comprendre et prédire les processus. Les techniques traditionnelles d'essai et d'erreur pour déterminer les résultats du processus d'AM pourraient être longues et coûteuses. De plus, la simulation numérique prend beaucoup de temps à calculer. Une nouvelle approche basée sur des techniques de l'apprentissage automatique (ML) pourrait contribuer à accélérer le processus de fabrication et réduire le coût d'exploitation.

Dans ce contexte, un modèle de simulation numérique du processus SLM a été développé à l'aide du logiciel ANSYS. Une nouvelle technique d'étalonnage des paramètres du procédé a été développée. L'efficacité du modèle numérique est évaluée et comparée à trois cas tests pour lesquels des données expérimentales sont disponibles. Les études expérimentales impliquent un prisme vertical, un prisme horizontal et une structure en forme de L. Un autre modèle numérique par éléments finis a été développé avec le logiciel ANSYS Workbench Additive pour modéliser une pièce fabriquée par le processus SLM et pour laquelle des données sont du domaine public. Afin d'analyser la sensibilité et la propagation des incertitudes des paramètres d'entrée, un modèle rapide dit de substitution a été développé. L'approche basée sur les données combine des techniques d'apprentissage automatique avec des simulations numériques d'haute-fidélité pour analyser plus efficacement le processus SLM et ce cadre peut être utilisé dans l'optimisation des processus. Les travaux de recherche ont considéré la vitesse du laser, l'éclosion, l'espacement, l'épaisseur de la couche, le module d'Young et le coefficient de Poisson comme paramètres d'entrée, tandis qu'à la sortie, les variables sont des prédictions de déformations normales dans la pièce fabriquée. Un modèle de substitution a été construit avec un réseau neuronal profond (DNN) et une expansion du chaos polynomial (PCE) pour créer une surface de réponse entre la sortie et les variables d'entrée. L'analyse a révélé que tous les paramètres étaient importants dans le processus. Par la suite, le modèle de substitution a été intégré avec des algorithmes d'optimisation non intrusifs (tels que les algorithmes génétiques (AG), l'évolution différentielle (DE) et l'optimisation des essais de particules (PSO)) pour effectuer une analyse inverse qui a aidé à trouver les paramètres optimaux. Parmi tous les modèles, le PSO a donné de bons résultats, et le modèle DNN s'est avéré être le modèle de substitution le plus efficace par rapport au PCE.

Une autre contribution de cette thèse est l'introduction de deux types de modèles réduits non intrusifs et fondés sur des données, le premier est nommé l'auto-encodeur convolutif-perceptron multicouche (CAE- MLP) et le deuxième est une combinaison de la décomposition orthogonale et de réseaux de neurones artificiels (POD-ANN). Le POD-ANN extrait la base d'ordre réduit à partir de la matrice des données d'haute-fidélité. Après cela, un réseau de neurones artificiels a été construit pour former un modèle de substitution entre la base réduite et les paramètres d'entrée. De même, le CAE-MLP utilise une méthode de convolution unidimensionnelle pour extraire une base réduite dite l'espace latent. Un modèle de régression basée sur un réseau de neurones multicouches (MLP) est construit entre les paramètres d'entrée et l'espace latent. L'efficacité et la précision de ces les méthodes sont quantifiées sur la base de l'analyse thermomécanique d'une pièce fabriquée. Une bonne comparaison entre les moments statistiques des résultats des simulations haute-fidélité et les prédictions des ROM confirment la capacité des méthodes proposées à prédire avec précision. De plus, les prédictions sont comparées aux résultats expérimentaux à différents endroits. Bien que les deux modèles aient montré une bonne corrélation avec les résultats expérimentaux, le modèle CAE-MLP s'est avéré plus performant que le modèle POD-ANN.

Mots-clés: Fusion laser sélective, Optimisation, Modélisation d'ordre réduit, Décomposition orthogonale propre, Auto-encodeur, Réseau de neurones profonds, Expension du chaos polynomial

Data-Driven Non-Intrusive Surrogate Modeling and Optimization of Selective Laser Melting Using Machine Learning Methods

SHUBHAM CHAUDHRY

ABSTRACT

The goal of the presented thesis is computational modeling and optimization of selective laser melting (SLM), which is an additive manufacturing(AM) process, using data-driven non-intrusive machine learning techniques. The selective laser melting process mostly depends on experiments to understand and predict the process. The use of traditional trial and error techniques to determine the AM process outputs could be time-consuming and costly. In addition, the numerical simulation takes a significantly longer time to compute. A new framework and techniques like machine learning (ML) are an urgent requirement of the AM industry to speed up the manufacturing process and reduce operational costs.

In this context, a numerical simulation model of SLM process was developed using the ANSYS additive software. To fasten the numerical convergence, a new calibration technique was developed, which not only improves the convergence but also improves the output results. The computation efficiency is assessed and compared with the three different experimental studies. The experimental studies involve a vertical prism, a horizontal prism, and an L-shaped structure. Later another SLM numerical model developed with ANSYS workbench additive, and a data-driven framework was proposed to analyze the sensitivity and uncertainty in SLM input and output parameters. The proposed data-driven approach combines machine learning techniques with high-fidelity numerical simulations to analyze the SLM process more efficiently and this framework can be used in process optimization. Research work considers laser speed, hatch spacing, layer thickness, Young modulus, and Poisson ratio as input parameters, while the output variables are normal strains predictions in the built part. A surrogate model was constructed with a deep neural network (DNN) and polynomial chaos expansion (PCE) to create a response surface between the process output and the input variables. The analysis found that all the considered parameters were important in the process. Subsequently, the surrogate model was integrated with non-intrusive optimization algorithms such as genetic algorithms (GA), differential evolution (DE), and particle swarm optimization (PSO) to perform an inverse analysis which helped in finding the optimal parameters setting for the building. Among all the models, the PSO performed well, and the DNN model was found to be the most efficient surrogate model compared to the PCE.

Another contribution from this thesis is the introduction of two data-driven, non-intrusive, reduced-order models (ROMs) named convolutional autoencoder- multilayer perceptron (CAE-MLP) and a combined proper orthogonal decomposition- artificial neural network (POD -ANN). The POD-ANN uses proper orthogonal decomposition-based, reduced-order modeling which extracts the reduced order basis for the given high-fidelity input snapshot matrix. After that, an artificial neural network was constructed to form a surrogate model between the reduced order bases and the input parameters. Similarly, the CAE-MLP uses a 1D convolutional autoencoder for the reduction of a high-fidelity spatial dimension snapshot matrix constructed from high-fidelity numerical simulations. The reduced latent space is projected to the input variables using a multilayer perceptron (MLP) regression model. The efficiency and accuracy of these methods are quantified based on the thermo-mechanical analysis of an AM-built part. A good comparison between the statistical moments from the high-fidelity simulation results and the ROMs predictions confirms the ability of the proposed methods to accurately predict the SLM outputs. Additionally, the predictions are compared with the experimental results at different locations. While both models have shown a good correlation with the experimental results, the CAE-MLP performed better than the POD-ANN.

Keywords: Selective laser melting, Optimization, Reduced order modeling, proper orthogonal decomposition, Autoencoder, Deep neural network, Polynomial chaos expension

TABLE OF CONTENTS

Page

LIST OF TABLES

LIST OF FIGURES

LIST OF ALGORITHMS

LIST OF ABBREVIATIONS

AM	Additive Manufacturing
LPBF	Laser Powder-Bed Fusion
SLM	elective Laser Melting
CAD	computer-Aided Design
DOE	Design of Experiment
LHS	Latin Hypercube Sampling
PCE	Polynomial Chaos Expansion
DNN	Deep Neural Network
GA	Genetic Algorithms
DE	Differential Evolution
CAE-MLP	Convolution Autoencoder
ROM	Reduced-Order Model
ML	Machine Learning
PSO	Particle Swarm Optimization
SSF	Strain Scale Factor
ASC	Anisotropic Coefficients
UA	Uncertainty Analysis
SA	Sensitivity Analysis
NIST	National Institute of Standards and Technology

CAE-MLP	Convolutional Autoencoder- Multilayer Perceptron
POD-ANN	Proper Orthogonal Decomposition based Artificial Neural Network
MSE	Mean Square Error

LIST OF SYMBOLS AND UNITS OF MEASUREMENTS

ρ	Material Density
c_p	Specific heat capacity
k	thermal conductivity
P	laser Power
A	Powder Material absorpitivity
S_n	Sensitivity indices
g	activation function
p	Order of Polynomial
a_α	polynomial expansion coefficient
$\delta_{\alpha\beta}$	Kornecker Symbol
d	Matrix rank
V	POD mode
ν	POD project coefficients
$\|\|.\|\|_2$	L^2 norm
σ	non linear activation function
φ	probability density function
α^*	new input variables
f	Kernal size
$F_{x_{eco}}$	Space encoder
$F_{x_{deco}}$	Space encoder

INTRODUCTION

Additive Manufacturing(AM) is one of the growing manufacturing techniques- that provides an opportunity to construct a complex and customized geometry with significantly less material wastage (Aboutaleb *et al.*, 2017). In the early stage, AM was known as rapid prototyping or 3D printing because it was mostly used to build prototype designs. However, later, it was realized that the technology could produce a fully functional part, and that is how the term 'Additive Manufacturing' became popular (Gu, Meiners, Wissenbach & Poprawe, 2012). AM process decimates the traditional forms of manufacturing like moulds, dyes, milling and machining etc. Furthermore, AM encompasses a wide range of materials ranging from plastic, composites, metals, and many more. Nowadays, the most recent and advanced AM system, Laser-Based Additive Manufacturing (LBAM), also known as a Laser Powder-bed Fusion (LPBF), is widely used to fabricate geometrically complex metallic parts (Wohler, 2013). Due to the potential of working with different materials and the capability of design flexibility, there is a growing number of applications in various industries, especially aerospace and medical fields, for improving performance and reducing weight (Horn & Harrysson, 2012).

In the context of LBAM, especially Selective Laser Melting (SLM) can achieve up to 99% density in a built part with the help of fine features (Wang, 2012), and it can use a wide range of alloys. In SLM, a 3D model is manufactured by selectively melting the material powder layers with a high-energy laser beam. The structure of each layer is a 2D cross-section of the main computer-aided design (CAD) model. Every layer incorporates line tracks which are deposited adjacent to each other. Therefore, unlike the conventional manufacturing methods, the SLM process makes products straight from the digital copy without acquiring the tool and the fabrication sequence.

As SLM provides new opportunities, process optimization is ideal for SLM because it can help achieve high-performance design and fully utilize the fabrication freedom provided by the AM. Additionally, process optimization can help reduce the AM process's limitations by reviewing the manufacturing constrain in the design phase and the mechanical properties, such as proper compensation of the final AM part deformations and cutting down the residual stresses in the processed part. The quality of the built part depends on the material properties, the process parameters and the surrounding environment. Thus, a large number of parameters (around 19) could affect the final constructed structure, which poses a significant challenge to the building process. So, by optimizing these SLM process parameters, the residual stress and deformations can be reduced.

0.1 Research Challenges

Even though LBAM has many advantages, its low build quality and poor process reliability remain a great weakness for LBAM and limit its widespread commercial applications. Depending on the material type and the process inputs, the major quality issues for LBAM-constructed parts are inaccurate geometry, high surface roughness, improper relative density, and poor mechanical properties (e.g. tensile strength). In this research, a new framework and methodology are developed to optimize the LBAM process to find the set of optimal parameters that improve the LBAM product quality, such as tensile properties, porosity and geometric characteristics.

Chapter 2 presents an extensive literature review regarding the effect of input parameters on the LBAM process outputs. It is found that many process variables, namely laser speed, hatch spacing, laser diameter, layer thickness, laser power, and scan pattern, can influence the construction process and the final fabricated part quality. Additionally, the high-temperature gradient during the heating and cooling process gives rise to residual stress, leading to the improper shape of the built product and sometimes the immature termination of the building process. The process involves various time and length scales, making the LBAM complex. For example, the steep increase in the melt pool's temperature takes a few seconds and milliseconds to interact between the laser beam and the material powder. Whereas a layer's heating takes minutes, the global heating treatment during fabrication can take hours. Hence, it is difficult to identify an optimal set of process variables due to the high dimensionality of parameter space. This challenge becomes complicated considering the interaction between the process parameters. In other words, one variable's effect is connected with another process variable's effect. Moreover, the multi-physic of the thermo-mechanical process is very complex, and a mathematical relation between the process parameters and the properties of the built part is not known.

The majority of relevant research studies use an extensive experimental approach to find the optimal process parameters. However, studying the process parameters and their mutual interactions becomes impossible as the AM experimental process is very costly and time-consuming. So, it is not recommended to use Design of Experiment (DOE) methods (e.g., full factorial, fractional etc.). Another problem with this approach is that the optimal parameters of one process cannot be applied to another similar process because of the different experimental conditions (like material powder, machine type etc). Therefore, there is an urgent requirement to develop a global optimization framework which can construct a relationship between the input variables and the desired properties of the final built part. It is also required to speed up the optimization process by leveraging existing studies.

Numerical models provide an alternative to experimental methods, and many research studies have cited them. A numerical process can help us generate a large number of data sets at a significantly lower cost than traditional experimental models. However, SLM involves complex multiphysics and multiscale phenomena (Horn & Harrysson, 2012) with several uncertainties, from the material powder bed to the melting and solidification processes. These uncertainties come from an insufficient understanding of the process, measurement, scaling, sampling errors, and lack of information about the material properties(Ngo, Kashani, Imbalzano, Nguyen & Hui, 2018). Additionally, the discretization of the SLM problem needs a fine spatial mesh and requires a large number of time steps. The overwhelming requirements for computational resources make high-fidelity simulations too expensive in the context of optimization and uncertainty quantification. These challenges can be overcome with the use of data-driven surrogate modelling. The surrogate method approach works in two stages 1) A dataset of solutions matrix computed for several input samples in the offline stage that allows a surrogate model to be obtained using a regression approach; 2) predictions on the new data set are performed online stage using the surrogate model. The data-driven approach does not require any modification of the high-fidelity source codes; these are used as a black box. However, the solutions database should be computed in a reasonable timeframe.

0.2 Thesis Objectives

The primary aim of this work is to form a system for uncertainty propagation and optimization for SLM. This structure can help researchers and industries take full advantage of SLM by providing information about deformations, residual stress, temperature profile and process optimization.

To fulfill these requirements, the objectives for this research work are as follows:

1. Develop a preliminary structure for numerical modeling and optimization of SLM.
2. Build a computational numerical model to understand the SLM process better and validate the results with the experimental results.
3. Investigate new mathematical approaches to speed up the SLM simulation process to predict the mechanical properties of the built part.

4. Implement a non-intrusive surrogate model for the stochastic processing of the output from the SLM model and construct a map between the input and the output parameters.
5. Construct a non-intrusive data-driven surrogate framework to analyze the SLM process's uncertainty propagation and implement a suitable sampling technique (like: Latin hypercube sampling (LHS))to achieve this goal.
6. Conduct a sensitivity and uncertainty analysis with the SLM input variables and find the most critical parameters to the process.
7. Propose an optimization technique and find the SLM process's optimal parameters.
8. Implement a new data-driven framework using a reduced order non-intrusive surrogate approach to analyze a dataset of high-fidelity solutions computed at large nodes during the SLM process. Also, compare the predictions with experimental results.

0.3 Proposed Approach

The methodology and framework proposed in the research significantly contribute to analyzing the uncertainties and sensitivity and optimizing the SLM process. Following are the significant contributions and originalities presented in this thesis.

1. After an extensive survey, a 3D numerical model of the SLM process is constructed using the Workbench additive and Ansys additive software. The validation of the simulations was performed by comparing the simulation results with the experimental results.
2. In this research, two different sampling techniques, Sobol and LHS, have been used to conduct uncertainty and sensitivity analysis and optimize the SLM process. A Monte Carlo method is also used to find the number of samples required to perform these statistical.
3. As an original contribution, a new numerical model for the better convergence of the Ansys additive model was developed. The new convergence technique provides better results and significantly reduces the computation time. The results obtained from the new method were

validated with the experimental results. This work has been published in the following journal: International Journal of Manufacturing Research https://doi.org/10.1504/IJMR.2022.127090

4. Secondly, the additive model was used to build high fidelity data matrix of numerical solutions from the SLM simulations. A random set of input parameters was generated using the Sobol sampling method, and the built part's mechanical properties (like strains and deformations) were extracted as output over a cross-section. The obtained output data matrix was then used to construct a surrogate model between input and output parameters using the Polynomial chaos expansion (PCA) and Deep Neural Network (DNN). Surrogate models were combined with non-intrusive optimization algorithms such as genetic algorithms (GA), differential evolution (DE), and particle swarm optimization (PSO) to perform an inverse analysis and find the optimal parameters for the SLM process. The work has been published in the following journal: Applied sciences https://doi.org/10.3390/app12052324
5. In the continuity of previous work, a data-driven, non-intrusive, reduced order model (ROM) constructed with the convolution autoencoder (CAE-MLP) and the linear reduced-order technique-based artificial neural network (POD-ANN) has been proposed for additive manufacturing (AM) process. The research considers the whole geometry nodes to construct the high-fidelity matrix instead of cross-sections. The performance of both models was compared with the experimental results and the results from the second paper. The new framework significantly improved the predictions and increased the accuracy by 60% -80%. The third publication with the new approach has been submitted to Computer and Mathermatics with application on May 11, 2023 for evaluation by the journal.
6. Finally, the development of the SLM simulation model and the stochastic analysis techniques allows a more reliable prediction that accounts for the variabilities in the input parameters. These frameworks and tools help speed up the SLM computation and build trust in the SLM part before going to the actual production.

0.4 Thesis Organizarion

This thesis is presented in the format of articles with four chapters. A chapter dedicated to the literature review and two articles have already been published, presented in chapters 2 and 3. Article 4 has been submitted to a journal for evaluation and is presented in chapter 4.

Chapter 1 provides a comprehensive review of AM process, SLM mathematical modelling, different numerical software, uncertainty and sensitivity analysis of AM process, the effectiveness of process parameters on the AM output, surrogate modelling of AM systems, optimization of AM process, optimization techniques and reduced order modelling. Chapter 2 illustrates the mathematical modelling of the SLM process using Ansys additive and presents a new convergence method for faster and better SLM simulation results. In Chapter 3, a parametric analysis of the SLM process is carried out using Sobol sampling with the help of workbench additive software. A systematically data-driven, non-intrusive surrogate model is constructed between the input and output parameters. The surrogate model is then used to conduct the uncertainty and sensitivity analysis of the SLM-built part. The framework presents two different techniques using a convolution autoencoder and proper orthogonal decomposition. The framework helped in finding the essential parameters in SLM building operation and then used those parameters to find the optimal solutions using a suitable optimization technique. Chapter 4 is dedicated to the development of a reduced-order model (ROM) method for the SLM-built part. The prediction from both models was compared with the experimental results at different locations and with the projections from the surrogate model constructed in the third chapter. Finally, the concluding remarks and the future works are listed.

CHAPTER 1

LITERATURE REVIEW

This chapter provides a comprehensive introduction to the general Additive Manufacturing (AM) process and its different types, with a specific focus on the Laser Based Additive Manufacturing (LBAM) process. The numerical modelling of the LBAM process being specific to Selective Laser Melting (SLM), the effect of process parameters, surrogate modelling of the SLM method and optimization techniques for the SLM have been highlighted.

1.1 Additive manufacturing

Additive manufacturing provides a new way of part fabrication. It fabricates components directly from a 3D computer model by selectively curing, depositing or consolidating material layers with the successive layer. Every layer is a representation of the cross-sectional geometry of the built part at a given height. These techniques provide a construction method other than the traditional manufacturing sources like forming. Casting and machining as it doesn't require tooling to produce a component. Thus additive manufacturing is changing the way we construct parts in the manufacturing industries. Some of the major advantages of AM process are as follows:

1. Components with complex geometry like internal channels, lattice structure and many other properties can be fabricated.
2. It reduces material wastage and can save industries a lot of money.
3. The number of resources required in the construction process has been significantly reduced.
4. It provides customers with the freedom to get a personalized product in a short period of time and thus, it increases the production demand.
5. The product can be manufactured where needed, reducing the transportation cost significantly.

There are mainly seven major categories of AM techniques depending on the processing mechanism. These categories are defined in the following sections.

VAT Photopolymerization: Vat Photopolymerization constructs a structure layer by layer using a vat of liquid photopolymer resin. During the process, ultraviolet (UV) light is used to harden the resin while depositing a layer. When the layer is cured, the substrate moves the object made downwards for the deposition of new layer deposition (Skoog, Goering & Narayan, 2014).

Material Extrusion: Material extrusion uses a thermoplastic material as the primary material for the construction process. The process is famous for materials like polylactic acid (PLA), Acrylonitrile Butadiene Styrene (ABS) etc. The material filament is heated in the chamber and fed through a heated coil known as an extruder head. The molten material is moved out of the nozzle using hydraulic pressure, and it is deposited on the building plate. Once the deposition of a layer is completed, the extruder and the platform are parted away, and the platform is moved lower for deposition of the next layer (Gibson *et al.*, 2021a).

Material Jetting: Material jetting creates a 3D structure by ejecting material droplets from the heated nozzle; the process is similar to 2D inkjet printing. The droplets are deposited on each other layer by layer. As the process requires material to be in a droplet form, the number of suitable materials for the procedure are limited. Polymers and waxes are ideal for the process due to their viscous nature, and they turn into drops quickly (Gülcan, Günaydın & Tamer, 2021).

Binder Jetting: Binder jetting is similar to the material jetting process, droplets from the heated nozzle are deposited, but the droplets are not made of the material of the actual part to be printed. The droplets comprise a particular binder selectively deposited over the material powder bed to construct a 3D structure layer by layer. The commonly used material in the process is sand, ceramics and metals that come in a granular form (Ziaee & Crane, 2019).

Sheet lamination: In sheet lamination, the material sheets are bounded together layer by layer to form a 3d object. It uses various materials like paper, polymers and metals, but each requires a different binding process. For example, a paper sheet involves heat and pressure to bind two sheets coated with an adhesive. Similarly, heat and pressure are added to melt the sheets together for polymers. For metals, the sheets are joined together using ultrasonic vibrations with the proper pressure (Gibson *et al.*, 2021c).

Direct energy deposition: A direct energy deposition is a group of AM processes where the material powder and heat input are added simultaneously over the building plate. The heat source can be a laser, electron beam or plasma etc, where as the material can be a metal powder or wire (Ahn, 2021).

Powder Bed Fusion Process: In the powder bed fusion (PBF) process, material powder (stainless steel 316L) is selectively fused together layer-by-layer into a 3D structure. The powder bed fusion can be broadly classified as: i) direct metal laser sintering (DMLS); ii) selective electron beam melting (SEBM); iii) selective heat sintering (SHS); iv) selective laser melting (SLM); and v) selective laser sintering (SLS). The heat source in the fusion process can be either a high-intensity laser or an electron beam. Selective laser melting (SLM) uses a laser beam as the heat source and selective electron beam melting (SEBM) utilizes an electron beam as the heat source. SLM is slower than SEBM but provides a better surface finish than SEBM. In addition, SEBM can be used with fewer metal powders than SLM. DMLS is similar to SLS but uses metals instead of plastics (Gibson *et al.*, 2021b).

1.2 Selective laser Melting (SLM)

The SLM process is comprised of four major phases: i) conceptualization; ii) pre-processing; iii) manufacturing; and iv) post-processing. The conceptualization and pre-processing phases create a geometry of the component in a computer using some software, such as ANSYS-Additive. Based on the pre-specified layer thickness, the constructed geometry is then transformed into several slices, usually from 20 to 100 micrometres thick, and subsequently converted into a machine-friendly file format (.stl). A thin metal powder layer is evenly distributed over the substrate plate that moves in the vertical direction (z-direction). When the component is in the manufacturing phase, each layer is melted one by one using a specific scan strategy. Once the melting of a layer is complete, the processing platform is reduced by one layer of thickness. A new layer of the powder is applied over the previous layer using a roller or a rake, and the heating process is continued. These steps are repeated until the desired structure is produced. After completion, the component is removed from the base plate for post-processing, where

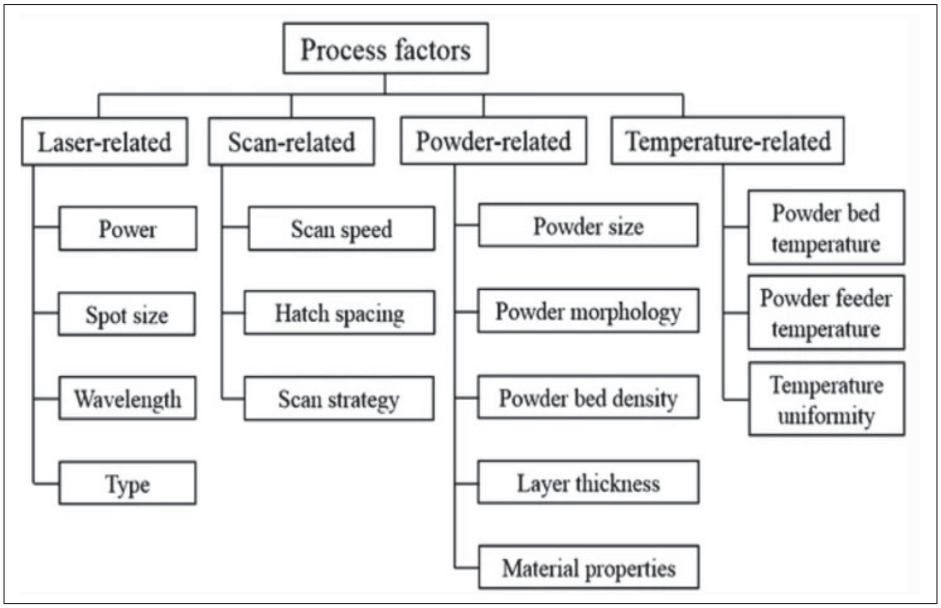

Figure 1.1 SLM process

the quality of the product is examined using neutron diffraction or a similar technique. The physical properties, such as absorption/reflection, phase transitions, melt pool dynamics and others, influence the quality of the final component an the stability of the process. The following subsections highlight the essential aspects of the SLM process and the challenges associated with its computational modeling.

1.2.1 SLM Process Variables

The efficiency and accuracy of additive manufacturing can be improved by using suitable material and process parameters. Broadly, the properties of a material, the process, and the environment define a large number of the parameters which affect the final product (Gu *et al.*, 2012), including laser speed, layer thickness, hatch spacing, laser diameter, chamber temperature, etc. Besides this, the scan pattern, for instance, a chess board, strip, etc., determine the final properties of the built part. Setting up a proper parameter setup is a tedious job, but it is essential to build a design geometry as the microstructure, geometry shape, mechanical properties, deformations, surface roughness etc, can be affected by the process parameters (Tapia & Elwany, 2014).

1.2.2 SLM Defects and Imperfections

The SLM process is highly complex; the physic behind the process consists of many phenomena's microstructure evolution, melt pool dynamics, rapid heating and cooling of the powder bed, absorption and reflection of the laser beam by the material powder and material evaporation (Li, Liang, Liou & Park, 2018) etc. The constant heating and cooling with high thermal gradient give rise to the residual stresses in the built part, leading to deformations, cracks, porosity and dimensional inaccuracy, etc (Zhang, Li & Bai, 2017). In (Zaeh & Branner, 2010) (Kruth *et al.*, 2010) a T-shaped cantilever and a bridge structure were constructed with the SLM. Both the structures showed deflections in the geometry once they were cooled down to ambient temperature and the supports were removed. Sometimes the building part can break from the substrate during fabrication due to internal stresses (Wang, Yang, Yi & Su, 2013). Aboulkhair, Everitt, Ashcroft & Tuck (2014) proposed a process map to get the high-density parts with AlSi10Mg alloy. The work demonstrated the correlations between the laser speed, laser power, and the porosities types. Similarly, many studies have been conducted in the past to find a relation between the process parameters and the properties of the built part to improve the quality of construction (Salem, Carter, Attallah & Salem, 2019) (Delgado, Ciurana & Rodríguez, 2012).

1.2.3 Materials processed by Selective Laser Melting

The majority of the SLM work uses metals like iron, titanium and nickel, because of their large applications and material cost. But as research progressed, different types of metal such as tungsten, copper, aluminum and magnesium have also been used for the SLM process. One of the famous metal alloys is 316L stainless steel which was first considered by (Abe, Osakada, Shiomi, Uematsu & Matsumoto, 2001) in 2001 but couldn't produce the desired results because of the balling effects. Later on, Jandin, Bertin, Dembinski & Coddet (2005) successfully reported SLM products with 316L stainless steel powder. The experiments found that low laser power and high scanning speed result in partial melting of the material powder; thus, it leads to high porosity components. However, it can be overcome by increasing the laser power and decreasing the scanning speed. Finally, in 2010 (Tolosa, Garciandía, Zubiri, Zapirain & Esnaola,

2010) achieved 99.9% relative density in the SLM process with the 316L stainless steel powder. Other variants of steel have been used and investigated by SLM, including M2 high-speed steel (tool steel), H13 tool steel, 314S stainless steel, inox904L stainless steel. AISI maraging 300 steel etc. Besides steel, iron and titanium-based alloys have also been reported by SLM like: Fe-Ni-Cr Fe-Ni-Cu-P, Fe-Al, Fe-Ni, Fe-Cr-Al Ti-6Al-7Nb, Ti-24Nb-4Zr-8Sn, Ti-13Zr-Nb, and Ti-13Nb-13Zr alloys. Another popular alloy is nickel-based and most of the research work is centred around Inconel, a nickel-based alloy family, mostly required in high-temperature applications. Some of the highly used nickel alloys are Inconel 625, Inconel 718, IN738LC, MAR-M 247, Chromel, Hastelloy X, and Nimonic 263 (Yap *et al.*, 2015) etc.

1.2.4 SLM post processing

The final step in the SLM process is post-processing, where the built part undergoes support removal, heat treatment and surface finishing. There could be two types of supports during the building process: the natural support provided by the material powder surrounding the building part and the stiff structures built alongside the actual geometry to give extra stability to the built part. The part could be removed easily from the powder supports, but the rigid supports must be removed from the part during the post-processing. Once the supports are removed, the surface still has some irregulates and to improve the surface quality, the SLM surfaces are treated by several methods like shoot peening, sand blasting, chemical polishing, Barrel finishing, electropolishing and grinding (Boschetto, Bottini, Macera & Veniali, 2020) (Löber, Flache, Petters, Kühn & Eckert, 2013). In post-processing the structure undergoes heat treatment too. The heat treatment can potentially reduce the residual stresses in the final structure and improve the product's capabilities (Baghi, Nafisi, Hashemi, Ebendorff-Heidepriem & Ghomashchi, 2021).

1.3 Computation modeling of SLM process

Understanding the SLM process and the effect of its input variables on the output using a traditional experimental path could be very expensive and time-consuming. Therefore SLM computational modeling has been introduced to study the SLM process. This will not only boost the SLM process understanding but will help us optimize the process too.

1.3.1 Analytical solutions

An analytical method for a moving heat source was first introduced for welding by Rosenthal and after some time, the heat source model is modified to a 2D Gaussian distributed heat source model (Huang, Khamesee & Toyserkani, 2016). Thijs, Kempen, Kruth & Van Humbeeck (2013) used the moving Gaussian heat source and provided an analytical solution to the thermal field. However, this model has limitations, and one of the major drawbacks is the oversimplification of the SLM physical mechanism. The model considered only the thermal conduction phenomena, and thus, it could not provide accurate results for a complex problem like SLM. (Peligrad, Zhou, Morton & Li, 2001) presented an analytical solution for melt pool depth during laser glazing, which matched the experimental results. But the prediction seemed to be accurate for a short range of parameters. King *et al.* (2014) proposed a normalized enthalpy that helps identify the transition between the conduction mode and the keyhole model. (Liu, Fang & Lei, 2021) later used the normalized enthalpy to predict the melt pool depth by considering the laser absorption behaviour. However, the model seems weak if the material properties change a lot. (Yang & Ayas, 2017) suggested a new analytical model for rapidly predicting the melt pool geometry and characterizes the depression shape formed under the influence of surface tension thermal dynamics and recoil pressure. A semi-analytical thermal model for LPBF process was proposed by Yang, Knol, Van Keulen & Ayas (2018) (Ning *et al.*, 2019) to study the influence of powder bed dimension and the related boundary conditions, which were solved using the finite difference method. Ning *et al.* (2019) introduced an analytical model with the pseudo heat sink and found a good match of melt pool dimensions with the experimental results. Moreover, the deformation induced due to the residual stresses was calculated using the analytical and finite element method (FEM) (Afazov, Denmark, Toralles, Holloway & Yaghi, 2017) (Gusarov & Kovalev, 2009). The proposed models can provide promising analytical results for thermal simulations, but they rely on FEM for mechanical simulations. Also, in some cases, the melt pool might not be in conduction mode or the material properties can be temperature dependent (Körner, Attar & Heinl, 2011), and in that case, the analytical model will need more validation proof.

1.3.2 Powder level modelling

SLM is a complicated process as it includes multiple physics: heat conduction, heat convection, radiation, photon absorption, hydrodynamics, phase change dynamics and solid mechanics etc. Thus, some researchers study particle-level SLM models to investigate the melt pool dynamics and heat flow, that includes many details such as laser-ray through the powder particle, computation fluid dynamics (CFD) model. Some of the particle-level methods and the challenges associated with them are provided in the following sub-sections.

Powder absorptivity modeling: During the SLM process, the powder bed is exposed to a laser beam, causing the photons to be transformed into thermal energy. The surface is highly reflective so that most of the beam's intensity is reflected from the surface and only a small fraction of the photons are absorbed. Generally, the first few nanometers of a surface absorb most of the photons (Tveito & Bruaset, 2006). The powder bed's relative density and reflectivity affect thermal energy absorption. The energy absorption in the deeper of the powder layer is higher than the coefficient of absorption of the material due to the multiple reflections of the photons by the powder particles.

The popular model for laser absorption proposed by Schoinochoritis, Chantzis & Salonitis (2017) can be used for modeling thick and high-porosity metal powder and ceramic powders. However, the approach is inadequate for modelling low-porosity metal powder layers. The distribution of particle size, the laser beam's size and its profile are some factors that affect the absorption of the powder material. Diffusive radiation transported through metal powder and a volumetric heat source are two of the approximations used in Gursarov's ray-tracing method for calculating the absorption of a powder bed (Gu *et al.*, 2012). But the work neglects the incident ray's polarization and angular absorption dependency. The significant challenges in the ray tracing method are considering the power, the polarization and the reflection/refraction of each ray.

Melt pool dynamics: Melt pool dynamics can be interpreted using the powder scale or continuum approaches. The powder scale approach deals with the dynamics at a particle level. The major forces driving melt pool dynamics are capillary action and the Marangoni effect. Two other factors that strongly influence a melt pool are the evaporation pressure and the wetting ability of the powder in the last layer. Körner *et al.* (2011) developed a two-dimensional numerical method that considers a lattice Boltzmann (LB) (Tveito & Bruaset, 2006) model to analyze the SLM process at the powder scale. This method has been modified to incorporate the free surface boundary conditions that help to model the phase change, wetting and surface tension (Ziaee & Crane, 2019).

In another approach, the powder bed is treated as a continuum (Schoinochoritis *et al.*, 2017). Such simplification reduces the computational costs and complexity of the interface between the atmosphere and the powder material. However, the continuum approach does not model the surface tension or the wetting effects between the material and the atmosphere. The study of melt pool at the macroscopic level requires a solution of the heat equation, with the laser as an energy source term. Gusarov, Yadroitsev, Bertrand & Smurov (2007) studied the melt pool properties in a selective melting process of steel 316 and successfully predicted the melt pool length and circumference. His work shows that at 45W if the scan speed is reduced from 2.4m/s to 1.2m/s, the process is stabilized by increasing the contact area available to the substrate. Zäh & Lutzmann (2010) study the single-layer melting of 316L steel powder using a finite element model. Their model only includes the heat radiation from the upper surface and the thermodynamics of the heat source. Their study estimated the formation of melt balls by analyzing the length-to-width ratio at different scanning speeds and beam powers.

Heat source: Heat source modeling or temperature distribution modeling is an essential part of the SLM process, as most of the material properties, such as density, surface tension and heat conductivity, are temperature-dependent. The metal powder absorbs only a small amount of incident energy during the process, whereas the rest of the intensity is reflected (Fischer *et al.*, 2003). Throughout the process, it is vital to expose the material to the laser intensity for a sufficient time so that it melts appropriately and solidifies accurately. Different combinations of laser power and velocity may result in other physical and mechanical characteristics of the built part. For instance, higher laser power and higher laser velocity lead to a finer microstructure and a higher cooling rate. On the other hand, higher laser power combined with lower laser velocity introduces a lower cooling rate and a coarser microstructure.

The heat energy source can be classified as the area heat and the volume heat flux. If the heat flux is applied over the material's surface, it is known as area heat flux; if the flux is applied to a volume, it is termed as volume-related heat flux. In SLM, the heat flux is considered a function of space and time. To simplify the process, the scanning vector is modeled with a scanning area rather than the exact scanning path (Neugebauer *et al.*, 2014) and the thermal heat is applied over the whole layer to substitute the scanning path.

Porosity: Porosity occurs due to the presence of large temperature gradients. During the melting and solidification processes, inert gases such as Nitrogen and Argon trapped inside the molten pool fail to escape the melt pool, resulting in porosity. Using a numerical model at the powder scale makes it possible to predict and analyze the morphology and evolution of the residual porosity within a bulk material. Teng *et al.* (2017) studied the formation of porosity in cobalt-chromium components using the 3DSIM tool. Using the SLM technique, their model can accurately predict the porosity and metal pool trends in CoCr parts.

Bauereiß, Scharowsky & Körner (2014) studied the defect formation and propagation mechanism using SEBM and the LB model proposed by Körner *et al.* (2011). They compared cubes of Ti6Al4V manufactured with a laser scan speed of 0.8m/s at different laser beam powers against numerical results. With a beam power of 90W, channels of high porosity are observed across many layers. They found that inadequate melt depth and the random nature of a powder layer lead to irregularities in the melted layer. During the melting process, thermal diffusion is slower than the hydrodynamic motion driven by the surface tension. Therefore, the molten particles merge with neighbouring solid material.

Surface Roughness:

The irregularities present over the surface of a built component are known as surface roughness. They may be useful, depending on the final application of the component; for instance, in contact/coupling between bones and implants (Deligianni *et al.*, 2001). However, surface roughness is not always desirable, as it negatively affects the component mechanical properties, leading to cracks (Cansizoglu, Harrysson, Cormier, West & Mahale, 2008). The built orientation, an important factor affecting the AM component, also affects the surface roughness. Strano, Hao, Everson & Evans (2013) found that all the parameters that affect the heat distribution over the surface will also significantly affect the surface roughness of an SLM component. Their study also reveals the dependence of the surface roughness on the slope angle. Their results show that the roughness increases as the inclination angle increases from 0°. The roughness then remains constant between 5°and 45°, followed by a slight decrease in roughness between 50°and 90°.

Qiu *et al.* (2015) discovered that melt pool stability affects surface roughness the most. Marangoni forces and recoil pressure influence the melt pool stability. Their study also reveals that poor finish, high scan speeds and larger layer thickness affect the surface roughness. Panwisawas *et al.* (2015) used a finite volume (FV) model to study the dependency of melt pool motion and the surface structure in SLM-manufactured cubes. The simulation setup considered the laser power and velocity to be 400 W and between 2m/s and 4m/s, respectively.

1.3.3 Part level modelling

Although understanding the physics at the powder level is essential, the model used in these studies has a dimension of 1 mm compared to the AM part of 10cm. The part-level simulation requires the inclusion of the deposition process, and thus, it may not be feasible to use those methods to simulate a part-level model. Therefore, the exclusion of particle-level modelling can reduce the computation cost and to further reduce the cost, some other assumptions are taken into account.

A simple SLM process simulation involving a coupled thermo-mechanical analysis and a fine mesh may take considerable time to solve (Cheng, Shrestha & Chou, 2016). Numerous assumptions that can simplify the representation and accelerate the SLM process computations are possible. In specific scenarios, the convection of liquid inside the melt pool and the heat loss from the base plate is usually ignored (Zhang, Li, Li & Zhao, 2011) (Cheng *et al.*, 2016) (Dai & Shaw, 2006). In other cases, the evaporation of the metal is not considered during the solidification and heating process (Dai & Shaw, 2002) (Tolochko *et al.*, 2003) (Dai & Gu, 2014). During the heating of the metal powder layer, the radiation effect of the heat source and heat loss from the base plate is usually ignored. The inclusion of the radiation loss term increases the nonlinearity of the problem (Yin *et al.*, 2012) (Roberts *et al.*, 2009). In the part level or continuum approach, the fluid dynamics of the melt pool are usually ignored, and the simulation only considers the thermo-mechanical model. Such simplifications help to bypass the surface tension and the wetting effects between the environment and the melt pool.

The quality of products using SLM depends on the material, the machine parameters, and their interactions during the process. The major challenges associated with SLM are: 1) the complexity in formulating the problem – it may take significant time and effort to solve a simple SLM process; and 2) the variations in the results from one machine to the other and the differences in material properties, both of which make it difficult to generalize the SLM process. Mathematical modeling provides an essential means for understanding the procedure and the material behaviour.

The AM community has been using the finite element (FE) and finite difference approaches for SLM thermal simulations, with scenarios solved as 1D, 2D, and 3D problems. A 1D model has the clear advantage of reduced computing cost. In (Childs, Hauser & Badrossamay, 2004), the SLM process was simulated by a 1D FE using Bisphenol-a polycarbonate. That work examined the effects of primary parameters like beam velocity, scanning length and the laser beam spot size over the as-built part. The disadvantage of 1D is that it lacks the ability to provide enough details about the thermal behaviour. For example, studying thermal distribution in a melt pool would not be possible. A 2D model can provide more insights than 1D modeling. A heat transfer model considering radiation and convective factors with a single line scab layer of steel 316L powder was studied in (Aboulkhair *et al.*, 2014). A similar study was done in(Matsumoto, Shiomi, Osakada & Abe, 2002), where a 2D model of the SLM process of the single layer formation of a nickel layer is studied. That study shows the possibilities for and the locations of future cracks in the layer.

While 2D modeling is mostly used to study the melting in a single layer case, for multiple layers a 3D model provides better accuracy. 3D modeling of a heat source was applied for the first time in (Goldak, Chakravarti & Bibby, 1984). The temperature field was calculated using a finite element model (FEM) and the laser beam was modeled as a double ellipsoidal heat source. The ellipsoidal shape allows the size and shape of the heat source to be modified, which helps to model a shallow penetration welding process or the deeper penetration laser and electron melting processes. In (Kolossov, Boillat, Glardon, Fischer & Locher, 2004), a three-dimensional FEM model of SLS was constructed. The model incorporates the nonlinearity of the specific heat and thermal conductivity during the phase changes. An important challenge here is to simulate and monitor the transient temperature history, as this history is required in order to calculate the residual stress states and the thermal stress distribution during the process. In (Roberts *et al.*, 2009) a 3D model is developed to calculate the temperature field in the multiple layers of an SLM process using the element birth and death technique. In this technique, the elements are activated or considered in the simulation process only when needed. In the process, zones of high heat flux are modeled with a fine mesh and the mesh density is increased only in specific areas of high flux. Such techniques save considerable computation time compared to having the finer mesh everywhere.

The discretization of a problem domain is vital for accuracy and computational cost. It is well known that when a coarse mesh is used, it can reduce the computing time but may lead to a significant discretization error. While finer meshes can provide better accuracy, they often require much more time to solve. In such a context, it becomes imperative to choose an appropriate mesh size that reduces the computational time without adversely affecting the accuracy of the simulation.

The temperature gradients under a laser beam are extremely high, but a dynamic adaptive mesh refinement (AMR) scheme can be used in the simulation process to capture the temperature field correctly while moving (Afazov *et al.*, 2017) (Gusarov & Kovalev, 2009) (Pal *et al.*, 2016). A dynamic adaptive mesh scheme can provide more precise results than static non-uniform mesh (Berger & Oliger, 1984). Dynamic AMR is a robust approach that has been widely applied in the study of fluid dynamics and forge forming. A similar dynamic approach, AMR modeling, was developed by Patil *et al.* (2015) for the simulation of SLM additive manufacturing processes. AMR modeling includes a box of finer mesh representing a melt pool area that moves throughout the coarser mesh domain. While the box is moving, the properties of all the elements within the box are calculated using the previous elements. During the process simulation, the element quantity remains the same, which keeps the model size constant.

As stated earlier, it is important to know the transient temperature history of the melting powder layer, as this helps to calculate the residual stress and temperature distribution in the SLM product. In the thermo-mechanical modeling of the SLM process, J2-plasticity and a heat conduction model can be used to represent the mechanical behaviour.

The temperature can vary from 100°C to 2000°C in the SLM process. Such drastic changes in the temperature of the process affects the mechanical properties of the metal powder and makes it essential to use an efficient model for the cooling and heating cycles of the process (Fu & Guo, 2014). For example, for Titanium alloy the density of the powder bed decreases with the increase of temperature until the melting point, after which it starts decreasing sharply. An inverse relation of the powder density with the temperature change between the solid and the liquid state is presented in (Childs, Hauser & Badrossamay, 2005). Masubuchi (2013) showed how the thermal stress of a material depends on the temperature of the material. Additionally, all the physical properties and mechanical behaviours of powder particles and the same bulk metals are different (Gusarov & Kruth, 2005) (Gusarov & Kovalev, 2009). In numerous cases, the material properties are considered independent of temperature to minimize the computational time (Deligianni *et al.*, 2001) (Strano *et al.*, 2013). However, solid and powder material properties can be defined as a function of temperature (Cheng *et al.*, 2016) (Hussein, Hao, Yan & Everson, 2013). An overview of the thermo-mechanical modeling of the SLM process is presented in the following section.

1.3.4 Numerical Software

There has been a great advancement in the numerical modelling of SLM. A number of software has been available to simulate the SLM process and some of them are listed in table 1.1.

1.4 Data-driven non-intrusive modelling of SLM

AM is a highly complex process comprising electronics, optics, mechanics and material science. Due to such complexity, the AM-built product is affected by several factors like material properties, laser parameters, working environment, etc. The mathematical modelling of AM system becomes difficult because the related factors are from diverse perspectives and different stages. Also, the physical-based model are usually too complicated due to the uncertainties in the process parameters, which further requires high computation cost. Another challenge associated with the AM process is the integration of different digital models for other phenomena and at

Table 1.1 Available software for the SLM simulation

	description	**References**
3DSim/ Ansys additive	A software developed by Prof. Stucker and later acquired by ansys in 2017	www.ansys.com /products/structures/additive /manufacturing
Flow3D	An american based company which simulates different types of LBPF process	www.flow3d.com /products/flow3d-am/
Additive Works	Keller introduced it first for the SLM simulation	www.additive.works
Netfabb	Strong mesh operation ability Acquired by Autodesk	www.autodesk.com /products netfabb overview
Ansys	workbench ansys provide another simulation model for the LPBF process by combing the thermal and structural models of the ANSYS software	www.ansys.com /products/
Abaqus	Users built the LPBF models	Favaloro & Pipes (2017)
Comsol	Strong multi-physic simulation with part level and particle level simulation abilities	Masoomi (2018)
Comet	FE software developed at the International Center for Numerical Methods in Engineering	www.cimne.upc.edu
ALE3D	Particle-level model by Lawrence Livermore National Laboratory	Khairallah & Anderson (2014)
CUBES	Developed by Pan Computing LLC and acquired by Autodesk	Denlinger (2016)
Simufact Additive	Mainly based on the inherent strain method	www.mscsoftware.com /product /simufact-additive
Deal.II	Open-source code. Strong ability in the adaptive mesh that is necessary for the LPBF process simulation	Bruna-Rosso (2018)
Diablo	Thermo-mechanical simulation for LPBF	www.esi-group.com/ software-solutions/virtual-manufacturing /additive-manufacturing
ESI	France company particle simulation	

multiple scales in one united model (Smith *et al.*, 2016). Machine learning (ML) applications have been spread to a wide range of fields, such as computer since, aerospace, manufacturing and healthcare industries. The advancement of data storage and acquisition has increased the adaptation of ML system-based data-driven models to uncover complex relationships and hidden knowledge in digital manufacturing systems (Lasi, Fettke, Kemper, Feld & Hoffmann, 2014). The use of a reliable ML model and dataset can learn hidden patterns and reveal the important latent understanding, which can help process optimization, system improvement and quality control. Thus, many researchers have used data-driven ML algorithms to counter the AM process challenges, including process modelling, design optimization, energy management and in-situ monitoring. This section provides a comprehensive literature review on the application of ML models in AM process.

The SLM process is an essential branch of additive manufacturing for the metal industry. The applications of machine learning in SLM technology are divided into three phases. The first phase is the pre-process, which is termed a "digital phase"; it consists of file preparation and part design. The second phase is the "manufacturing stage," which includes in-situ monitoring and process parameters optimization. The final step is post-processing, where the mechanical properties and the built part's quality are analyzed. All these stages are discussed in the subsequent.

Digital phase: The design of the L-PBF part corresponds to the design concept for additive manufacturing(DfAM). Initially, at the design phase, most designers consider the design according to their experience and knowledge. Thus, the AM professional lacks advanced intelligent techniques to help explore the AM-enabled design field. Therefore to address this issue (Salonitis, Chantzis & Kappatos, 2017) proposed a hybrid ML approach for selecting design features at the conceptual stage in the AM process. The research considers the AM design features and the target outputs were classified into loading, objectives and properties. An SVM model was considered to train and predict the final cluster with the recommended AM design features for the process. Zhang, Yang, Dong & Zhao (2021). used a convolution neural network (CNN) and neural network (NN) to study the manufacturing abilities and the potential failure area with a specific build design for an L-PBF process. In another similar study, Andrew et al. presented a framework using variational autoencoder(VAE) and Ml techniques for the cantilever design optimization. The process consists of the long short-term memory neural network and VAE to transform the cantilever structures to a 2d latent space and make a surrogate model for the latent space corresponding to the topology optimization process. (Després, Cyr, Setoodeh & Mohammadi, 2020) used the NN model with the genetic algorithm (GA) to optimize the micro lattice architectures in AM. They used GA to generate data set for the micro-lattice structures and performed a finite element analysis model to calculate the corresponding mechanical properties. The generated data was used as a training set for the graph convolution network and asymmetric auto-encoder for constructing micro lattice structures. The framework was able to predict mechanical properties with an accuracy of 93.72% for a given micro lattices structure. In (Zhang, Harik, Fadel & Bernard, 2018a) the authors used K-means clustering method to generate an efficient build orientation. The stereolithography (STL) models were decomposed into k facet cluster using the k-means clustering method along with the Davies-Bouldin criterion. The normal vector of every facet normal cluster were considered a different build orientations and the optimal orientation was calculated with the statistical evaluation method.

In-situ monitoring: Currently, in-situ monitoring is the highly focused area of ML applications in AM process. The technology has grown rapidly and now it uses advanced equipment like thermocouples, photo-detectors, high-speed optical cameras and pyrometers etc. (Angelone *et al.*, 2020). In-situ, monitoring is acquiring data from the multiple sensors attached during the AM building process to provide first-hand product quality information. The analysis of real-time data during the manufacturing process helps increase the quality of the built product and reduce material wastage and manufacturing costs. However, the process of accomplishing accurate time control on the AM is still at the developing phase, irrespective of the availability of big, multi-modal and high-quality data. This could be because of the following reasons. First, it is still not documented which sensor data is most useful for implementation in control strategies. Secondly, ML methods require to consider that fused data exist, but they're only been implemented recently. Finally, the data fusion methods needed to accept that all the sensor data is unavailable or doesn't exist (Razvi, Feng, Narayanan, Lee & Witherell, 2019).

The data for In-situ monitoring is divided into three types: one-dimensional (1D) data like spectra, 2D data corresponding to images and finally 3D data such as tomography. During the high-temperature melting of material powder in the SLM process, plumes can be formed because of the ionization of metallic vapour in the melt pool. Also, the recoiled pressure could drive the liquid drop to move upward with high speed and thus creates spattering. Even though the formation of plumes and spattering interrupted the melt pool, they could give useful incites about the melting process. Therefore grasso et.al conducted an experiment where a set of 14 non-consecutive layers in SLM for the plume images were captured in IR image streams. Each image had a sampling frequency of 50 Hz and a spatial resolution of 320 × 240 pixels. The data set was analyzed using an unsupervised ML technique where the first four layers at the bottom were used to train the model and the rest of the 10 layers helped monitor the process with the help of a control chart. Zhang, Hong, Ye, Zhu & Fuh (2018b) proposed a vision framework with a high-speed camera to track the images during the SLM process's sequential melting of the powder layer. The work was based on finding valuable information on melt pool, spatters and plumes. The features were extracted based on the physical mechanism phenomena during the process, using the PCA method and the SVM classification. This framework achieved an accuracy level of 90.1% for quality-level classification. The convolution neural network(CNN) can correctly monitor the real-time building process with 92.5% accuracy without the h feature selection method. CNN models can learn features automatically from the raw data and are primarily used in image analysis. Caggiano *et al.* (2019) proposed a modified version of CNN called deep CNN (DCNN) that used a hierarchical structure for multilevel feature extraction during the online image detection in the SLM. Similarly, Scime & Beuth (2018) presented another advanced version of CNN called multi-scale CNN (MsCNN), which further improved the flexibility and classification quality of the traditional CNN methods for the anomaly detection process.

Acoustic signals provide another way to monitor the manufacturing process and have advantages over optical signal, like it can accurately provide a defect's location (Shevchik, Kenel, Leinenbach & Wasmer, 2018). Additionally, the 1D acoustic method is faster than the 2D image or 3D tomography technique. However, this process faces challenges due to the background noises, which are noticeable in AM process, especially in the SLM process. But, the challenges can be handled using ML-based monitoring and could provide good results. The acoustic signals generated from the plasma created during the powder layer melting have gained popularity for in-suite monitoring. The overheating or the underheating of the powder layer can cause a change in the plasma density. Thus the change in the plasma density and the pressure fluctuation during the melting process affect the acoustic intensity. Ye, Hong, Zhang, Zhu & Fuh (2018) used this principle, collected acoustic signal using a microphone, and combined it with the deep belief network (DBN) to analyze the melt tracts condition during the heating process. Shevchik *et al.* (2018) another way, using a susceptible fibre Bragg grating sensor and a sample rate of 1MHz to collect the acoustic signals for the SLM method.

Process parameters optimization:

The application of data-driven analysis in mapping the process parameters, final built part properties, and the performance of the AM process has multiplied. Even though the Finite element methods can accurately represent these relationships to some extent, the representation of AM process through high-fidelity modelling is complex. The numerical modeling of AM requires a deep understanding of material properties and the law of physics involved in AM process. On the other hand, the low-fidelity methods don't incorporate all the information related to the physical poperies, mainly because of the variability from material to material or machine to machine. Many studies have been conducted to introduce ML methods to counter these challenges in the optimization of AM process.

The earliest work of ANN use in process optimization was proposed by (Shen, Yao, Wang & Yang, 2004) to predict the part density in the built part. Xiong, Zhang, Hu & Wu (2014) used the ANN model to find the effect of process parameters on the part density of SLM built part. (Rong-Ji, Xin-Hua, Qing-Ding & Lingling, 2009) used this technique and combined it with the genetic algorithm (GA) to find the optimal parameters like laser speed, hath spacing, laser power, interval time and surrounding temperature to calculate the minimum shrinkage in the built part. In another similar study, (Hertlein, Deshpande, Venugopal, Kumar & Anand, 2020) introduced a new optimization framework to obtain the optimal process variables for the SLM process of Ti-6Al-4V material with the 98% material density of the built part. (Lo, Liu & Tran, 2019) studied the effect of hatch spacing and scan length on the melt pool temperature and depth in an SLM process of SS316L material. The studies find the optimal combination of the input variable and prove the capability of their technique with the experimental results.

During the melting building process, the melt pool properties like geometry, uniformity, and depth can influence the end product properties. So, a multi-layer perceptron was used to analyze the predict the melt pool dimensions for the powder fusion AM (Caiazzo & Caggiano, 2018) and the wire-based DED (Xiong *et al.*, 2014) process using the available experimental data points. The study concluded that a desired melt pool geometry can be achieved by controlling the input variable reversely. Tapia, Khairallah, Matthews, King & Elwany (2018) proposed a surrogate model with the Gaussian process (GP) to analyze the melt pool depth with the process parameters. The framework used 139 data points, some of which were collected from the in-house experiments and others from the publicly available literature. The study used ad-hoc filter to remove the outlier, providing 96 valid data points. The calculated error was 6.02μm which was under the acceptable limit. (Hertlein *et al.*, 2020) presented a technique to link the process parameters with the part properties with the help of a Bayesian network (BN). The research work considered laser power, scan speed, hatch speed and layer thickness as the input variables. In contrast, the ultimate tensile strength, yield strength, hardness, surface roughness and density were taken as the output variables. The analysis used data from different publications related to manufacturing AM parts built with 316 L material to train the BN model. The BN model was continuously trained and used to improve the accuracy.

Mechanical property and quality control

The major limitation to AM's large-scale production at the global level is the quality of the built product, which varies from machine to machine, even for the same process or build to build with one machine. These irregularities in the process may cause inaccurate geometry, process instability, product density and mechanical properties. Therefore extensive research has been carried out to monitor and improve AM-built quality using ML models.

Kusano *et al.* (2020) presented a prediction analysis for the tensile properties of a built part and their relation with the microstructural feature after the heat treatment. The research work includes the SLM process and the Ti6Al-4V alloy powder. The microstructures in the built part were observed using scanning electron microscopy(SEM) and micro-focus X-ray CT along the cross-section and parallel length, respectively. The ML-based regression model was used to predict the tensile properties based on the microstructure features. The model shows good prediction performance for yield strength and the ultimate tensile strength. (Özel *et al.*, 2020) proposed a framework with ML methods like ANN and generic programming to find the relation between the process parameters such as energy density and scan speed with the built part surface quality. The surface quality can influence the mechanical properties and corrosion resistance. In another similar study, Zouhri *et al.* (2021) used ML methods to predict the built part properties in SLM. The study used an SVM classifier and statistical features to analyze and predict the density in an SLM-built part. The analysis finds that SVM has an accuracy of 93% with the training set, whereas 99% with validation and 90% with the test set. Hassanin et al. introduced framework with deep learning method to predict mechanical properties of cellular structure built with SLM process by controlling the unit cell geometry.

Chowdhury & Anand (2016) used a feed-forward neural network(NN) to analyze and correct the geometry inaccuracies caused by the residual stress in a built part. The NN model was trained with the geometry inputs and the compensated point cloud. The model provides the optimized compensated point cloud, which is then post-processed to get new geometry inputs and used in the final printing process. (Zhu, Anwer, Huang & Mathieu, 2018) introduced an ML-based technique to model in-plane deviation in the AM process. A numerical relation was constructed between the designed and final geometry to capture the trend in shape deviation. A multi-task Gaussian process(GP) was used to understand the unexplained deviation data and model the local deviation. The presented methodology proved effective and provided 90% prediction accuracy. (Ferreira, Sabbaghi & Huang, 2019) proposed another approach to model the shape deviation using a Bayesian neural network and transfer learning technique for different geometries in AM process. (Samie Tootooni *et al.*, 2017) presented a using the spectral graph theory and ML techniques to analyze the dimensional variation in AM-built parts. The research work has proven to be effective in reducing the post-processing quality assurance burden. (Shen *et al.*, 2019) introduced a convolution neural network (CNN) technique to optimize the final built part geometry. In this technique, the 3D model was encoded into a probabilistic binary distribution and used as an input in the CNN to capture the deformation features, and then an inverse analysis was used to obtain a compensated geometry for the final built geometry.

Liu *et al.* (2020) predicted the porosity in the SLM built due to the physical effect of the process parameters. The study considers the effects of the process variables like energy density distribution instead of using the input variable directly to build the process porosity correlation model in AM community. Forming a fully dense built part has become a primary objective because it has the potential to influence the mechanical properties of the AM products (Lewandowski & Seifi, 2016). An MLP method can model highly complex and non-linear relationships, and the GP is capable of performing the uncertainty analysis, but it is very computationally expensive compared to MLP. So a combination of MLP along with the GP was coupled with the Bayesian methods to predict the porosity due to the effect of process parameters in SLM process (Tapia *et al.*, 2018). (Srinivasan, Swick & Groeber, 2020) integrated the ML regression methods with the physical-based methods for dimensionality reduction and optimization of the process parameters to build a more uniform part.

(Koeppe, Padilla, Voshage, Schleifenbaum & Markert, 2018) presents a framework by combing experimental studies with numerical simulation and deep learning(DL) methods to predict the maximum von mises and equivalent principal stresses in the SLM-built part. The study used experimental results to verify the numerical simulation and then the numerical simulation was used to generate a dataset, which was used to train the LSTM model. (Baturynska, 2019) developed ML-based methods for built-part mechanical properties(e.g. tensile modulus and nominal stress). The research work considers the geometry location, Orientation and the STL model properties as inputs. Zhang, Wang & Gao (2019b) proposed a neural network with the LSTM network to predict the tensile strength in the AM process built part. The LSTM model was used to process the temperature, vibration and sensing signals in the sequential inter-layer connections during the FDM process. The other variables like speed, layer height, temperature and material properties were used as an output for the ANN model and the outputs from the LSTM were used as the output for the ANN model to predict the final quality of the built part.

1.4.1 Deep neural nework

Deep neural networks (DNNs) are part of artificial neural networks (ANNs), similar to a human brain's neuronal system. The basic unit of an ANN structure is called a node, and it takes information from one end and passes to the next node from the other end. A DNN model contains three layers, with the first being the input layer and the last is the output layer. The layers between input and output are called hidden layers, which are more than one number for the DNN model. Each layer has a number of nodes or neurons connected with each other (Bishop & Nasrabadi, 2006). The node contains the values of inputs, sums their weighted values, and then uses an activation function to produce an output (Goodfellow, Bengio & Courville, 2016). An activation function is a nonlinear transformation over the input variables of each neuron that controls the activation of the neuron. The activation function performs an important role in the ANN model because if there is no activation function, then the model will be a linear regression and will not be able to learn the non-linear complex behaviours of the input and output parameters. Some of the primarily used activation functions are Sigmoid, Tanh and ReLU. The mathematical form of these activation functions is shown, and a simple structure of a deep neural network is presented in Fig. 1.2.

$$Sigmoid(x) = \frac{1}{1 + e^{-x}} \tag{1.1}$$

$$Tanh(x) = \frac{2}{1 + e^{-2x}} - 1 \tag{1.2}$$

$$ReLU(x) = max(0, x) \tag{1.3}$$

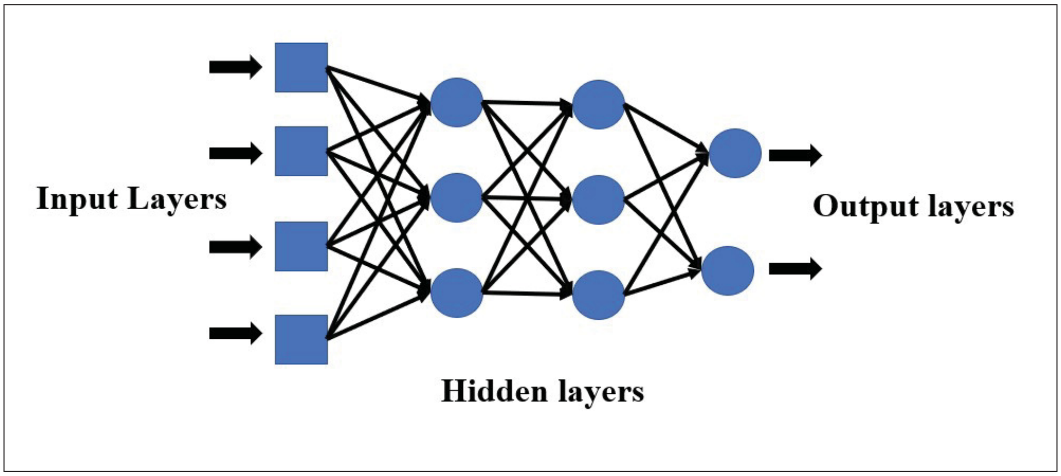

Figure 1.2 Representation of six layer DNN model

The AM community has widely used the ANN method to understand the relationship between process variables and the properties of the final built part. An ANN model can potentially represent the highly non-linear complex relations between the input and output parameters. A simple ANN model with one hidden layer but enough neurons can define any random function, but the optimal values of ANN parameters can lead to better results also, it protects the model from overfitting or underfitting. (Chen & Zhao, 2015) analyzed the effect of layer thickness, printing saturation, heater power ratio, and drying time on the dimensional accuracy surface roughness of the binder jetting process using the ANN network. Similarly in (Shen *et al.*, 2004) (Li, Dong & Zhang, 2009) (Kim, Shen, Nagy & Braatz, 2013) studied the effect of laser power, scan speed spacing, layer thickness, volume, bounding box, hatch spacing, scan mode and temperature on the density, dimension, built time, shrinkage ratio, density and tensile strength of the built selective laser sintering built part.

During the training phase of ANN, the values of each neuron are mapped to the next neuron with the help of some weights. The values are calculated using the following equation.

$$y(x) = f(w \odot x + b) \tag{1.4}$$

where x, w, b, $\odot$, f, y represent the input vector, weight vector, neuron bias, element-wise multiplication, activation function, and neuron output, respectively.To optimize the DNN network, we need to determine the optimal weights and biases by minimizing the loss function.

The form of loss function depends on the nature of the problem. For example, mean absolute error(MAE) and root mean square error(RMSE) represent the distance between two vectors and are widely used as loss functions. The mathematical form for both errors are:

$$RMSE = \sqrt{\frac{\sum_{i=1}^{n}(y_i - y_t)^2}{n}} \tag{1.5}$$

$$MAE = \frac{|\sum_{i=1}^{n}(y_i - y_t)|}{n} \tag{1.6}$$

Where i represents the sample index, y_i denoted the predicted value and y_t is the targeted value. Since the RMSE squares the error, the modeling will consider larger error compare to the MAE. Thus making RMSE a popular choice. In addition to protecting DNN from overfitting, a regularization term (λ) is added to the loss function shown below.

$$RMSE = \sqrt{\frac{\sum_{i=1}^{n}(y_i - y_t)^2}{n}} + \lambda \tag{1.7}$$

1.4.2 Polynomial Chaos Expansion

Polynomial chaos is the method used to compute parameter determination and surrogate modelling. The Polynomial Chao expansion was initially introduced by Wiener in 1938 for turbulence flow (Blatman & Sudret, 2010). The use of PCE became popular after the increased efficiencies of the computer due to the use of parallel computing. Later in the years, using PCE as a Hermite polynomial for linear elastic problems strengthened the use of PCE in different areas. Most recently the potential use of PCE as an uncertain model with an extended number of variables has been used in a variety of computational modeling of other fields like mechanical engineering (Prabhakar, Fisher & Bhattacharya, 2010), aerospace application (Hosder, Walters & Perez, 2006), chemical processes and computational fluid dynamics (Najm, 2009) (Nagy & Braatz, 2007). PCE could offer some advantages such as, it can use a small number of parameters hence it leads to better efficiency in utilizing experimental data, it has the ability to include information regarding the variable uncertainty and has an expansion structure which can further incorporate non-linear terms if the data needs.

In a PCE, a deterministic map, M, is considered such that $Y = M(X)$ where $x \in R^m$, $Y \in R^n$, m, and n define the input and output variables respectively. In order to simplify the equation, let us consider n to be 1 then the probability distribution of$X$ is provided by the probability density function $f_X(x)$ (Tan *et al.*, 2019). So the polynomial expansion of Y can be expressed as:

$$Y(X) = \sum_{\alpha=1}^{NP} a_\alpha \Phi_\alpha(X) \tag{1.8}$$

In the above equation, a_α is the expansion coefficient of $Y(X)$. The NP is calculated with the order of polynomial p and the size of input parameters m. Therefore, the value of NP is determined by $\frac{(m+p)!}{m!p!}$. The term Φ_α, denotes the orthogonal multivariant basis functions, with respect to the probability density function $f_X(x)$, such that:

$$\int_{R^m} \Phi_\alpha \Phi_\beta f_X(x) dx = \delta_{\alpha\beta} \tag{1.9}$$

where, δ_{α_β} is the Kronecker symbol. In the case of independent input variables, the values of Φ_α are obtained with the tensor product of the univariate orthogonal polynomials $\Phi^{\alpha}_{p_i}(X)$, as shown in the equation below:

$$\Phi_{\alpha(X)} = \prod_{i=1}^{m} \Phi_{p_i^\alpha(X_i)} \tag{1.10}$$

where, p_i^α represents the multi-index vector. The selection of the univariate polynomial basis function depends on the probability density function. Let us assume if there is a uniform distribution; then the Legendre polynomial would be considered as the basis function. Now the PCE coefficient a_α can be calculated with the regression approach by minimizing the mean square error $\sum_{j=1}^{N}(y_D^j - y(x_D^j))^2 + \gamma a^T a$. For a data space D of N input parameters $X_D = (x_D^1, x_D^2, \ldots, x_D^N)$ and their corresponding output vector $Y_D = (y_D^1, y_D^2, \ldots, y_D^N)$, the expansion coefficients are determined by the following equation:

$$a = (\theta^T \theta + \gamma I)^{-1} \theta^T Y_D \tag{1.11}$$

Where γ denotes the regularization factor, I represents the identity matrix, and θ is the design matrix with components $\Phi_j(x_D^i)(i = 1, ..., N; j = 1, .., NP)$. The total number of sample inputs are $N = \gamma NP$, while $\gamma \geq 1$ is the oversampling parameter which controls the quality and accuracy of the PCE.

1.4.3 Polynomial orthogonal decomposition

Reduced-order modelling (ROM) has gained popularity in the computational community as a means to reduce high computation costs without compromising accuracy, especially where dimensionality is a big challenge. ROM gives a faster surrogate model for computationally expensive simulations. Such speed is especially useful for optimizations of real-time tracking tasks that require significantly large model iterations or rapid online predictions in industrial applications and in fundamental science.

One of the more popular ROM methods to convert a high dimensional problem to a low-dimensional problem is proper orthogonal decomposition (POD). POD was initially presented by (Pearson, 1901) in 1901, and has since been developed and improved to provide an effective and efficient technique for ROM analysis for several applications (Xiao, Fang, Pain & Navon, 2017). Recent developments have provided many non-intrusive methods to calculate the coefficients of linear POD approximations with the help of data-driven approaches without compromising the governing equations (Chatterjee, 2000). This method consists of a stochastic framework, such as POD with polynomial chaos expansion (POD-PCA) or POD coupled with an artificial neural network (POD-ANN), which constructs a regression framework with the reduced-order modelling between the input parameters and the coefficients of POD basis (El Moçayd, Mohamed, Ouazar & Seaid, 2020) (Abdedou & Soulaïmani, 2021) (Jacquier, Abdedou, Delmas & Soulaïmani, 2021) (Sun & Choi, 2021).

POD initially originated from the turbulence flow field with the concept of forming deterministic functions by decomposing the random vector fields of turbulence fluid motion and representing fluctuating kinetic energy in the flow (Lumley, 1967) (Weiss, 2019). The expectation was that this finite number of deterministic functions, also known as POD modes, would be able to describe the flow structure. This approach has been widely adopted in other fields. The POD compresses two essential properties: optimality and orthogonality. Optimality ensures that the POD provides the most efficient decomposition, which means the leading modes possess the highest possible energy compared to all the linear decompositions during projection over the subspace. Orthogonality indicates that the time series of the coefficients are linearly uncorrelated, an important property for making reduced-order models.

Zhao *et al.* (2021) used POD for the thermal study of the electron beam melting system. Their investigation used the ABAQUS model and POD to study the temperature distribution of a moving energy source in the EBM process. Likewise, (Gaonkar & Kulkarni, 2015) (Fic, Białecki & Kassab, 2005) (Białecki, Kassab & Fic, 2005) developed POD-based ROM methods to solve the linear and non-linear transit heat transfer problem and presented a good correlation of the standard FEM code and POD-FEM results. The central core of POD application is building a high-fidelity snapshot matrix to obtain a small set of eigenmodes and the coefficients of the linear basis constructed with these modes. (Liu & Liu, 2023) performed a ROM with POD and generated a map for input parameters and the POD bases with the help of the regression tree method. The constructed map was later used to project the outcomes for a new set of input variables. In two different studies (Abdedou & Soulaïmani, 2021) (Jacquier *et al.*, 2021) POD modes are combined with ML models, including artificial neural networks (ANNs). The POD and ML algorithms have proven effective and productive in analyzing large data sets and processes. Our study uses a POD-ANN method that constructs a regression surrogate model for the ROM to learn and predict the strains in an SLM-built part.

Let us suppose $Y = [y_1, y_2, ...y_n]$ is a real valued $m \times n$ matrix whose rank is $d \leq min(m, n)$ with columns $y_j \in R^m$, $1 \leq j \leq n$. POD is combined with a singular value decomposition (SVD) to obtain the reduced order model and a low rank approximation that is easy to compute (Weiss). The SVD assures that there are real numbers $\sigma_1 \geq \sigma_2 \geq ... \geq \sigma_d > 0$ and orthogonal matrices $\Psi \in R^{m\times m}$, with columns $\{\Psi_i\}_{i=1}^m$, and $\Phi \in R^{n\times n}$, with columns $\{\phi_j\}_{j=1}^n$, such that

$$\Psi^T Y \Phi = \begin{pmatrix} D & 0 \\ 0 & 0 \end{pmatrix} \tag{1.12}$$

Here, $D = diag(\sigma_1, \sigma_2 ... \sigma_d) \in R^{d\times d}$. The zero blocks in equation 1.12 have the appropriate dimensions, and T represents the matrix transpose. In addition, $\{\Psi_i\}_{i=1}^{d}$ and $\{\phi_i\}_{j=1}^{d}$ satisfy the properties

$$Y\phi_i = \sigma_i\psi_i \; and \; Y^T\psi = \sigma_i\phi \tag{1.13}$$

where $i = 1, 2, ...d$, and which these are eigenvector of YY^T and Y^TY , respectively, with the eigenvalues $\lambda_i = \sigma_i^2 > 0, i = 1, 2....d$. Also, $\{\psi_i\}_{i=d+1}^{m}$ and $\{\phi_i\}_{i=d+1}^{m}$ are eigenvectors with the eigenvalue 0 of YY^T and Y^TY (if $d < m$ and $d < n$). From equation 1.12 we can write

$$Y = \Psi \begin{pmatrix} D & 0 \\ 0 & 0 \end{pmatrix} \Phi^T \tag{1.14}$$

For a finite number of initial L modes, the truncation criteria are imposed on the singular values as shown below:

$$\frac{\sum_{l=L+1}^{r} \sigma_l^2}{\sum_{l=1}^{r} \sigma_l^2} \leq \delta \tag{1.15}$$

where δ is a small parameter. So, every mode vector V_j may be calculated from the jth column of ϕ as

$$v_j = \frac{1}{\sigma_i} Y\Phi_j \tag{1.16}$$

Thus, the POD mode matrix can be constructed as below

$$V = [V_1|......|V_j|....|v_L] \in R^{m\times L} \tag{1.17}$$

Once the POD modes are obtained, they are then used to calculate the projection coefficients v for the snapshot matrix as shown:

$$v = V^T Y \tag{1.18}$$

Similarly, the POD bases and the projection coefficients can be used to find the approximation matrix of Y:

$$Y^* = VV^T Y = Vv \tag{1.19}$$

The quality of the compression/expansion process can be captured by the relative projection error shown in the equation:

$$RE_{POD} = \sum_{j=1}^{n} \frac{||y_j - y_j^*||_2}{||Y_j||_2} \tag{1.20}$$

where j represents the jth column of the targeted matrix and $||.||_2$ is the L^2- norm.

1.4.4 Convolution autoencoder

One of the traditional methods for reduced order modeling is the projection-based technique is one of the conventional ways to create a reduced order modeling, that assumes a low rank approximation with a linear combination of basis functions (Quarteroni, Rozza *et al.*, 2014). Such basis functions are created using a fully order model snapshot matrix. For example, Proper orthogonal decomposition Ravindran (2000) is one such methods, which forms a linear reduced-order model by breaking down the snapshot matrix into principal components and employs Galerkin projection (Carlberg, Barone & Antil, 2015). But, for many real-life problems and non-linear phenomena, linear reduced-order models don't produce significantly accurate results (Unger & Gugercin, 2019). Thus it is recommended to use the nonlinear reduced-order modeling techniques like auto-encoders (Hinton & Salakhutdinov, 2006) and kernel PCA to reduce the dimension. However, these projection-based methods are essential in dimensionality reduction, but, they depend on the controlling differential equations and difficult to solve with spatiotemporal data where equations are not known. Machine-learning algorithms require data to mimic a certain task and make them appropriate to strengthen spatiotemporal data and connect with measurement results. These data-driven techniques are instrumental in the offline–online strategy for active control by integrating with measurement data. The data-driven models can create a low-dimension approximation from large data in the offline stage, and it can provide real-time scalable while the data-driven model can be trained to learn a reduced representation from the high-dimensional physical data in the offline stage, the reduced model in the online stage can provide nearly real-time and scalable projections for control and optimization tasks.

An autoencoder is a type of deep neural network that is useful for unsupervised feature extraction. The architecture has the potential for modal decomposition because it provides a framework that includes non-linearity in the mapping by using a nonlinear activation function. However, the modal decomposition of an input field that contains multiscale coherent features is challenging for a neural network autoencoder. This challenge can be overcome by using convolution layers in the autoencoder to process the input information.

Convolutional autoencoders (CAEs) have gained popularity in image recognition as powerful techniques for non-linear reduced-order modelling. The convolution layers provide an alternative approach to the limitations that a classical autoencoder based on deep neural networks (i.e. fully connected layers) faces for high dimensional inputs (Gonzalez & Balajewicz, 2018). (Tan *et al.*, 2019) presented a convolutional neural network (CNN)-based autoencoder (CAE) model to detect anomalies in an AM-built part for reduced order modeling. CNN autoencoders include different operations like convolution, multilayer perceptron, upscaling and pooling (He, Shi, Tan, Song & Zhu, 2021) (Gonzalez & Balajewicz, 2018), thereby helping to reduce the number of training parameters required. In similar studies (Shi, Mamun, Kan, Tian & Liu, 2022) (Siddalingappa & Kanagaraj, 2021) (Tang, Vian, Tang & Yang, 2021), a CAE is combined with Long Short-Term Memory (LSTM) networks to build a framework for surrogate modelling projections, especially for time-dependent predictions in AM-built parts.

A CAE has two parts, an encoder and a decoder. The encoder part reduces the input matrix dimension and maps it to a latent space using a composition of convolutions, pooling, and densely connected layers. The decoder uses convolutions, upscaling, and dense layers to map the latent space to the original dimension of the input matrix.

A convolution layer is a feature map representation in which a selected part of a previous layer is fully connected with each unit of the next layer with the help of an activation function and a kernel. This connection permits the calculation of the most significant features from the input matrix with the help of the kernel. A mathematical representation of a 1D convolution layer is given by (Maulik, Lusch & Balaprakash, 2021):

$$h_i^l = \sigma(H^{l-1} * f_i^l + b_i^l) \tag{1.21}$$

in which the $*$ denotes the 1D convolution operator, $h_i^l \in R^{D_l \times 1}$ represents the i^{th} feature of the l^{th}, σ is the nonlinear activation function, $H^{l-1} = [h_1^{l-1}, h_2^{l-1} \ldots h_{N_{f_{l-1}}}^{l-1}]$ represents the convolution layer $l-1$, b_i^l gives bias value with $i \in N_{f_l}$, f_i^l represents kernel for layer l and $l \in (1, n)$. The depth of the convolution layer is represented by the total number of layers. After each layer, the pooling layers are inserted to decrease the dimension of the features by an amount that is defined by the kernel size of the pooling layer.

As presented in the previous section, the snapshot matrix consists of a set of n high-fidelity solutions obtained from the numerical simulation $Y(\alpha_s) \in R^m, s = 1, \ldots .n$. In this solver, α_s is the s^{th} value of the random variable α in its data sample with size n, which follows a probability density function $\varphi(\alpha)$. All these vectors' solutions are combined and form a global snapshot matrix:

$$Y = [y_1 ... y_s ... y_n] \nu R^{m \times n} \tag{1.22}$$

Where m is the total number of computational nodes in the spatial domain. The global snapshot matrix created above is divided into two sets, one with 80% and the other with 20% of the data for training and validation, respectively.

The CAE framework is divided into three parts: 1) spatial compression, 2) a regression-based multilayer perceptron (MLP), and 3) online surrogate predictions. The spatial compression provides the dimension reduction of the input data matrix from n to L along the spatial dimension where L represents the latent space dimension. The snapshot matrix Y is reshaped using the space encoder $F_{x_{enc}}$ part of the CAE along the spatial dimension, as given:

$$V_{xL} = F_{x_{enc}}(Y) \in R^{m \times L} \tag{1.23}$$

where V_{x_L} represents the snapshot matrix with reduced dimension. The detailed structures for every autoencoder in the test set and the benchmark problem are given in appendices A1 and A3. Once the latent space is constructed, the next level of the CAE framework is applied: the implementation of MLP in the latent space. The MLP maps the latent space V_{x_L} to the input variables α. The MLP model consists of multiple fully connected neuron layers. The detailed structures of the MLP applied for each case are given in appendices A2 and A4. The compression of the spatial dimension and the MLP are classified as an offline phase of the CAE. It must be noted that the framework presented here is built using the open source package TensorFlow with the Adam optimizer and its default parameters. The input snapshot parameters are normalized to accelerate the optimization and the convergence of the training process, and the coefficients of the snapshot matrix are normalized between [-0.5 0.5], as:

$$\frac{Y_{si} - min(Y_s)}{max(Y_s) - min(Y_s)} \tag{1.24}$$

where $s = 1, ...n, i = 1.....m$, u_{si} is the normalized outptu for the s^{th} input parameter and the i^{th} mesh node.

The final step is the online surrogate prediction of a new data set.
A new set of input variables is constructed using the Latin hypercube sampling (LHS) algorithm . For each value of the new data set, a spatial latent vector ($V^*_{x_L}$) is generated using the trained MLP regression model. The predicted latent space is then transformed back to the original dimension using the spatial decoder function ($F_{x_{dec}}$),$Y^* = F_{x_{dec}}(V^*_{x_L})$.

1.5 Sensitivity and uncertainty analysis

Uncertainty sources can be classified into two categories: epistemic and aleatory uncertainty. Aleatory uncertainty in a system occurs due to natural causes such as fluctuation in the laser power, etc. The sources of epistemic uncertainty, meanwhile, are an incomplete understanding or a lack of knowledge, which can be further divided into two types, data uncertainty and model uncertainty. Data uncertainty arises because of improper measurements and an insufficient amount of measured data. Model uncertainty is used to quantify the difference between experimental data and numerical simulation models. For example, model uncertainty may occur due to the assumptions made to simplify the numerical model (Hu & Mahadevan, 2017). To understand the relationship between uncertainties in input and output parameters, we proposed performing a sensitivity analysis (SA). These can be divided into two types, local and global sensitivity analyses. Local sensitivity analysis is derivative-based; this technique analyzes the effect of one parameter on the process by keeping other parameters constant. In global sensitivity analysis, all the input parameters are varied simultaneously, and the sensitivity is calculated over the whole sample space of each input.
There are different approaches to performing sensitivity and uncertainty analysis in SLM. The most popular method is trial and error experimentation. Delgado *et al.* (2012) conducted an experimental investigation to determine the influences of input parameters (laser speed, build direction, and layer thickness) on SLM output. They used a full factorial experimental design technique with three factors, and two levels for each factor. The dimensional accuracy, roughness,

and mechanical properties were considered to measure the effect of input parameters. UA and SA of the AM process using experiments may give good results to some extent, but these analyses have various disadvantages. For example, experiments on a large scale lead to material wastage and a delay in final product delivery, subsequently increasing the product and process cost. Additionally, one component's results may not be applicable to other SLM products, as results may vary with the problems (Hu & Mahadevan, 2017).

Criales, Arısoy & Özel (2016) used finite element modeling to analyze 2D temperature profiles and melt pool geometry. They performed a sensitivity analysis by changing one input parameter at a time while keeping the other parameters constant and found that the powder reflectivity affects the melt pool geometry the most. However, changing parameters one at a time does not always provide good results, as this process fails to consider the interaction of parameters. Bruna-Rosso, Demir, Vedani & Previtali (2018) conducted a global sensitivity analysis for SLM using a 2D numerical simulation model. They used 26 input parameters and calculated their influence on melt pool width, length, and maximum temperature. The effect on the output was calculated by changing the input parameters simultaneously instead of changing one at a time. They used the elementary effect technique and found that 16 of the parameters did not significantly affect the process output. Similarly, Lopez, Witherell & Lane (2016) used a numerical model for single-track simulation to identify uncertainties in the SLM process. Moser, Fish, Beaman & Murthy (2014) performed a sensitivity and uncertainty analysis by developing a numerical model of SLS process using the ANSYS Fluent software. The study considered powder density, average particle diameter, powder conductivity, simulation time and powder specific heat as the input parameters and there effect on the temperature distribution was investigated. The sensitivity analysis finds that specific heat is the most sensitive parameter. The model finds the peak temperature rise for a stationary laser stays within one standard deviation of the mean calculated by the framework.

Recently, surrogate models have gained popularity for UA in the AM process. The most commonly used surrogate models in AM are support vector machines (SVM), neural networks

(NNs), Gaussian process (GA) models, and polynomial chaos expansion Hu & Mahadevan (2017). Cai & Mahadevan (2016) developed a methodology to study the uncertainty in a final product's microstructure via the construction process parameters and environmental changes. They replaced the finite element model with the Gaussian surrogate model and applied it to study the relationship between the cooling rate and the final product's microstructure. A similar methodology was adopted by Sankararaman, Ling & Mahadevan (2011), who used a surrogate model to quantify the uncertainties in fatigue crack growth in AM. Tapia *et al.* (2018) proposed a Gaussian process-based surrogate model to make a response surface between the SLM process output and the input parameters. Their surrogate model was constructed using 96-single-track experimental data to predict the melt pool depth. The model was then used to calculate the melt pool depth at unobserved input process parameters. Kamath (2016) performed uncertainty and sensitivity analysis of the SLM process by combining numerical and surrogate models to reduce the computation time. The research used the Eagar-Tsai model to simulate the melt pool dimensions given the laser speed, power, absorptivity and beam size. A large data set was constructed with a numerical model, and then the regression tree and Gaussian process models were used to construct two separate surrogate models for the process.

1.6 Optimization of SLM process

Optimization is the process of finding the best solution in a pool of possible solution for a given problem. The optimized solution could be minimizing and maximizing the cost and efficiency of a problem respectively or it could any other desired results according to the problem. For example a machine allocation problem, where optimum job is to assign separate machines with different capacity and performance along with independent operating cost, so that the production can be increased with the minimum cost. In present time the optimization techniques have been spread across all the fields such as economics, sciences and engineering etc. Due to such popularity in all the areas, the use of optimization techniques has become more substantial as industries want to focus on minimizing the cost or need to distribute resources judiciously. The optimization problems these days are multiobjective and multidisciplinary type. These problems are too complex to solve, which don't only require gradient-based algorithms but also consider non-traditional methods such as ant colony optimization, particle swarm optimization and genetic algorithms.

Additive manufacturing(AM) has been growing at a rapid rate and over the last decade, more attention has been paid to the development of this process. To find specific design requirements in the AM built part, it is essential to optimize the process parameters. Even though a physical-based models are important to learn about the AM process, their construction is extremely complex. In contrast, the traditional experimental methods to understand the process are very expensive and time-consuming. Singh & Prakash (2009) performed optimization analysis using a two-level factorial design of experiment (DOE) and studied the most essential process variable that affects the most built part density. The research concluded that laser power is the most significant variable among the scan speed, laser power, scan spacing and scan velocity. Based on this analysis, a regression model was developed with the optimized and most significant parameter. The density prediction was found to be in good accordance with the published experimental results.

Highly efficient machine learning models have provided an alternative framework for optimizing the AM process Wang, Tan, Tor & Lim (2020). Rong-Ji *et al.* (2009) used an NN framework to optimize the selective laser sintering process parameters by minimizing the shrinkage. They trained the NN with experimental data and then combined it with the genetic algorithm to find the input parameters' optimal values. The proposed structure can be used to optimize any nonlinear and multitudinous system. Tapia, Elwany & Sang (2016) used this approach to predict the porosity of an SLM-built part using a Gaussian process-based model. Additionally, they provided a Bayesian framework to estimate the statistical model's parameters and then used the Kriging method to predict the given parameter settings' porosity. This study primary disadvantage was that only two parameters were used as input variables, whereas the SLM can be affected by many factors, including the materials and environment.

NNs and GAs are the most widely used methods for the optimization, modeling, and prediction of process parameters. Some of the popular GA methods used in AM are multi-genetic programming (MGGP), the multi-objective particle swarm optimizer (MOPSO), the non-dominated genetic algorithm, etc. (Padhye & Deb, 2011). The study used MOPSO and a non-dominated sorting genetic algorithm (NSGA-II) to minimize the surface roughness and built time in the selective laser sintering (SLS) process.

The surface roughness and the built time are functions of the "build direction," and so minimizing them aids in finding the optimal build orientation. A study by Padhye & Deb (2011) also found that the NSGA-II outperforms the MOPSO in finding optimal results. In a similar study by Singhal, Jain, Pandey & Nagpal (2009), a conventional optimization algorithm based on a trust region method was used to optimize the stereolithography (SL) and the SLS process. The objective of the Singhal *et al.* (2009) study was to increase the quality of the built surface and the support structure by determining the optimum deposition orientation for a building part. Below is a review of some of the data-driven optimization methods that have been applied in the process optimization of SLM studies.

1.6.1 Genetic algorithms

Genetic algorithms(GAs) are search algorithms with the principle of natural selection. The algorithm is inspired by the darwin's theory: of survival of the fittest. At the global level the population is submitted for many transformations and after some generations, where the population is not enduring anymore, then the best population set is considered to be the best solution. GA compies the working principle of the genetic process, in which the parents' characteristics are transferred to their offspring. These genes correspond to a specific characteristics like eys, height etc., and are present in the chromosome. For example, in humans, we have 23 pairs of chromosomes and one chromosome in each pair comes from the maternal side, and the other comes from the paternal side. So after crossover, some characteristics of both parents transfer to the child. Also, sometimes there are naturally some genes randomly mutate, and the offspring can have some characteristics different than the parents. These mutation carries the changes in offspring and improves the chance of survivability.

In gradient-based models, the solution runs from one point to another with the help of gradient and Hessian information. However, in GA, one works with a population of points rather than a single point. A GA mimics the genetic process where the characteristics from parents are transferred to the children. It is divided into four phases: initialization, fitness, selection, and combination. At the start of the GA, a sample set of the starting population or a sample set is created, and then for each input parameter, their fitness value (the value of the objective function) is computed. The lowest values are taken as the parents' for the subsequent iterations, and they will produce new offspring for the next iteration. Similarly to the human genes, in a GA, individuals with the least function value will undergo crossovers and mutations to produce better offspring than the parents. By better, we mean their function value is less than their parents' function value(s). A single-point cross-over of 0.8 was established in our present case, and the mutation probability was taken as 0.1 to obtain the best results.

1.6.2 Particle Swarm Optimization

Similar to GA, particle swarm optimization(PSO) carried out search operations simultaneously at large points in the iteration. The PSO technique is motivated by a group of individual and their wisdom, like flock birds or a group of fish moving together. The technique keeps track of the best position among all individual along with the whole population in terms of the objective function. The best values of the objective function for the group and the individual is represented by '$gbest'$ and '$pbest'$ respectively. (Arora, 2015). Each individual in the group moves with a certain velocity which is dependent on the '$pbest'$, '$gbest'$, and their initial velocity. The new position for each individual is determined based on their initial positions and velocity. After this value on new objective function is calculated based on the new positions and the PSO steps are repeated. Each step for the PSO algorithm is given below.

If we assume the ‘nth’ individual in a set, then its initial position is calculated by:

$$x_{i,n} = x_{i,min} + (x_{i,max} - x_{i,min})u_i \tag{1.25}$$

The $x_{i,min}$ and $x_{i,min}$ are the bounds for x_i, and u_i variables, represent a random number between 0 and 1. Computing the fitness value for nth individual:

$$A_{i,n} = f(x_{i,n}) \tag{1.26}$$

In the beginning, the best fitness value $pbest_{i,n}$ for each individual is $A_{i,n}$ and the global best value can be calculated as:

$$gbest_i = min(pbest_{i,n}) \tag{1.27}$$

The new velocity for the individual can then be calculated as:

$$v_{i+1,n} = \varphi_i v_{i,n} + \psi_1(pbest_{x,i,n} - x_{i,n})u_i + \psi_2(gbest_{x,i} - x_{i,n})u_i \tag{1.28}$$

where φ_1, ψ_1 and ψ_2 are the tuning factors, which are 0.8, 2, and 2, respectively, in our study. Now, the new position can be calculated as:

$$x_{i+1,n} = x_{i,min} + (x_{i,max} - x_{i,min})u_i \tag{1.29}$$

Based on the new position, we can evaluate the new fitness value, which is:

$$A_{i+1,n} = f(x_{i+1}, n) \tag{1.30}$$

If the new fitness value is less than that of $pbest_{i,n}$, then it is replaced with the $A_{i+1,n}$. The global fitness value is computed as:

$$gbest_{i+1} = min(pbest_{i+1,n}) \tag{1.31}$$

1.6.3 Differential Evolution(DE)

Differential evolution (DE) is another optimization algorithm that, similar to GAs, is based on an evolutionary process. DE has gained in popularity in recent years for its success in optimization problems in different fields of science and engineering. The algorithm was first introduced by (Storn & Price, 1995) in 1995 to optimize the non-differentiable and non-linear continuous function. DE algorithms are based on stochastic population-driven evolution methods similar to the other evolution methods. This approach uses a population set and searches the whole design space to find the optimal solution using crossover, mutation, and selection operators. One of the differences between DE and the other evolution methods is the mutation strategy used by DE, which applies to each point and explores the whole design space based on other individuals' solutions. (Georgioudakis & Plevris, 2020) presented several DE algorithms based on different crossover and mutation strategies. There are three controlling factors in a DE algorithm: the crossover rate, the population size, and scaling factors, which all must be controlled to get the best performance (Storn & Price, 1997). Figure 1.3 outlines the functioning of a DE algorithm. From mutation to selection, all steps are repeated until the termination criteria are reached. Our study considers the crossover and the scaling factor to be 0.8 and 0.6, respectively.

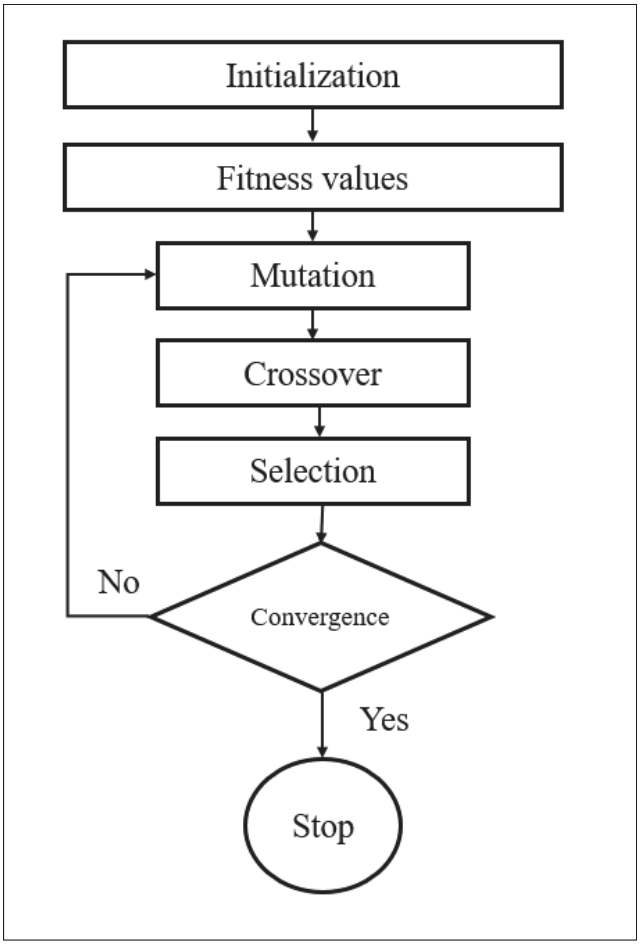

Figure 1.3 Differential Evolution

Research Gap

After completing a detailed literature review, it was found that the final built part of AM process depends on many parameters such as layer thickness, scanning length, hatch spacing etc. these parameters directly or indirectly affect the end product, for example, thinner layer thickness leads to higher stress and deformation whereas higher scan length is responsible for high-temperature gradient and stress in the built process. To find the relation between input and output parameters, the researchers have conducted sensitivity and uncertainty analyses for different case studies. Most of these works are either focused on melt pool studies or single-layer powder melting. There is a significant gap in the research areas, where sensitivity and uncertainty analysis is performed with a whole geometry constructed using the SLM process.

A 3D numerical analysis of AM process has the potential to provide more realistic results for the built part than 1D or 2D analysis. The traditional ways to understand the physic behind the SLM process are experimental and numerical studies. However, performing sensitivity and uncertainty analysis with these methods could be time-consuming and computationally expensive. So, based on the literature review, it is recommended to use a combination of machine learning (ML) algorithms with numerical modeling and then verify those results with experimental results. The ML methods have the capability to reduce the computation cost and can provide good predictions. Also, significantly less attention has been given to the applications of ML methods in AM analysis. If a framework can be provided to the AM community, it can not only speed up the SLM analysis but can also provide better predictions for given input parameters, eliminating the use of traditional methods.

Also, ML models have been widely used for optimization in different research areas, and some of the applications have been implemented in SLM too. However, The lack of numeral modeling for whole geometry and the availability of experimental data to verify such studies have limited the use of ML for whole geometry. So, another essential framework is presented in this research work which again uses ML methods to find the optimal parameters for the optimal SLM outputs. subsequently, a new approach using reduced-order surrogate models is suggested for the analysis of a large number of high-fidelity snapshot matrices. this approach would help handle the big spatial and temporal data matrices during the building process.

CHAPTER 2

COMPUTATIONAL MODELING OF SLM ADDITIVE MANUFACTURING OF METALS

Shubham Chaudhry[1] , James William Tcheumanak Chuitcheu[1] , Azzeddine Soulaimani[1] , Rajeev Das[1]

[1] Département de génie mécanique, École de Technologie Supérieure,
1100 Notre-Dame Ouest, Montréal, Québec, Canada H3C 1K3

Paper published in *International Journal of Manufacturing Research*, November 2022

Abstract

Additive manufacturing (AM) is a technology that can create 3D structures by depositing or melting material in a layer-by-layer manner. This paper focuses on the metal-based powder bed fusion AM approach, specifically the selective laser melting (SLM) technique. The repetitive hot and cold cycles associated with AM cause localized compression and tension giving rise to significant residual stresses, which can lead to shape loss, structural failure, etc. Numerous parameters determine the thermal gradient; these include the thermal characteristics of the powder, the bed temperature, and the part size. This investigation describes the associated problem formulation and numerical resolution in the SLM simulation. An ANSYS-Additive model is developed to determine the parameter dependence on the process. An efficient parameter calibration algorithm is proposed to generate an accurate numerical model. Three numerical studies are conducted using a vertical prism, a horizontal prism, and an L-shaped structure also compared with the experimental data.

keywords

Selective laser melting, Simulation, Additive manufacturing, ANSYS-Additive.

2.1 Introduction

Additive manufacturing (AM) is the process of constructing 3D structures by fusing layers of material powder together. There has been considerable interest in AM in industrial manufacturing, as AM allows the fabrication of more complex shapes and lighter products without any significant material wastage. This ability is beyond the scope of traditional dies, molds, milling and machining. Due to these advantages, AM has been applied in the aerospace and automotive industries, and in the healthcare sector (Horn & Harrysson, 2012). The AM process can be categorized as material jetting, material droplet printing, material extrusion, sheet lamination, powder bed fusion and direct energy deposition. Among these techniques, powder bed fusion is the most widely used method.

In the powder bed fusion (PBF) process, material powder (for instance stainless steel 316L) is selectively fused together layer-by-layer into a 3D structure. The powder bed fusion can be broadly classified as: i) direct metal laser sintering (DMLS); ii) selective electron beam melting (SEBM); iii) selective heat sintering (SHS); iv) selective laser melting (SLM); and v) selective laser sintering (SLS). The heat source in the fusion process can be either a high intensity laser or an electron beam. Selective laser melting (SLM) uses a laser beam as the heat source and selective electron beam melting (SEBM) utilizes an electron beam as the heat source. SLM is slower than SEBM, but it provides a better surface finish than SEBM. In addition, SEBM can be used with fewer types of metal powders compared to SLM. DMLS is similar to SLS, but uses metals instead of plastics. This work considers the SLM process.

One of the challenges associated with SLM is determining the best process parameters to ensure the quality of the built part. The final product may have defects such as the balling effect, surface irregularities, porosity, residual stress and cracks, etc.(Yang, Hwang & Lee, 2002) (Ippolito, Iuliano & Gatto, 1995) (Körner *et al.*, 2011). An understanding of the SLM process can provide valuable insights into the performance margins, the uncertainties in those margins, and their sensitivities to process parameters. To study the sensitivity of process parameters we can use the SLM process with different parameters and then analyze the properties of the final product. Performing an assessment involves repeated experiments; a time-consuming exercise that leads to material wastage, making the process expensive. Numerical modeling and simulation of the SLM process can provide an efficient mechanism with which to develop this understanding. SLM modeling involves numerous complexities and expert knowledge in heat transfer, solid mechanics and phase change.

The effects of process parameters on the SLM product is difficult to determine because of the high dimensionality of parameters' spaces and their interaction(s) with one another. Broadly, the properties of the material, the process, and the environment define a large number of parameters (around 19 parameters) that affect the final product (Körner *et al.*, 2011). In order to meet specific design requirements, these material parameters and the shape of the component may need to be optimized. These challenges can be addressed by utilizing machine-learning methods. The modeling approach involves choosing an experimental design (such as a Taguchi design (Ballantyne, Van Oorschot & Mitchell, 2008)) which takes machine and material parameters as inputs and generates output data in the form of displacements and stress in the SLM product. This technique is used to screen all the parameters simultaneously, thereby helping to identify those that are more significant. Once the input and output data have been generated, a specific model (such as a regression model) is applied to fit the dataset. This numerical model can then be considered in the optimization process instead of the actual SLM model.

In this work, an ANSYS-Additive numerical model was developed to calculate the stress and displacement fields during the SLM process. The ANSYS-Additive software uses a calibration technique for the parameters. In this paper, we have developed a new calibration algorithm which is more precise and faster than the one provided by ANSYS-Additive. Section 2.2 provides the thermo-mechanical mathematical governing equations in an SLM process. The proposed calibration algorithm is then detailed in section 2.3. In next section, three numerical benchmark tests are conducted using a vertical prism, a horizontal prism and an L-shaped structure and the numerical results are compared with experimental data. Finally, some concluding remarks are drawn in section 2.5.

2.2 Mathematical Modelling

The mathematical modeling of the SLM process includes a balanced study of the thermal and mechanical analyses of the process. In thermal analysis, a better understanding of the interaction between the energy source and the powder bed provides improved results about the temperature distribution in the process. When the heat energy from the laser interacts with the powder, most of it will be reflected due to the lustrous nature of the material. The rest of the energy travels through and escapes the system to the surroundings by conduction, radiation and convection. The absorptivity of the energy is controlled by the powder's and the material's morphology. A complete mechanism of the heat transfer in the SLM process is shown in Fig 2.1. This figure shows the melting of a Ti-alloy powder with an Nd:YAG pulse laser source in an SLM process. The heat equation and the boundary conditions with the convection, radiation and conduction are described below.

According to the first law of thermodynamics and Fourier's law, the energy balance equation is given by:

$$\frac{\partial}{\partial x}\left(k\frac{\partial T}{\partial x}\right)+\frac{\partial}{\partial y}\left(k\frac{\partial T}{\partial y}\right)+\frac{\partial}{\partial z}\left(k\frac{\partial T}{\partial z}\right)+\dot{Q}=\rho c_p\frac{\partial T}{\partial t} \tag{2.1}$$

where k is the thermal conductivity, T the object temperature, ρ the material density, t the time, $\dot{Q}$ the internal heat intensity and c_p the specific heat capacity. The primary unknown here is the temperature T. In this equation k is the thermal conductivity that depends on the temperature. However, the effective thermal conductivity of the powder can be a function of other factors like particle shape and size, the thermal conductivity of a gaseous medium or the

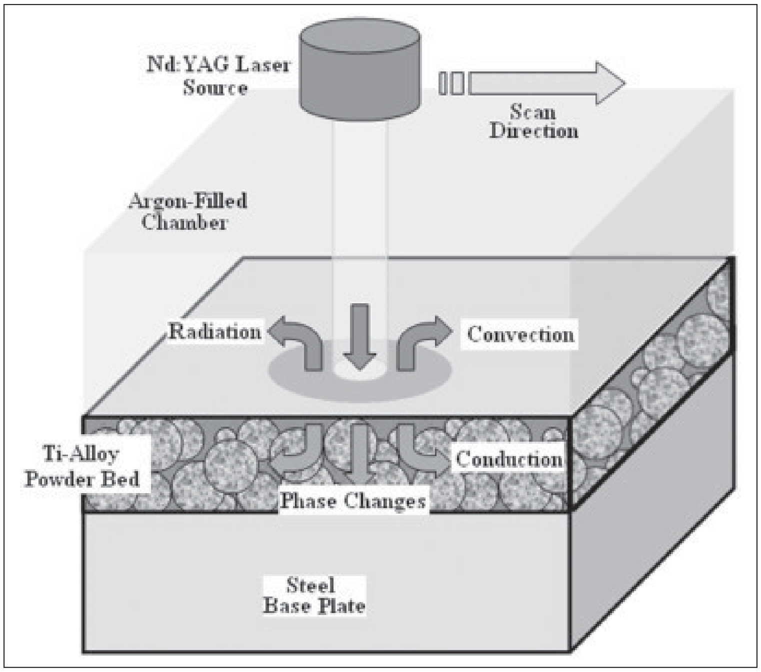

Figure 2.1 Heat transfer during the SLM process taken from Roberts *et al.*(2009, p. 917)

thermal conductivity of a solid. An effective thermal conductivity model of a packed powder bed is derived as a function of local relative density in (Yagi & Kunii, 1957):

$$k_{eff} = \frac{\rho_r k_s(T)}{1 + \varphi k_s(T)/k_g} \tag{2.2}$$

where φ is the empirical coefficient, which is equal to $0.02 * 10^{2(0.7-\rho_r)}$, ρ_r is the powder's relative density, $k_s(T)$ the temperature-dependent solid thermal conductivity, and k_g the thermal conductivity of the chamber gas. Another model for effective thermal conductivity is presented in (Childs *et al.*, 2005), as a function of the porosity β:

$$k_{eff} = k_s(T)(1 - 0.2\beta - 1.73\beta^2) \tag{2.3}$$

where the temperature-dependent conductivity of solid material $k_s(T)$ is (Sun, Nelson, Beaman & Barlow, 1991):

$$k_e(T) = 0.02504 + 0.0005T \tag{2.4}$$

The heat transfer during the SLM process requires two boundary conditions and one initial condition, which are sufficient to model the thermal behavior of the process. The corresponding boundary and initial conditions of the model are Initial condition:

$$T(x, y, z, 0) = T_{base} \tag{2.5}$$

Boundary conditions:

1. Surface convection and radiation:

$$-k\frac{\partial T}{\partial z} = \phi\sigma(T^4 - T_e^4) + h(T - T_e) \tag{2.6}$$

2. No heat loss at the bottom:

$$-k\frac{\partial T}{\partial z}\bigg|_{z=0} = 0 \tag{2.7}$$

where ϕ is the thermal radiation coefficient, σ the Stefan-Boltzmann constant, h the convection coefficient, T_e the room temperature and T_{base} the temperature of the base plate.

Another important aspect in the thermal equation is the modeling of the laser beam as a heat source. The heat source in an SLM process can be modeled as a volumetric heat source or as a heat flux load. In the case of a heat flux load the Gaussian distribution heat source model is generally used. An example of the Gaussian heat source distribution is shown in Fig 2.2. In (Luo & Zhao, 2018) the heat source is modeled as a temperature load to the elements. That work shows the laser heating represented by the internal heat generation term of the thermal equation. The material properties such as surface tension, density(ρ), heat conduction, heat capacity (c_p)

and thermal diffusivity (k) are temperature-dependent; all of these properties affect the quality of the component. Because they exert such a major influence, it is very important to calculate the temperature and its gradient precisely. The Gaussian heat source can be modeled as:

$$q(r) = \frac{2AP}{\pi r_0^2} e^{-\frac{2r^2}{r_0^2}} \tag{2.8}$$

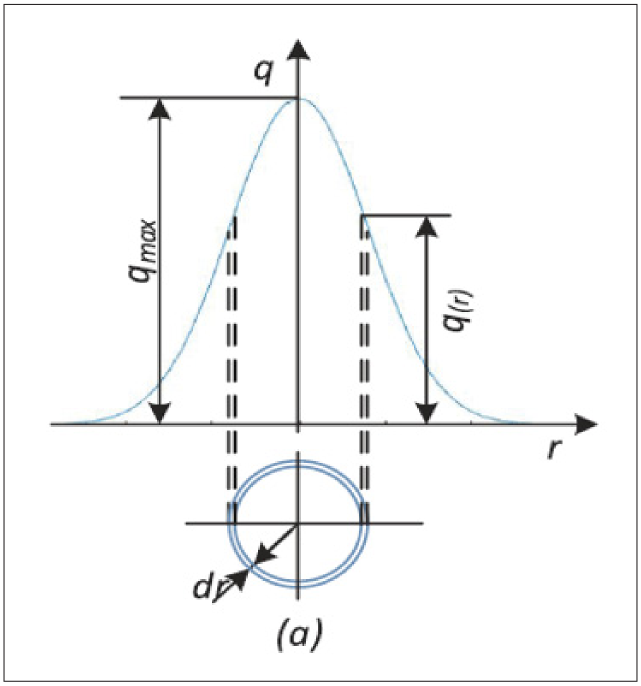

Figure 2.2 Distribution of the Gaussian heat source taken from Luo & Zhao (2018, p. 323)

where A is the powder material absorptivity, P is the power of the laser, r_0 represents the radius of the laser beam, and r denotes the radius from the center of the laser to the exposure. The important factors are the laser power P and the radius of the laser beam r_0 that define the Gaussian model. Once the temperature field is calculated, the stress and the deformation in the geometry are calculated using a mechanical analysis model. A thermal-mechanical model can be coupled or uncoupled. In coupled analysis, the thermal and the mechanical analyses are executed simultaneously at each time step, whereas in an uncoupled model the thermal and mechanical analyses are not interconnected and so both are performed successively. If the material behaviour is considered to be elastoplastic then the governing equations for the stress and strain can be written as (Luo & Zhao, 2018):

$$\sigma = D\varepsilon^{e} \tag{2.9}$$

where ε^{e},σ are the second-order elastic strain tensor and the material stress of the system, respectively, and D represents the material stiffness tensor of order four. The total strain tensor in the material is the combination of the elastic strain ε^{e}, the plastic strain ε^{p} and the thermal strain ε^{th}:

$$\varepsilon = \varepsilon^{e} + \varepsilon^{p} + \varepsilon^{th} \tag{2.10}$$

In the case of homogeneous and isotropic material:

$$\varepsilon = \frac{1+\nu}{E}\sigma - \frac{\nu}{E}tr(\sigma) \tag{2.11}$$

$$\varepsilon^{p} = g(\sigma_{Y}) \tag{2.12}$$

$$\varepsilon^{th} = \varphi(T - T_{0}) \tag{2.13}$$

where ν, E and φ is the Poisson's ratio, Young's modulus, and the thermal expansion coefficient, respectively, $T4$ and T_{0} are the nodal and initial temperature, respectively, and $g(\sigma_{Y})$ represents the function of yield strength σ_{Y}. In this work, we have used the ANSYS-Additive software to solve the governing equations.

The ANSYS-additive solver is a macroscopic additive manufacturing solver and which considers the melt pool dynamics. The ANSYS-additive has three modules, which include 1) Assumed strain-Uniform strain 2) Scan pattern strain-anisotropic and 3) thermal strain -Anisotropic. The assumed strain is the fastest Ansys additive simulation available. It assumes an isotropic average strain at each point in the geometry. The in the geometry is calculated by dividing the yield strength (σ_{yield}) with the elastic modulus(E) and multiplying the ratio with Strain scale factor(SSF).

$$\varepsilon = SSF \times \frac{\sigma_{yield}}{E} \tag{2.14}$$

In the Scan pattern strain module, the average stain magnitude is the same as the assumed uniform strain, but the strain magnitude is divided into different anisotropic components, which is calculating using the local orientation of the scan vectors. The magnitude of each strain component is calculated as follow:

$$\varepsilon_{xx} = SSF \times ASC_x \frac{\sigma_{yield}}{E} \tag{2.15}$$

$$\varepsilon_{yy} = SSF \times ASC_y \frac{\sigma_{yield}}{E} \tag{2.16}$$

$$\varepsilon_{zz} = SSF \times ASC_z \frac{\sigma_{yield}}{E} \tag{2.17}$$

Here ASC is the anisotropic strain coefficients and $\varepsilon_{xx}, \varepsilon_{yy}, and \varepsilon_{zz}$ represent the longitudinal strains in x, y, z directions, respectively. Both the modules are fast because it reduces the complexity of thermo-mechanical simulation to solo mechanical only. To calculate the strain results in the building part, we have to calibrate the SSF and anisotropic coefficients for a given machine and material. Once the coefficients are calculated, then we can predict the strain results for any parameters in a given machine.

The third and final module is the thermal strain, which we have used in this paper. It has higher accuracy than the other two modules as it predicts the accumulation of strains in the building part due to thermal cycling. During the layer-by-layer process, the thermal strain module uses the inherent strain and modifies the strain values using a thermal ratcheting algorithm. The thermal ratcheting algorithm of the solver assigns base strain values to each location as it solidifies. During the process, when each position in the building part is heated above the temperature threshold(approximately 0.4 of the melting temperature), an increase in the strain will occur. Every time a location is heated above the threshold, it leads to the accumulation of the strain at that location, and if the location is re-melted, then the strain value of that location would be set as a base value. After the calculation of strain value at every position, that strain is passed to the mechanic's solver. The strain values will be applied as an anisotropic strain, which is based on the local orientation and the local strain magnitude. In the case of isotropic material, the values of the $ASCs$ are equal to one. In contrast, for an anisotropic case, we have to calibrate the exact values using a calibration algorithm. The values of SSF and ASC are different for different machines and materials. In this work, the experimental tests of (Wu *et al.*, 2014) are used to validate the proposed calibration algorithm.

2.3 Calibration procedures

For complex modeling problems such as the SLM process, any numerical model requires a calibration method to adjust the process and material properties. In ANSYS-Additive, the values of the Strain Scale Factor (SSF) and the Anisotropic Coefficients (ASC) are important to improve the accuracy of the simulation. The SSF is a direct multiplier of the predicted strain values in the simulation, while the ASC_x, ASC_y, and ASC_z correct the predicted strain values along the longitudinal, the transverse and the depth direction. The SSF and the $ASCs$ must be adjusted to calibrate the numerical model when some measurements are available. The calibration process is iterated with updated values of the SSF and ASC until the desired results of the comparison between simulated and experimental results are found. The calibration algorithms 2.1 provided by ANSYS-Additive, (Ansys) and the one proposed here are described below. Both calibration techniques have the following assumptions:

- The anisotropic coefficient in the z direction is always equal to 1, and the sum of the anisotropic coefficients in the x and y directions (ASC_{x_1}, ASC_{y_1}) is equal to 2; and
- The ratio of anisotropic coefficients in the x and y directions are a linear function of the difference of distortion in the corresponding directions.

Algorithm 2.1 Calibration process proposed in ANSYS-Additive

```
Get the maximum measured experimental displacements $u_x^m u_y^m$ and $u_z^m$
Set $SSF_1 = 1, ASC_{x_1} = 1.5, ASC_{y_1} = 0.5, ASC_{z_1} = 1$
Get values of maximum simulation displacements $u_{x_1}^s, u_{y_1}^s$ and $u_{z_1}^s$
for For i=2 number of iterations, calculate new values of $SSF, ASC_x, ASC_y, ASC_z$ using do
    $SSF_i = \frac{1}{2} \times \left( \frac{u_x^m}{u_{x_{i-1}}^s} + \frac{u_y^m}{u_{y_{i-1}}^s} \right)$
    $ASC_{x_i} = \frac{1}{SSF_i} \times \left( \frac{u_x^m}{u_{x_{i-1}}^s} \right)$
    $ASC_{y_i} = \frac{1}{SSF_i} \times \left( \frac{u_y^m}{u_{y_{i-1}}^s} \right)$
    $ASC_{z_i} = 1$
    Convergence criteria: if the desired error between experimental and numerical
      displacements is not satisfied: Run new simulation and get $u_{x_1}^s, u_{y_1}^s$ and $u_{z_1}^s$
end for
```

In our proposed calibration method, the algorithm described below is adapted from the initial calibration procedure where a relaxation factor α is introduced to improve the convergence of the iterations. The can be between 0 and 1 which varies from machine to machine and material to material.

2.4 Benchmark tests

The validation tests are based on relevant experimental results from the work of (Wu *et al.*, 2014), which have become benchmarks for validating numerical results. The objectives of that paper

Algorithm 2.2 calibration procedure with relaxation

```
Set $SSF_1 = 1, ASC_{x_1} = 1.5, ASC_{y_1} = 0.5, ASC_{z_1} = 1$
Get the maximum measured experimental displacements $u^m_x u^m_y$ and $u^m_z$
Run first thermo-mechanical simulation and get displacements $u^s_{x_1}, u^s_{y_1}$ and $u^s_{z_1}$ and
  compute
$SSF_2 = \frac{1}{2} \times \left( \frac{u^m_x}{u^s_{x_{i-1}}} + \frac{u^m_y}{u^s_{y_{i-1}}} \right)$
$ASC_{x_2} = \frac{1}{SSF_i} \times \left( \frac{u^m_x}{u^s_{x_{i-1}}} \right)$
$ASC_{y_2} = \frac{1}{SSF_i} \times \left( \frac{u^m_y}{u^s_{y_{i-1}}} \right)$
$ASC_{z_2} = 1$
for Run second simulation and get displacements $u^s_{x_1}, u^s_{y_1}$ and $u^s_{z_1}$ Set a value for the
  relaxation factor $\alpha$ (for example $\frac{3}{4}$ which can be different for different machine and
  material) and compute do
    $u^s_{x_i} = \alpha(u^s_{x_1} +u^s_{x_{i-1}} + (1 - \alpha)u^s_{x_2}$
    $u^s_{y_i} = \alpha(u^s_{y_1} +u^s_{y_{i-1}} + (1 - \alpha)u^s_{y_2}$
    $SSF_3 = \frac{1}{2} \times \left( \frac{u^m_x}{u^s_{x_{i-1}}} + \frac{u^m_y}{u^s_{y_{i-1}}} \right)$
    $ASC_{x_3} = \frac{1}{SSF_i} \times \left( \frac{u^m_x}{u^s_{x_{i-1}}} \right)$
    $ASC_{y_3} = \frac{1}{SSF_i} \times \left( \frac{u^m_y}{u^s_{y_{i-1}}} \right)$
    $ASC_{z_3} = 1$
end for
for for $i = 3$ maximum number of iterations do
    $u^s_{x_i} = \alpha(u^s_{x_1} + u^s_{x_{i-1}} + (1 - \alpha)u^s_{x_2}$
    $u^s_{y_i} = \alpha(u^s_{y_1} + u^s_{y_{i-1}} + (1 - \alpha)u^s_{y_2}$
    $SSF_3 = \frac{1}{2} \times \left( \frac{u^m_x}{u^s_{x_{i-1}}} + \frac{u^m_y}{u^s_{y_{i-1}}} \right)$
    $ASC_{x_3} = \frac{1}{SSF_i} \times \left( \frac{u^m_x}{u^s_{x_{i-1}}} \right)$
    $ASC_{y_3} = \frac{1}{SSF_i} \times \left( \frac{u^m_y}{u^s_{y_{i-1}}} \right)$
    $ASC_{z_3} = 1$
end for
Convergence criteria: if the desired error between experimental and numerical
  displacements is not satisfied:
Run new simulation and get $u^s_{x_1}, u^s_{y_1}$ and $u^s_{z_1}$
```

were two-fold: to measure the surface deformations associated with the sectioning of a part by image correlation (DIC), and to measure the internal stresses of a part by neutron-diffraction.

2.4.1 Description of the geometries and scanning strategy

Simple stainless steel 316L specimens were tested as shown in Figure 2.3. The prism specimen was constructed in two configurations, horizontal and vertical. The information required to understand the construction and testing performed on these samples is very well detailed in the original reference (Wu *et al.*, 2014).

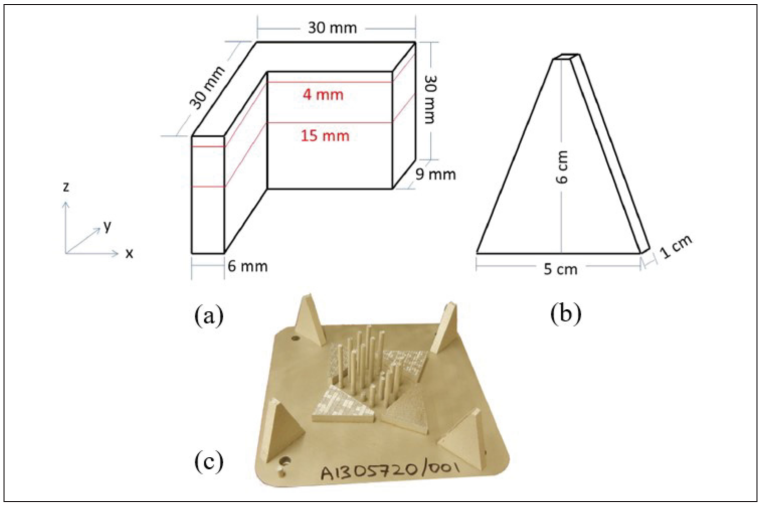

Figure 2.3 (a) L cross section sample dimensions, (b) Prism sample dimensions, and (c) Built plate containing vertical and horizontal prisms taken from Wu *et al.* (2014, p. 6262)

There are several laser-scanning strategies for the additive manufacturing of parts. Some machine builders use island scanning, as shown in Figure 2.4(a), where the islands are placed at random until the complete transformation of the cross section has been achieved. Random-island scan strategy cannot be reproduced in ANSYS-Additive software (used in our study), and so we have approximated the laser's path by equating it into a monolithic serpentine path (shown in Figure 2.4(b)), similar to the approximation adopted by (Hodge *et al.*, 2016). The units used for the deformations and the stresses are in millimeters and mega Pascal (MPa), respectively.

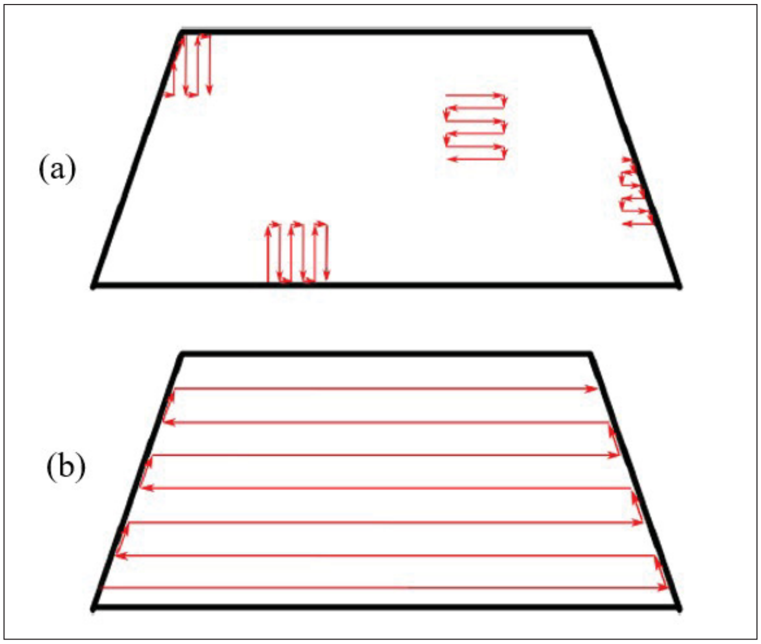

Figure 2.4 (a) Island scanning strategy used by many manufacturers, and (b) Monolithic serpentine approximation used in the present study taken from Hodge *et al.* (2016, p. 160)

2.4.2 Numerical experiments

Our simulations deal with three geometries: a horizontal prism, a vertical prism and an L-shaped part. To start a simulation in ANSYS-Additive, we need different types of data, including the properties of the material used, the configuration parameters of the additive manufacturing machine, the STL file of the part to be manufactured and the initial information on the structure supports. All tests were performed on a PC running under Windows 7 using a 4-core CPU (Intel® Core ™ I7-3770 CPU @ 3.40 GHz with a RAM of 8.00 GB). The duration of an iteration (simulation) in the calibration process was estimated at about 2 hours (for the L-shape specimen), 5 hours (for the vertical prism specimen) and 6 ½ hours (for the horizontal prism specimen) using 4 cores. In addition, it took an average of 7 to 15 simulations (using the new calibration formulation developed during this study) to obtain a convergence in the displacement results. To reduce the computational time, the software can be run on a 12-core computer.

The material properties and the configuration parameters of the machine are shown in Tab 2.1 and 2.2, respectively.

Table 2.1 Material properties

Quantities	**Values**
Powder absorptivity	0.66
Solid absorptivity	0.4
Thermal expansion coefficient	$19.23 \times 10^{-6}/K$
Elastic modulus (GPa)	$187Gpa$
Solid absorptivity	$0.265<\theta<0.275$
Material yield strength (MPa)	$422MPa$
Support yield strength ratio	0.66
Hardening factor	0.0198
Strain scaling factor	To calibrate
Anisotropic strain coefficients (x-longitudinal)	To calibrate
Anisotropic strain coefficients (y-transversal)	To calibrate
Anisotropic strain coefficients (z-printing)	1

Table 2.2 Machine configuration settings

Parameters	**Values**
Powder Layer thickness	$30\mu m$
Layer thickness	$0\,^{\circ}$
Layer rotation angle	$0\,^{\circ}$
Hatch spacing	$100\mu m$
Slicing stripe width	$5\mu m$
Laser wattage	$400W$
Hardening factor	0.0198
Scan speed	$1800mm/s$
Baseplate temperature	$303K$

For the horizontal and vertical prisms, quantified experimental displacement results were obtained from (Wu *et al.*, 2014). The meshes of all of the geometric models presented in this study were chosen so that there are at least four voxels (cubic mesh elements) in the thinnest thickness of the geometry. For these two cases, we performed a mesh convergence study using three mesh sizes (0.35 mm, 0.30 mm and 0.22 mm); the comparisons are detailed first for the medium mesh (0.30 mm.).

2.4.2.1 Horizontal prism

The first comparison is focused on horizontal prism. Tab 2.3 summarizes the comparison for the medium mesh.

Table 2.3 Comparisons of numerical and experimental results for a horizontal prism with a medium mesh

Mesh size 0.30mm	**UXmin**	**UXmax**	**UYmin**	**UYmax**	**UZmin**	**UZmax**
Wu *et al.* (2014).	-0.045	0.045	-0.07	0.04	-0.05	0.08
Present results	-0.035	0.035	-0.094	0.061	-0.048	0.2
Hodge *et al.* (2016)	-	-	-	-	-0.04562	0.09029

The following figures present the results concerning the compression displacements. We could not obtain convergence in the results when we used the calibration procedure of the anisotropic coefficients and the scale factor proposed in ANSYS' documentation, as shown in Fig 2.5:

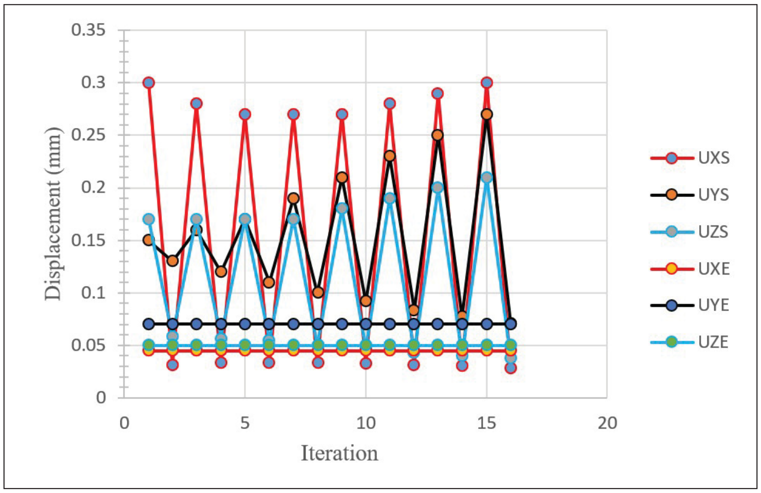

Figure 2.5 Evolution of the maximum displacements using the calibration proposed by ANSYS: horizontal prism

Here UXS, and UXE represent the maximum displacements in x-direction obtained using simulation and experiment. Similar notation is used for the displacements in y and z directions.

However, the new calibration procedure described in section 4 makes it possible to have a simultaneous convergence of the displacements along the three axes (x, y and z), as shown in Fig 2.6.

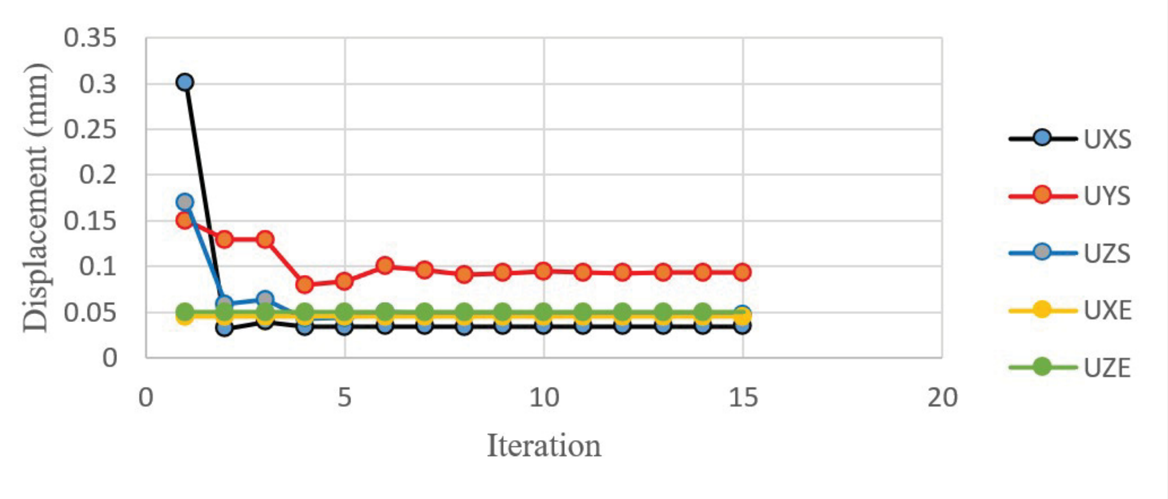

Figure 2.6 Evolution of the maximum displacements using the proposed calibration procedure: horizontal prism

Fig 2.7 shows the displacements in the x, y and z directions associated with the removal of the horizontal prism from its base. The final anisotropic coefficients used to obtain our results are 0.676 along the x axis, 1.324 along the y axis and 1 along the z axis. The strain scaling factor (SSF) used for our results was 0.256.

By comparing the displacements along each axis (x, y or z), we observe that the distribution of the simulation results corresponds well to those of the experimental results, even though the amplitudes of displacement are not always as close as we would wish. However, since the calibration procedure used here is based exclusively on the experimental data in compression, we can observe a consistency between the compression displacement amplitudes of the experimental and simulation results, as shown in Fig 2.8,2.9, and 2.10.

(Hodge *et al.*, 2016) used the experimental results of (Wu *et al.*, 2014) to validate the ability of their code (Diablo) to predict deformations and stresses on the benchmark tests. We compare our results with those of (Hodge *et al.*, 2016) in the following paragraphs.

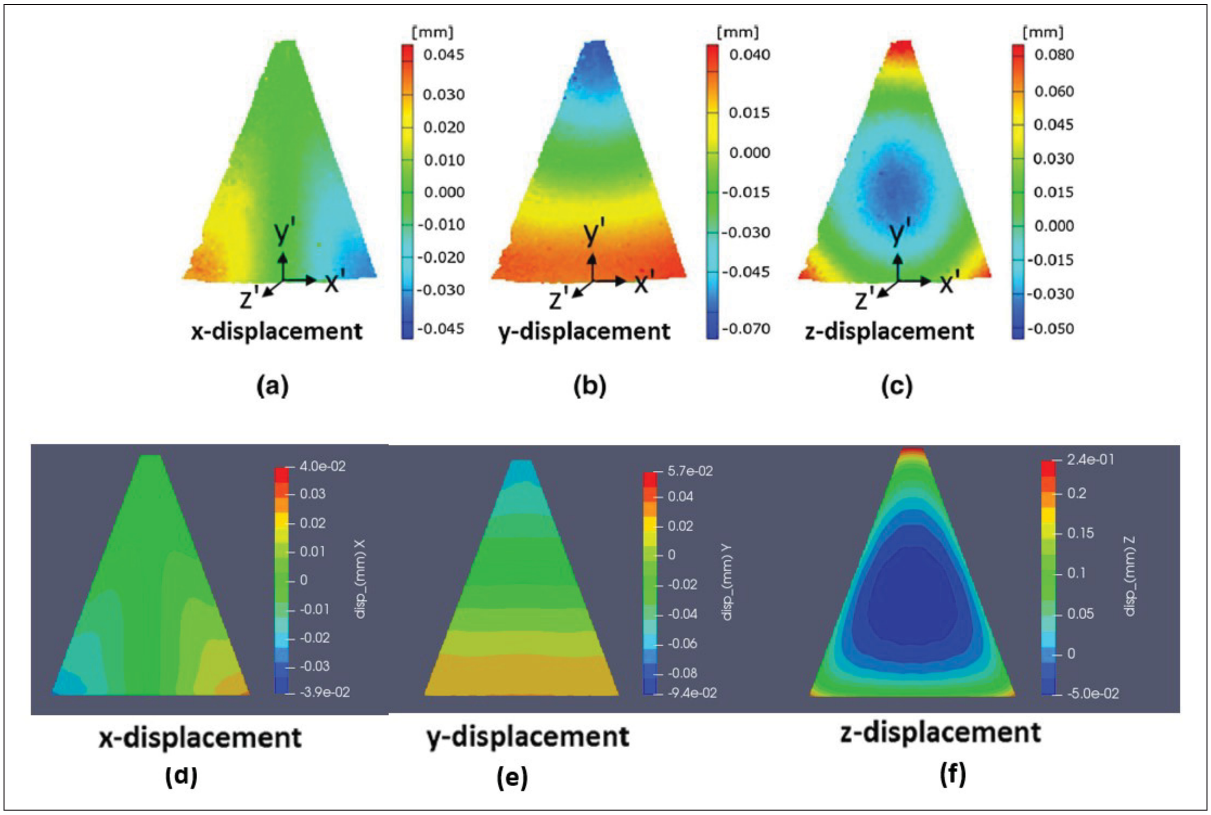

Figure 2.7 Displacements resulting from the removal of the horizontal prism from its base: (a), (b) and (c) – experimental results of the displacement along the x, y and z axes, respectively; - (d), (e) and (f) – displacement results along the x, y and z axes, respectively, obtained by calibrated simulations in ANSYS Additive

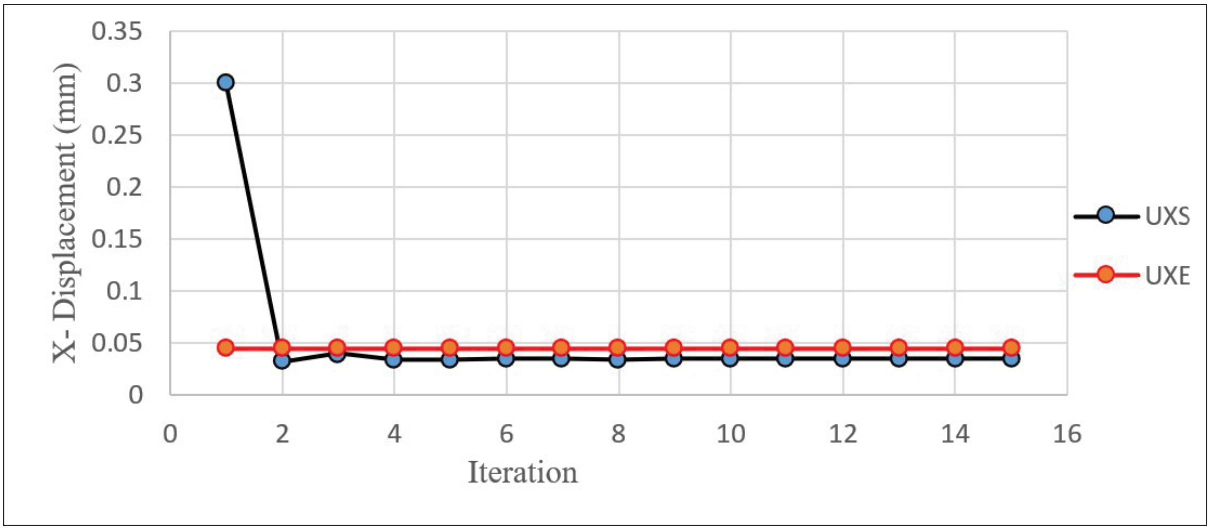

Figure 2.8 Evolution of the maximum displacement of the horizontal prism along the x-axis with the number of iterations

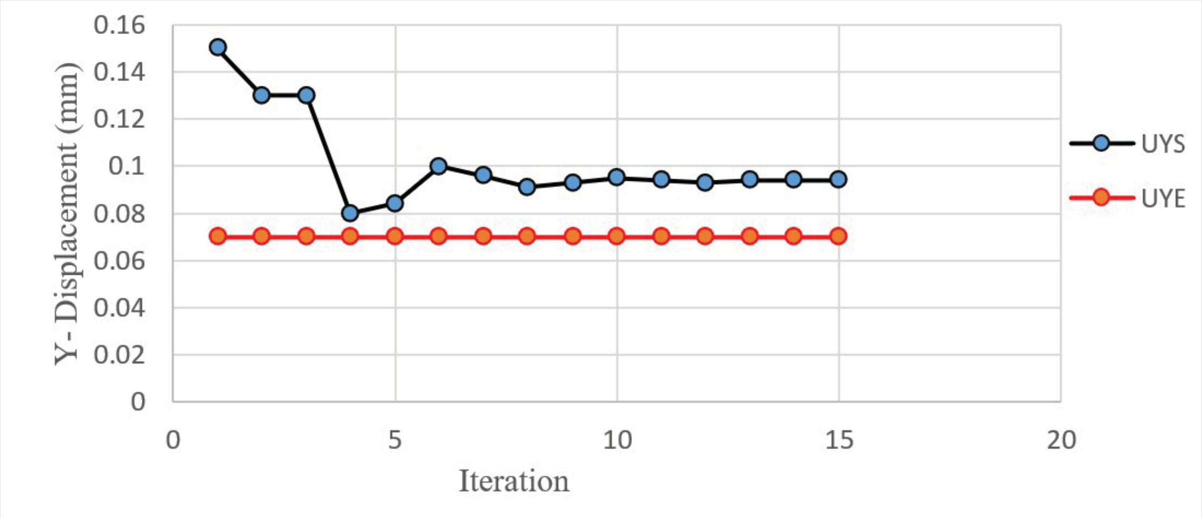

Figure 2.9 Evolution of the displacement of the horizontal prism along the y-axis with the number of iterations

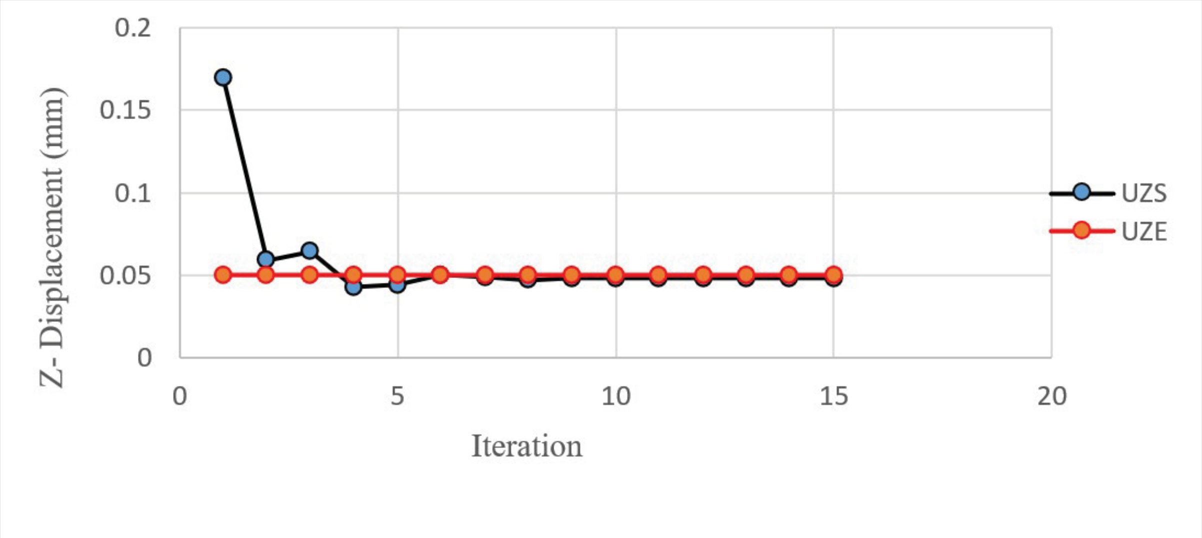

Figure 2.10 Evolution of the displacement of the horizontal prism along the z-axis with the number of iterations

Fig 2.11 shows that the displacement distribution along the z-axis that we obtained with the medium mesh is closer to the distribution obtained experimentally than that obtained by (Hodge *et al.*, 2016). With respect to the displacement amplitudes, we obtained a good prediction of the maximum displacement in compression (0.05 mm), which is equal to the experimental value

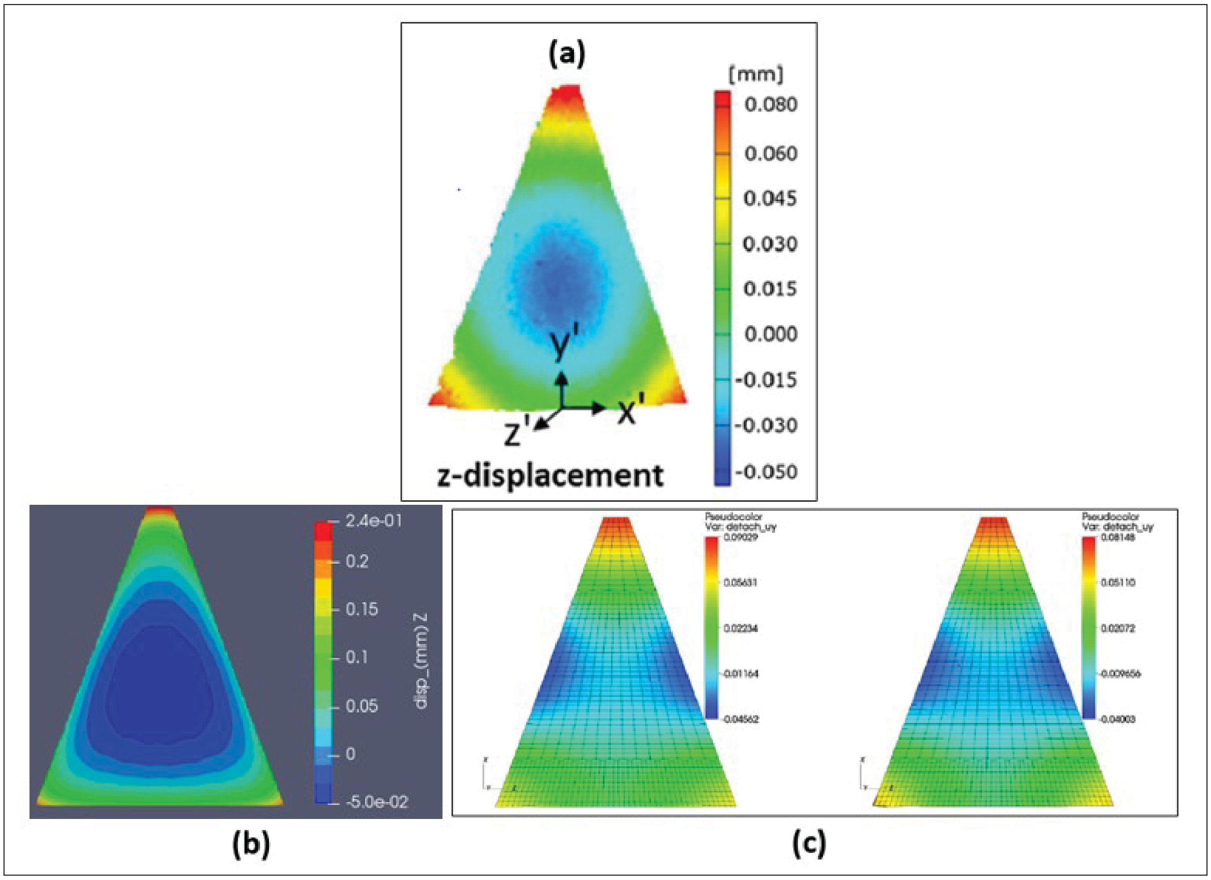

Figure 2.11 z-axis displacements after moving the horizontal prism from its base: (a) experimental z-axis displacements, (b) z-axis displacements obtained in the present study using the medium mesh, and (c) numerical z-axis displacements obtained by Hodge *et al.* (2016, p. 164)

(0.05 mm) and close to the maximum displacement in compression (0.04562 mm). However, the amplitudes found by (Hodge *et al.*, 2016) seem to be closer to the experimental amplitudes than ours for the maximum amplitude in traction. Our calibration method does not take into account the values of tensile displacements, since it is based solely on the values of displacements in compression. This limitation makes its prediction of the maximum displacement in traction further from the experimental value. The Ansys additive uses an adaptive mesh refinement technique during the laser movement where as the (Hodge *et al.*, 2016) used a staggered mesh . The staggered mesh reduces the simulation complexity but the computation cost will increase if make the decrease in mesh size. (Hodge *et al.*, 2016) did not present the x- and y-axis results; however, we present the results for all three axes (x, y and z) and compare them with the experimental results.

2.4.2.2 Vertical prism

We used the new calibration formulation for the following tests on the vertical prism displacement. As shown in Fig 2.12, this calibration allowed us to obtain convergence. Table 2.4 summarizes the comparison.

Table 2.4 Comparison of numerical and experimental results for the vertical prism

Mesh size 0.30mm	**UXmin**	**UXmax**	**UYmin**	**UYmax**	**UZmin**	**UZmax**
Wu *et al.* (2014).	-0.009	0.009	-0.025	0.025	-0.00427	0.00657
Present results	-0.0087	0.0085	-0.012	0.034	-0.007	0.0067
Hodge *et al.* (2016)	-0.01079	0.01088	-0.01428	0.01405	-	-

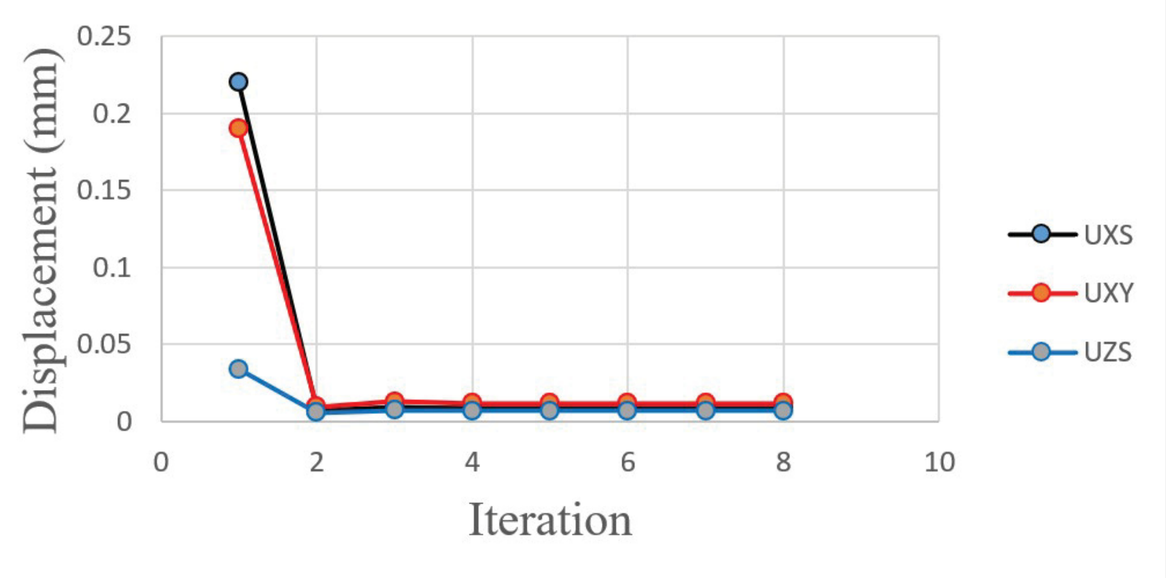

Figure 2.12 Evolution of the maximum displacements of the vertical prism using the proposed calibration procedure

Fig 2.13 shows the displacements in the x, y and z directions associated with the removal of the vertical prism from its base. The final anisotropic coefficients obtained were 0.485 along the x axis, 1.515 along the y axis and 1 along the z axis. The strain scaling factor (SSF) used for our results was 0.107.

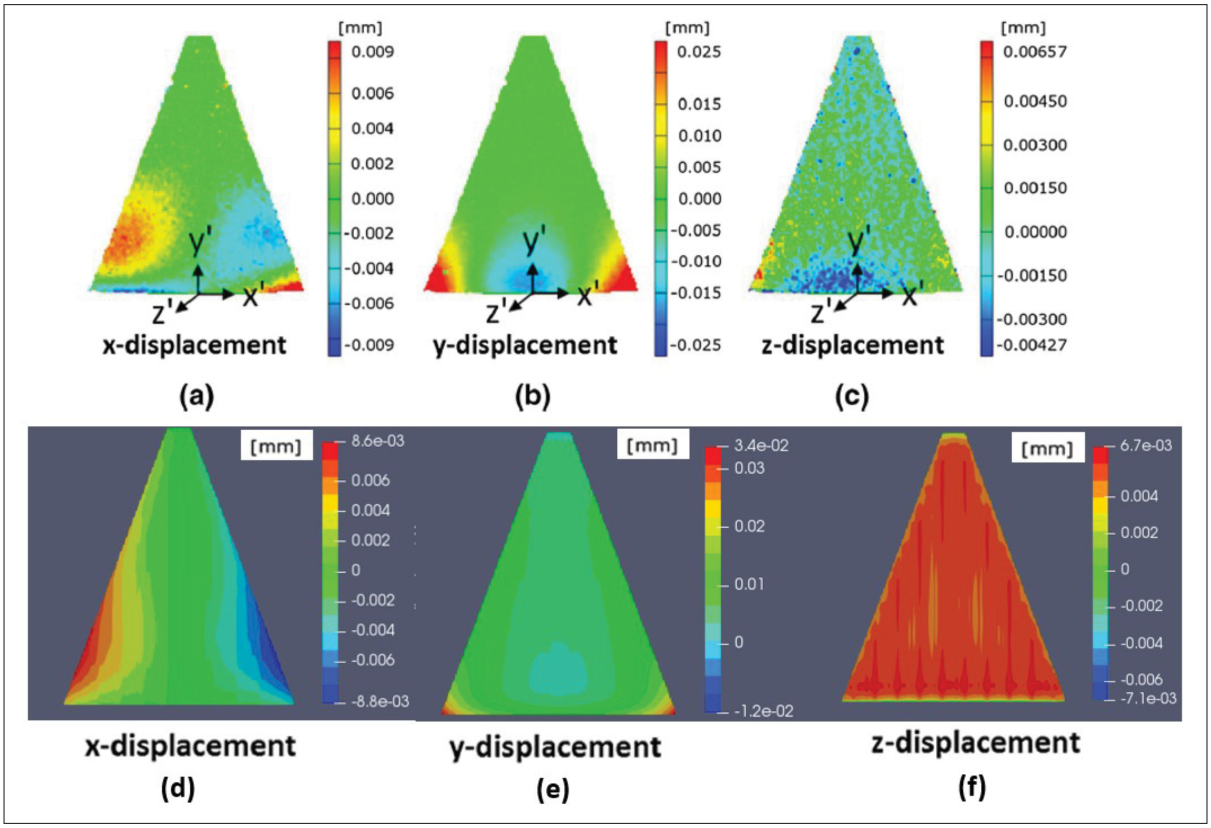

Figure 2.13 Displacements after moving the vertical prism from its base: (a), (b) and (c) – experimental displacements in the x, y and z directions, respectively; (d), (e) and (f) – predicted displacements in the x, y and z directions, respectively (mesh size = 0.30 mm)

In Fig 2.13, we can observe that the numerical result distributions correspond well to those of the experimental results, although the amplitudes of displacement are not always as close as we wish. There is clearly a good displacement prediction for the x-component (for both distribution and amplitude). For the z-component, there is a good prediction for the amplitude, but the distribution for the experimental case seems not to be well reproduced. We further present a comparison between our results and those of Hodge *et al.* (2016). It is clear that the distributions and the amplitudes obtained in the present study for x-displacements (Fig 2.14) are closer to the experimental ones than those obtained by Hodge *et al.* (2016). The amplitudes of the y-displacements of Hodge *et al.* (2016) are symmetrical, as is the case for those obtained experimentally, but our distribution does not provide symmetrical amplitudes in traction. This observation is very likely due to the island scanning strategy used in Hodge *et al.* (2016); our study uses ANSYS-Additive 19.2, in which it is not possible to use such a strategy. It is not possible to present the comparisons for the z-displacements here because they are not shown in Hodge *et al.* (2016).

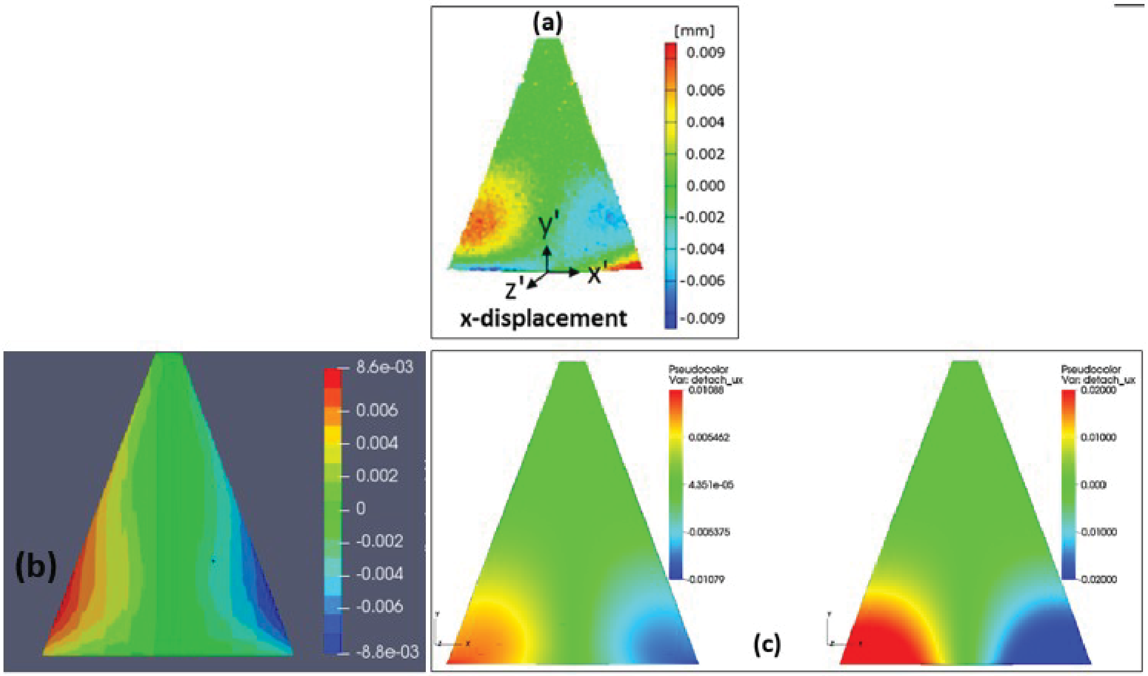

Figure 2.14 x-axis displacements after moving the vertical prism from its base: (a) experimental x-displacements, (b) numerical x-displacements obtained in the present study, and (c) numerical x-displacements presented in Hodge *et al.* (2016, p. 161)

2.4.2.3 The L-shaped cross-section

The dimensions of the sample are shown in Fig 2.16; the manufacturing direction (z-axis) is normal to the L-shaped cross-section. For this case, the measured normal stresses σ_{zz} are at the level (z = 15 mm) and are given in Wu *et al.* (2014). As shown in Fig 2.16, most of the section is in compression and the maximum stress is around -200 MPa in both the experimental and the simulation results. There is clearly a similarity between the stress distributions of these two results. While the maximum stress in compression is similar in both cases, there are differences

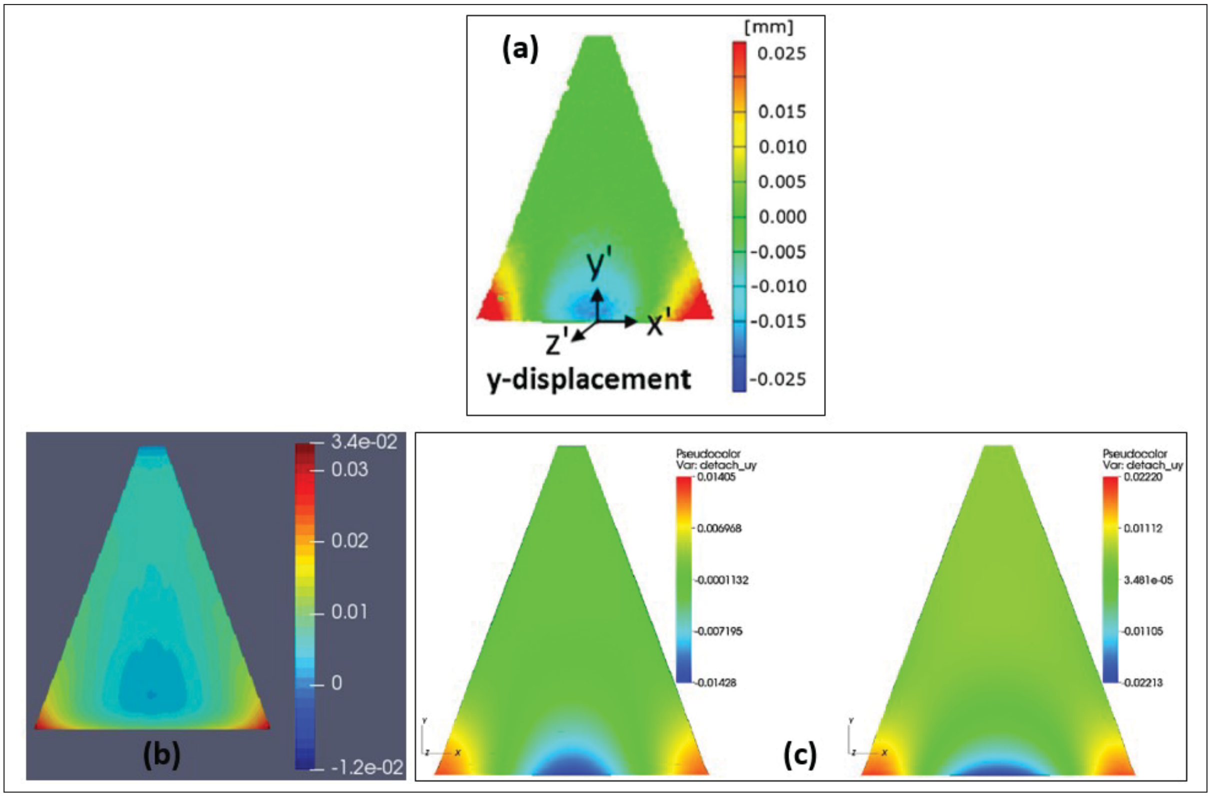

Figure 2.15 y-axis displacements after moving the vertical prism: (a) experimental y-axis displacements, (b) numerical y-axis displacements obtained in the present study, and (c) numerical y-axis displacements presented in Hodge *et al.* (2016, p. 162)

in the maximum tensile stress.

It should be noted that in addition to predicting displacements and constraints, the ANSYS-Additive software used in this study is able to generate compensated geometries that take into account residual distortions and stresses, as well as optimized geometries of the supports required for obtaining a good quality piece at the end of the additive manufacturing process. Another advantage is that it not only makes it possible to visualize the deformed part after fabrication, it also allows the visualization of the distortions and the residual stresses layer by layer during the manufacturing process, thereby making it possible to observe the zones of greater deformations.

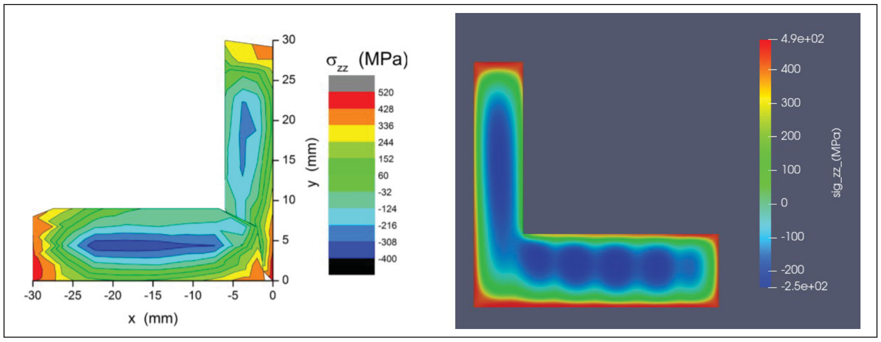

Figure 2.16 L-shaped cross-section displacement: (a) axial constraints obtained by simulation in ANSYS Additive at Z = 15 mm, (b) experimental axial residual stresses measured at Z = 15 mm

In the appendix, some plots of the displacements and stresses along cuts are presented to serve as quantitative comparisons for future comparisons.

2.4.3 Mesh convergence analysis

We can show that the mesh size chosen is acceptable by comparing the results obtained with two other meshes of different sizes. It is important to mention that the mesh size of 0.22 mm is the minimum size recommended by the ANSYS-Additive software to obtain reasonable results while considering the capacity of our computing computer. However, while it is possible to set mesh sizes smaller than 0.22 mm, it is not recommended, as it may introduce errors. Our convergence study focuses on three mesh sizes: 0.22 mm, 0.3 mm and 0.35 mm.

2.4.3.1 Case of horizontal prism

As we can see in Table 2.5, the values of the displacements do not vary much with changes in the mesh size. We choose the size 0.3 mm to display our results.

Table 2.5 Mesh convergence study of horizontal prism

Mesh size (mm)	UXS	UYS	UZS	Number of iteration
0.22	0.09	0.093	0.05	8
0.3	0.039	0.094	0.05	12
0.35	0.035	0.093	0.044	18

2.4.3.2 Mesh convergence study of vertical prism

As we can see in Table 2.6, the values of the displacements do not vary much between the different mesh sizes

Table 2.6 Mesh convergence study of horizontal prism

Mesh size (mm)	UXS	UYS	UZS	Number of iteration
0.22	0.0086	0.012	0.0068	7
0.3	0.0087	0.012	0.007	10
0.35	0.0088	0.012	0.0072	14

2.5 Conclusion

After a literature review on the main challenges faced in the numerical modeling of the SLM process, this paper uses experimental data to validate the ANSYS-Additive package. The definition of the process and the material properties' values are crucial for obtaining accurate results. This work proposes a new calibration technique for these parameters when experimental data are available. The validation tests presented in this study are based on experimental data from the work of Wu *et al.* (2014). Three geometries are simulated. The displacement and the stress analysis of the SLM products show a good comparison between the numerical and the experimental results. It is important to mention that the simulations were executed with some simplifications, such as the scan strategy used in the process is monolithic serpentine instead of island strategy; the latter was used in the actual experiments. Such approximations give rise to some discrepancies.

The new calibration strategy significantly improves the convergence time, and the results are close to the experimental values. The relaxation factor is considered to be 3/4, which helps to consider the deformation history of the product in order to calculate the new SSF and the anisotropic coefficients for the next iteration. To visualize the deformations and the stresses in more detail, a region is considered in all three specimens. Appendix A provides a visualization of the associated deformations. Future work will involve an analysis of the effects of the process parameters using machine-learning algorithms.

CHAPTER 3

A COMPARATIVE STUDY OF MACHINE LEARNING METHODS FOR COMPUTATIONAL MODELING OF THE SELECTIVE LASER MELTING ADDITIVE MANUFACTURING PROCESS

Shubham Chaudhry[1] , Azzeddine Soulaimani[1]

[1] Département de génie mécanique, École de Technologie Supérieure,
1100 Notre-Dame Ouest, Montréal, Québec, Canada H3C 1K3

Paper published in *Advances in Additive Manufacturing Technology, Applied Sciences*,
February 2022

Abstract

Selective laser melting (SLM) is a metal-based additive manufacturing (AM) technique. Many factors contribute to the output quality of SLM, particularly the machine and material parameters. Analysis of the parameters' effects is critical, but using traditional experimental and numerical simulation can be expensive and time-consuming. This paper provides a framework to analyze the sensitivity and uncertainty in SLM input and output parameters, which can then be used to find the optimum parameters. The proposed data-driven approach combines machine learning algorithms with high-fidelity numerical simulations to study the SLM process more efficiently. We have considered laser speed, hatch spacing, layer thickness, Young modulus, and Poisson ratio as input variables, while the output variables are numerical predicted normal strains in the building part. A surrogate model was constructed with a deep neural network (DNN) or polynomial chaos expansion (PCE) to generate a response surface between the SLM output and the input variables. The surrogate model and the sensitivity analysis found that all five parameters were important in the process. The surrogate model was combined with non-intrusive optimization algorithms such as genetic algorithms (GA), differential evolution (DE), and particle swarm optimization (PSO) to perform an inverse analysis and find the optimal parameters for the SLM process. Of the three al-gorithms, the PSO performed well, and the DNN model was found to be the most efficient surro-gate model compared to the PCE.

keyworks

Selective laser melting; Additive manufacturing; Optimization; Surrogate model; Polynomial chaos expansion; Deep learning networks.

3.1 Introduction

Selective laser melting (SLM) is an additive manufacturing (AM) process in which a 3D structure is constructed by successively melting material powder layers. The SLM process uses a high-energy laser beam to melt the powder, making it accessible to different materials, including metals. This technique can help to construct lighter, more complex geometries that are more robust, without any significant material wastage. Due to such advantages, SLM technology has increased in popularity and has made its way into large manufacturing industries such as aerospace, medical implants, automobiles, etc. Ngo *et al.* (2018). However, many challenges are associated with SLM products, including dimensional accuracy, part distortion, premature process termination, and mechanical properties, thus requiring further research and analysis (Ngo *et al.*, 2018) (Abdulhameed, Al-Ahmari, Ameen & Mian, 2019).

Additive manufacturing (AM) efficiency and accuracy can be improved by using suitable material and process parameters. Broadly, the properties of a material, the process, and the environment define a large number of the parameters which affect the final product (Bian, Shamsaei & Usher, 2017) , including laser speed, layer thickness, chamber temperature, etc. Therefore, it is important to understand each parameter's impact on the AM process; there could also be possible interactions between the parameters. To meet specific design requirements in the AM, these material parameters and the process parameters may need to be optimized. SLM is a multiphysics process that occurs over different time and length scales (Markl & Körner, 2016). Among the major physical phenomena that occur during the process are radiation, convection phase change, absorption and phase change, etc. (Tapia & Elwany, 2014). Our understanding of the SLM process can be improved by using the design of experimental methods (Tapia & Elwany, 2014). However, experimenting on a large scale is time-consuming and costly. Such challenges can be addressed using a realistic numerical model of the process. A numerical model can help us generate a large number of data sets at a significantly lower cost than traditional experimental methods. However, SLM involves complex multiphysics and multiscale phenomena (Markl & Körner, 2016) with many uncertainties, from the material powder bed to the melting and solidification processes. These uncertainties come from an insufficient understanding of the process, measurement error, scaling error, sampling error, and lack of information about the material properties (Hu & Mahadevan, 2017). All these elements contribute to the model's confidence level, which may limit SLM applications.

To increase the SLM product quality and production, we need to understand the sources of uncertainties; how they grow, and how they affect the final product quality. Two methods can be considered to tackle these issues and to increase trust in the SLM numerical model (Saltelli *et al.*, 2010) or the process: (1) uncertainty analysis (UA), and (2) sensitivity analysis (SA). Uncertainty analysis aids in understanding the uncertainty in model outputs due to the uncertainties in the model inputs; whereas, sensitivity analysis gives insight into how uncertainties in the model inputs and outputs are related to each other. Most of the reported UA and SA methods in AM are experiment-based, which leads to a high material wastage and makes the process expensive (Hu & Mahadevan, 2017). In another approach, numerical models can be used to quantify the uncertainties in the SLM process. However, a full-scale (such as a finite elements-based) model could be computationally expensive and may take hours or days to complete depending on the simulation type. In addition, numerical models are deterministic, and usually do not consider the input variables' uncertainties (Asserin, Loredo, Petelet & Iooss, 2011).

This paper provides a framework to optimize the SLM process and study uncertainty and sensitivity analyses using a data-driven approach along with a 3D finite element model. As the discretization of SLM problems requires fine spatial meshes and a high number of time steps, the overwhelming demand for computational resources makes high-fidelity simulations too expensive computationally in the con-texts of uncertainty propagation or inverse analysis studies. To alleviate this difficulty, we advocate the use of the data-driven approach, which consists of two major stages: (1) A database of high-fidelity solutions computed for a certain number of samples of the input data in the offline stage, which allows a surrogate model to be obtained using a regression method on a reduced basis; (2) Predictions on new data performed on the online stage using the surrogate model.

It is possible to a priori prescribe a reduced basis such as in the well-known polynomial chaos expansion (PCE), or to use neural networks for which the reduced basis is obtained adaptively. The data-driven approach does not require any modification of the high-fidelity source codes; these are used as a black box. However, the solutions da-tabase should be computed in a reasonable timeframe, for which parallel computing is deemed essential. We used PCE and neural network methods to build an efficient ma-chine learning model. Genetic and evolutionary optimization algorithms were then used to find the optimal parameters. These models were validated on a benchmark SLM test (Phan *et al.*, 2019) for which the high-fidelity solutions were obtained using Ansys additive software.

After this introduction, Section 3.2 gives an overview of the mathematical methods used for statistical analysis, surrogate modeling, and optimization. The results of the benchmark test are discussed in Section 3.3. Finally, concluding remarks are given in Section 3.4.

3.2 Mathematical Model

A global sensitivity analysis considers the uncertainty in the input parameters and their influence on the uncertainty of the process output to rank the importance of each input parameter (Bruna-Rosso *et al.*, 2018). In this paper, we have used a variance-based global sensitivity analysis (GSA), which is commonly used to quantify the sensitivity of output to input parameters. The basic concept behind the variance-based method is to decompose the output variance among each model input. To explain the variance-based GSA, let us consider the following model:

$$Y = f(X_1, ...X_p) \tag{3.1}$$

where Y is the system output and $X_1, ...X_p$ represents the independent input variables, which can be defined by a known probability distribution. If we compare this equation with our case, then Y can be seen as the strain value, and the inputs are the machine properties, such as laser speed and layer thickness, etc. To calculate the effect of input parameters X_n on the variance of Y, we assume that the actual value of X_n is x_n^*. The following conditional variance gives the change in the variance of Y:

$$O_{X_{-n}}(Y|X_n = x_n^*) \tag{3.2}$$

In the above Equation, $O_{X_{-n}}$ represents the conditional variance over the $(p-1)$ input parameter space, including all the input parameters except x_{n^*}. As the exact value of X_n is unknown, we will take an average over all the potential values of X_n, which is given by:

$$E_{X_n}(O_{X_{-n}}(Y|X_n)) \tag{3.3}$$

The smaller value of $E_{X_n}(O_{X_{-n}}(Y|X_n))$ represents the greater importance of X_n in the variance of Y. If we use the law of total variance, then we can write:

$$O(Y) = O_{X_n}(E_{X_{-n}}(Y|X_n)) + E_{X_n}(O_{X_{-n}}(Y|X_n)) \tag{3.4}$$

After a normalization, this Equation can be written as:

$$1 = \frac{O_{X_n}(E_{X_{-n}}(Y|X_n))}{O(Y)} + \frac{E_{X_n}(O_{X_{-n}}(Y|X_n))}{O(Y)} \tag{3.5}$$

$$S_n = \frac{O_{X_n}(E_{X_{-n}}(Y|X_n))}{O(Y)} \tag{3.6}$$

S_n represents the first-order sensitivity index for the parameter X_n. The remaining terms in equation 3.6 will help in calculating the total order index. Equation 3.1 is further decomposed into increasing orders of dimension, as:

$$f(X_1, ...X_p) = f_0 + \sum_{i=1}^{p} f_i(X_i) + \sum_{1 \leq i < j \leq p} f_{ij}(X_i, X_j) + ... + f_{1,...,p}(X_1, ..., X_p) \tag{3.7}$$

In the above equation, if we assume that all the input factors are mutually independent, then there exists a simple decomposition where all the terms will be mutually orthogonal, and so the variance of the output $(O(Y))$ can be written as follows:

$$O(Y) = \sum_{i=1}^{p} O_i + \sum_{1 \leq i < j \leq p} O_{ij} + ... + O_{1,...p} \tag{3.8}$$

where $O_i, O_{i,j}, \ldots, O_{1,\ldots,p}$ represents the variance of $f_i, f_{i,j}, \ldots, f_{1,\ldots,p}$, respectively. The first-order sensitivity index shown in Equation (6) can be obtained by using the first p term of the above decomposition.

3.2.1 Surrogate Modeling

A surrogate model is a mathematical representation of the relationship between the input and output parameters; it provides approximate outputs for new input values without explicitly solving the process. In the present study, we have used a deep neural network and polynomial chaos expansion to build our surrogate models.

3.2.1.1 Deep Neural Networks

Deep neural networks (DNNs) are a class of artificial neural networks (ANNs), similar to a human brain's neuronal network. The basic unit of an ANN is called a node, which collects information from one end and passes it to another node at the other end. A node contains the values of inputs, sums their weighted values, and then uses an activation function to produce an output (Goodfellow *et al.*, 2016). A simple structure of a neural network is shown in Figure 3.1a. The nodes are arranged in a number of layers. Each layer is fully connected with its subsequent layer, but the nodes in a layer are not interconnected. The first and last layers of an ANN structure are called the input and output layers. The number of nodes in the input and output layers is equal to the number of input and output variables, respectively. After the first layer, there are one or more layers called the hidden layers (Bishop & Nasrabadi, 2006). A neural network model with more than two hidden layers and many nodes is referred to as a deep neural network (Singh, Pal, Yadav & Singla, 2020). The values from each layer are mapped to the nodes in the successive hidden layers by being multiplied by some weights. The new value in each node is given by the equation:

$$d_j^k = g(\sum_{i=1}^{n} W_{ji}^k x_i + b_j^k) \tag{3.9}$$

where k represents the number of layers and W_{ji}^k are the weight parameters associated with each node i whose state is given by x_i. The g is the activation function that helps to introduce the non-linearity and b_j^k are the biases parameters. The sigmoid and hyperbolic tangents are the most widely used activation functions. Once the activation function is selected, we need to determine the optimal weights and biases by minimizing the loss function. The mean square error (MSE) is used as a loss function in the present study:

$$MSE = \frac{1}{N} \sum_{i=1}^{n} \left(\sum_{j=1}^{m} [y_j^i - y_{P,j}^i]^2 \right) \tag{3.10}$$

where N represents the total number of input parameters:$x_P^1, x_P^2, \ldots, x_P^N$. The P represents a dataset for a given input sample vector. The corresponding target outputs are represented by $y_P^1, y_P^2, \ldots, y_P^N$, and $y_{P,j}^i$ represents the desired output. In the MSE equation, a regularization term is added to prevent the neural network model from overfitting. Thus, a complete MSE equation can be written as:

$$MSE = \frac{1}{N}\sum_{i=1}^{n}\left(\sum_{j=1}^{m}[y_j^i - y_{P,j}^i]^2\right) + \lambda \sum_{l,\alpha,\beta}^{2} \tag{3.11}$$

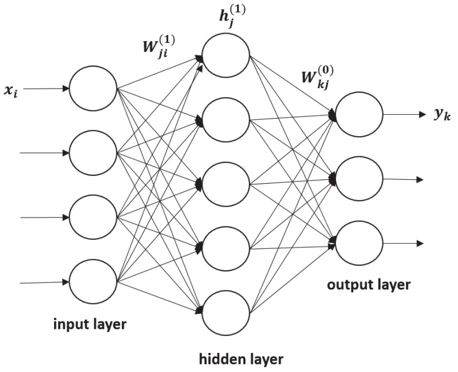

a) Single layer neural network(32)

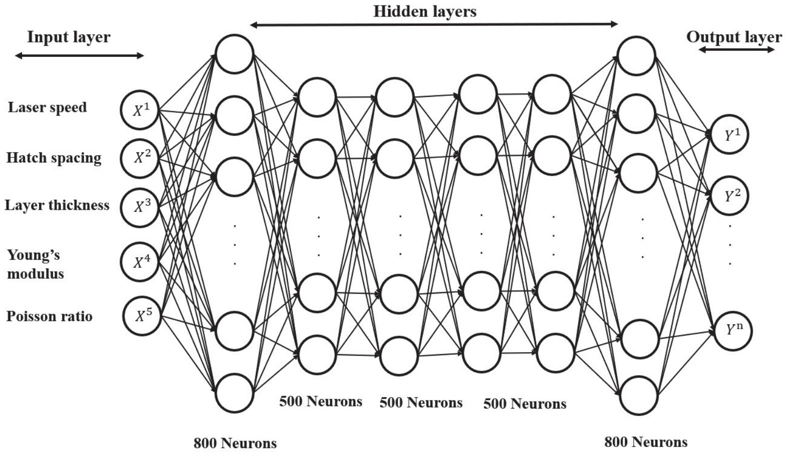

b) six-layers deep neural network used in the present study

Figure 3.1 Pictorial representation of ANN and DNN models

3.2.1.2 Polynomial Chaos Expansion

A polynomial chaos expansion (PCE) is a way of constructing an analytical model that maps the outputs of interest to inputs using a predefined basis of polynomials. The function is represented in the form of a polynomial expansion (Blatman & Sudret, 2010). In a PCE, we assume a deterministic map, M, such that the response is $Y = M(X)$ where $x \in \Re^m, Y \in \Re^n$, m, and n represents the input and output variables respectively For simplicity let us consider n to be 1. The probability distribution of X is given by the probability density function $f_X(x)$ (O'Hagan *et al.*, 2013). Thus, the polynomial expansion of Y can be written as the following equation:

$$y(X) = \sum_{\alpha=1}^{NP} a_\alpha \phi_\alpha(X) \tag{3.12}$$

where a_α represents the expansion coefficients. The value of NP depends on the order of polynomial p and the number of input variables m. Thus, the exact value of NP can be calculated by $NP = \ ((m+p)!)/m!p!$. The other term in Equation 3.12, ϕ_α, represents the multivariant basis functions, which are orthogonal with respect to the probability density function $f_X(x)$, that is:

$$\int_{R^m} \phi_\alpha \phi_\beta f_X(x) dx = \delta_{\alpha\beta} \tag{3.13}$$

Here, $\delta_{\alpha\beta}$ represents the Kronecker symbol. For independent input variables, the value of ϕ_α can be obtained by the tensor product of the univariate orthogonal polynomials $\phi_{p_i^\alpha}(X)$, as in:

$$\phi_\alpha(X) = \prod_1^m \phi_{p_i^\alpha(X_i)} \tag{3.14}$$

where, p_i^α represents the multi-index vector. The univariate polynomial basis function was selected with respect to the type of probability density function. For example, if we have a uniform distribution, the Legendre polynomial is considered the optimal basis function. The PCE coefficient a_α can be computed using a regression approach, by minimizing the mean square error $\sum_{j=1}^{N}(y_D^j - Y(x_D^j))^2 - \gamma a^T)$. Given a dataset D of N input variables $X_D = (x_D^1, x_D^2, \ldots, x_D^N)$ and their corresponding output vector $Y_D = y_D^1, y_D^2, \ldots, y_D^N$, the expansion coefficients can be calculated by solving the following problem:

$$a = (\theta^T\theta + \gamma I)^{-1}\theta^T Y_D \tag{3.15}$$

where γ is the regularization factor, I is the identity matrix and θ is the design matrix, whose components are $\phi_j(x_{D^i})(i = 1, .., N; j = 1, .., NP)$. The total number of sample input points are calculated using $N = \Upsilon NP$, while $\Upsilon \geq 1$ represents the oversampling parameters that control the accuracy of the PCE. To generate the dataset, we can use any sampling method, including Latin hypercube or Sobol (Saliby & Pacheco, 2002). Once we obtain the expansion coefficients, we can use the relationship 3.12 to approximate the outputs for any input variables.

3.2.2 Optimization

To find the optimum parameters for an SLM process, we considered three different optimization algorithms: genetic algorithm, particle swarm optimization (PSO), and differential evolution. These algorithms are briefly described in the following subsections.

3.2.2.1 Genetic Algorithm(GA)

Genetic algorithms(GAs) are search algorithms with the principle of natural selection. The algorithm is inspired by the darwin's theory: of survival of the fittest. At the global level, the population is submitted for many transformations and after some generations, where the population is not enduring anymore, then the best population set is considered to be the best solution. GA compies the working principle of the genetic process, in which the parents' characteristics are transferred to their offspring. These genes correspond to specific characteristics like eys, height etc, and are present in the chromosome. For example, in humans, we have 23 pairs of chromosomes and one chromosome in each pair comes from the maternal side and the other comes from the paternal side. So after crossover, some characteristics of both parents transfer to the child. Also, sometimes there is naturally, some genes randomly mutate and the offspring can have some characteristics different than the parents. These mutation carries the changes in offspring and improves the chance of survivability.

In gradient-based models, the solution runs from one point to another with the help of gradient and the Hessian information (Arora, 2015). However, in GA, one works with a population of points rather than a single point. A GA mimics the genetic process where the characteristics from parents are transferred to the children (Holland, 1992). As shown in the flow chart of a GA presented in Figure 3.2, it is divided into four phases: initialization, fitness, selection, and combination. At the start of the GA, a sample set of the staring population or a sample set is created, and then for each input parameter, their fitness value (the value of the objective function) is computed. The lowest values are taken as the parents' for the subsequent iterations, and they will produce new offspring for the next iteration. Similarly to the human genes, in a GA, individuals with the least function value will undergo crossovers and mutations to produce better offspring than the parents (Wilson & Mantooth, 2013). By better, we mean their function value is less than their parents' function value(s). In our present case, a single-point crossover of 0.8 was established, and the mutation probability was taken as 0.1 to obtain the best results.

3.2.2.2 Particle Swarm Optimization(PSO)

The PSO technique uses a large number of samples to explore the optimal solution, as with GA techniques. A GA is based on a biological evolution process, whereas PSO is based on natural phenomena such as birds flocking or fish moving in a group together. PSO keeps a record of the best position of the individual and of the population using the objective function. In a PSO, 'pbest' and 'gbest' denote the best objective function for the population and for the group, respectively

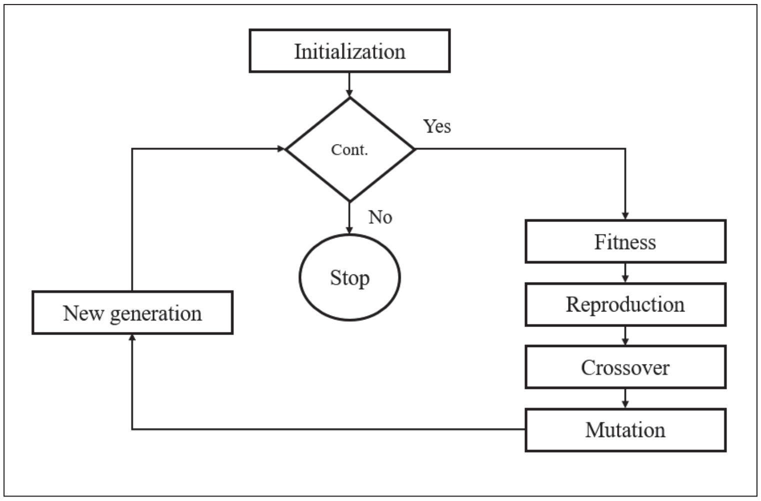

Figure 3.2 Genetic Algorithm

(Arora, 2015). The velocity for each individual in a population is calculated using '$pbest'$', '$gbest'$', and its initial velocity. The new position for each individual is then calculated with the help of the initial positions and their velocity. Each step for the PSO algorithm is described below.

If we assume the 'nth' individual in a set, then its position is given by:

$$x_{i,n} = x_{i,min} + (x_{i,max} - x_{i,min})u_i \tag{3.16}$$

where $x_{i,min}$ and $x_{i,min}$ are the bounds for a variable x_i, and u_i represents a random number between 0 and 1. The fitness value of the nth individual can be calculated by:

$$A_{i,n} = f(x_{i,n}) \tag{3.17}$$

In the beginning, the best fitness value $pbest_{i,n}$ for each individual is $A_{i,n}$ and the global best value can be calculated as:

$$gbest_i = min(pbest_{i,n}) \tag{3.18}$$

The new velocity for the individual can then be calculated as:

$$v_{i+1,n} = \varphi_i v_{i,n} + \psi_1(pbest_{x,i,n} - x_{i,n})u_i + \psi_2(gbest_{x,i} - x_{i,n})u_i \tag{3.19}$$

where φ_1, ψ_1 and ψ_2 are the tuning factors, which are 0.8, 2, and 2, respectively, in our study. Now, the new position can be calculated as:

$$x_{i+1,n} = x_{i,min} + (x_{i,max} - x_{i,min})u_i \tag{3.20}$$

Based on the new position, we can evaluate the new fitness value, which is:

$$A_{i+1,n} = f(x_{i+1}, n) \tag{3.21}$$

If the new fitness value is less than that of $pbest_{i,n}$, then it is replaced with the $A_{i+1,n}$. The global fitness value is computed as:

$$gbest_{i+1} = min(pbest_{i+1,n}) \tag{3.22}$$

3.2.2.3 Differential Evolution (DE)

Differential evolution (DE) is another optimization algorithm that, similar to GAs, is based on an evolutionary process. DE has gained in popularity in recent years for its success in optimization problems in different fields of science and engineering. The algorithm was first introduced by (Storn & Price, 1995) in 1995 to optimize the non-differentiable and non-linear continuous function. DE algorithms are based on stochastic population-driven evolution methods similar to the other evolution methods. This approach uses a population set and searches the whole design space to find the optimal solution using crossover, mutation, and selection operators. One of the differences between DE and the other evolution methods is the mutation strategy used by DE, which applies to each point and explores the whole design space based on other individuals' solutions. (Georgioudakis & Plevris, 2020) presented several DE algorithms based on different crossover and mutation strategies. There are three controlling factors in a DE algorithm: the crossover rate, the population size, and scaling factors, which all must be controlled to get the best performance (Storn & Price, 1997). Figure 3.3 outlines the functioning of a DE algorithm. From mutation to the selection, all steps are repeated until the termination criteria are reached. Our study considers the crossover and the scaling factor to be 0.8 and 0.6, respectively.

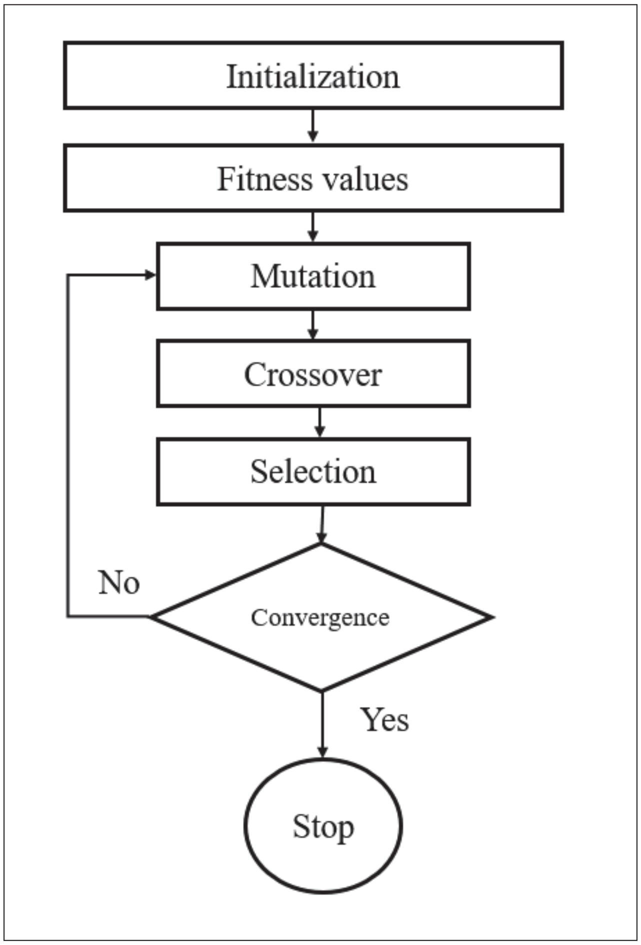

Figure 3.3 Differential Evolution

3.3 Application to an Additive Manufacturing Benchmark Test

To model the SLM process, we used Ansys additive software (ANSYS) that employs a thermo-mechanical coupling method to simulate the SLM process, as shown in Figure 3.4 The heat transfer analysis provides the transient temperature field that is transferred to the mechanical analysis model (ANSYS). The same workbench additive model has been used in many similar studies (Heinrich, Feldhausen, Saleeby, Saldana & Kurfess, 2021) (Weinhold *et al.*, 2021) (Tupac-Yupanqui & Armani, 2021) to validate the code and to optimize the SLM build part.

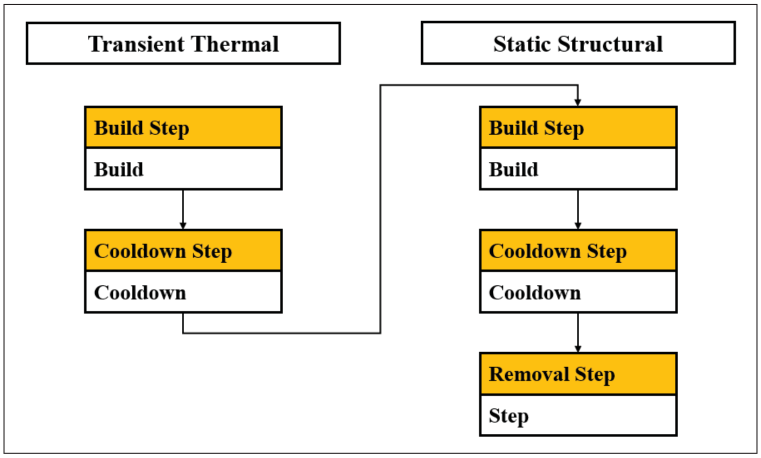

Figure 3.4 Flow chart of Ansys additive simulation

To set up an AM simulation in Ansys, we can either create our geometry in the software or we can import the stl. format of the geometry. In addition, the software gives the freedom to create supports during the simulation, or it can generate them automatically depending upon the given conditions. However, in this study we did not consider any support structure. After the geometry setup, the whole domain was divided into several layers depending on the layer thickness. To simulate each layer, we used the cartesian coordinate mesh with an element birth method to activate the elements in each building step. The numerical model sets the elements in the whole layer to the melting temperature at once, assuming that the developed temperature is always at or above the melting temperature but it does not significantly exceed it. During the melting of the powder, the scan pattern is not considered as an input parameter. Additionally, the unmelted surrounding powder is not explicitly modeled, instead the heat loss between the powder and the solid material boundary is simplified using the convection boundary condition at the interface. A convection boundary condition was used for each heating and cooling step, but the radiation boundary condition is not considered in the model. The powder and the gas convection coefficients were $1.8 \times 10^{-5}\ W/mm^2$ °C and $2.4 \times 10^{-8} W/mm^2$ °C respectively. The pre-heat powder temperature was set at 80 °C whereas, the chamber and the base plate temperature were maintained at 40 °C and 80°C respectively. The other process parameters related to the machine and the material are described in the following subsections. Further details can be found in (Carraturo *et al.*, 2020) (Phan *et al.*, 2019).

To validate the numerical results presented in this work, we compared the strains and the part deflection results with the experimental data of a benchmark case, AMB2018-1, provided by the National Institute of Standards and Technology (NIST) (Phan *et al.*, 2019). In 2018, the NIST provided a set of experimental results for different additive manufacturing processes, including SLM. All the details about the experimental setup and the operations for AMB2018-1 are available on the NIST website (torey.liepa@nist.gov). This benchmark study aimed to provide reliable stress, strain, and deflection benchmark data in a bridge-like structure.

A brief description of this benchmark case, shown in Figure 3.5a,b, is provided here. The residual stress and strain data were measured using x-ray diffraction and neutron diffraction methods. For the part deflection measurement, the bridge was partially separated from the base plate, and then a coordinate measurement machine was used to measure the deflection. The AM part was constructed using two different machines: the NIST in-house-built machine AMMT (additive manufacturing metrology testbed) and the EOS M270. In the present study, we considered only the EOS M270 machine, as the measurement results for the part deflection were not available for the structure constructed with the AMMT. More details on the process can be found in (Phan *et al.*, 2019). The test case comprised four bridge structures on a build plate, as shown in Figure 3.5b. All four bridges and the substrate were constructed using IN625 material with a powder bed fusion process. During the process, the bridges were built with some spacing (Figure 3.5b). As the bridges' construction process does not affect the other bridges' properties, we considered only one bridge on the substrate for our numerical simulations as shown in Figure 3.5c. This simplification significantly reduced the computation time. The bridge and the build plate's final dimensions were 75 × 5 × 12.5 (mm × mm × mm) and 81 × 12.7 × 11 (mm × mm × mm), respectively. Our primary objective was to investigate the strain within the build-part in the validation study. In addition, we verified the geometry deflection in the z-direction after part of the bridge was separated from the substrate.

3.3.0.1 Baseline Machine Parameters

The AM part and the substrate were constructed using a Nickel alloy, IN625. In the experiment, the part was built at the center of the substrate, with odd and even layers that were melted using horizontal and vertical scan strategies. However, because of the software constraint, we only considered the horizontal strategy for all the layers. Table 1 shows the machine parameters that were used during the SLM experiment.

Table 3.1 Machine configuration settings

Machine Parameters	**Values**
Laser Power	195 W
Laser speed	800 mm/s
Hatch spacing	0.1 mm
Layer thickness	0.02 mm
Base plate temperature	80 C°
Chamber temperature	40 C°

3.3.1 Baseline Material Parameters

IN625 is a very common alloy used in manufacturing. Therefore, its properties are easily available and well-known. In this work, we considered the temperature-dependent material properties.

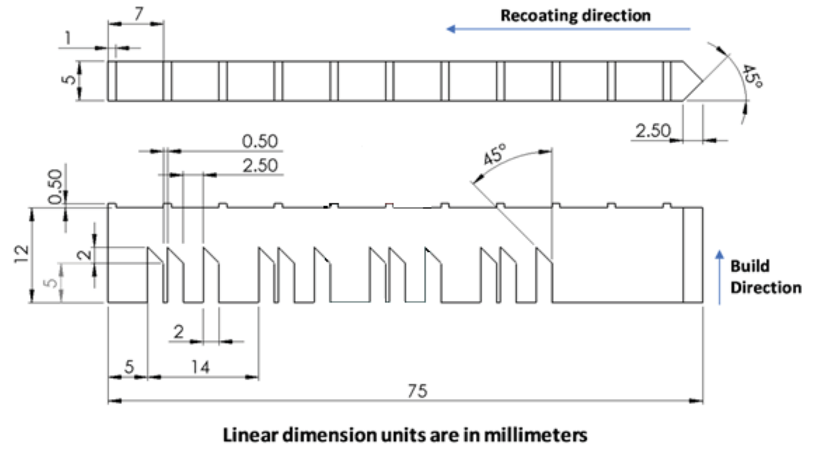

a) Plan (top) and elevation (bottom) views of the AMB2018-01 bridge structure geometry

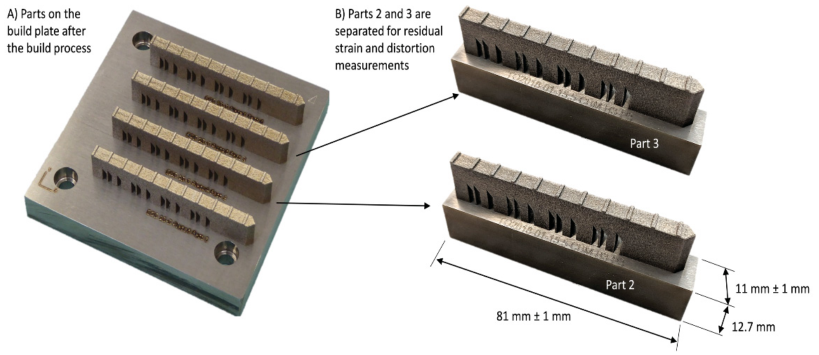

b) AMB2018-01 bridge

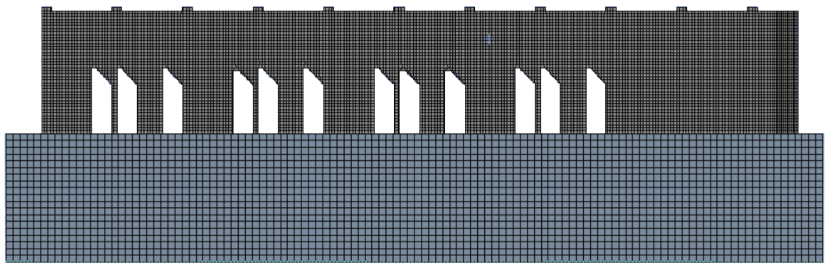

c) AMB2018-01 bridge geometry constructed with Ansys additive software

Figure 3.5 Pictorial representation AMB2018-01 bridge structure

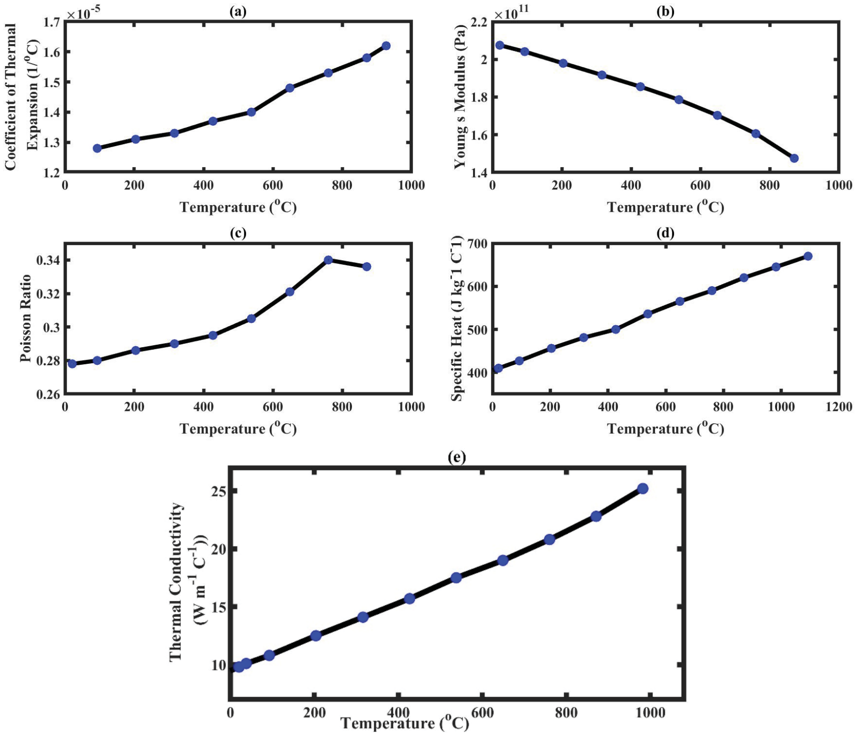

Figure 3.6 Material properties of IN625 (a Nickel alloy)

3.3.1.1 Mesh Convergence Study

A mesh convergence study was first conducted to evaluate the effect of the mesh size of the 3D finite element model on the simulation results. We selected three different mesh sizes, compared their results with the experimental results, and concluded that a mesh of size 0.3 mm was best suited for further studies. The comparison study was conducted using the residual strain results at $z = 9.536mm$. In Fig 3.7, the numerical results are similar to the experimental results. Table 2 presents the decrease in error norm between the experimental and numerical results with mesh size. For the error analysis, we used the L^2 relative error norm which is defined as

$$L^2 = \sqrt{\frac{\sum_{i=1}^{n} (u_E(i) - u - s(i))^2}{\sum_{i=1}^{n} (u_E(i))^2}} \tag{3.23}$$

in which u_E and u_s are the experimental and simulation data, respectively, whereas the total number of data is represented by n. Each simulation was performed on 32 CPUs that each had an Intel E5-2683 v4 processor. From Table 3.7, it is clear that the error decreases with the decrease in mesh size, but at the same time, the computation cost increases. Therefore, we chose a 0.3 mm mesh for our simulations, as it provides better results than the 0.4 mm mesh size, while it is much less computationally expensive than the 0.2 mm mesh size.

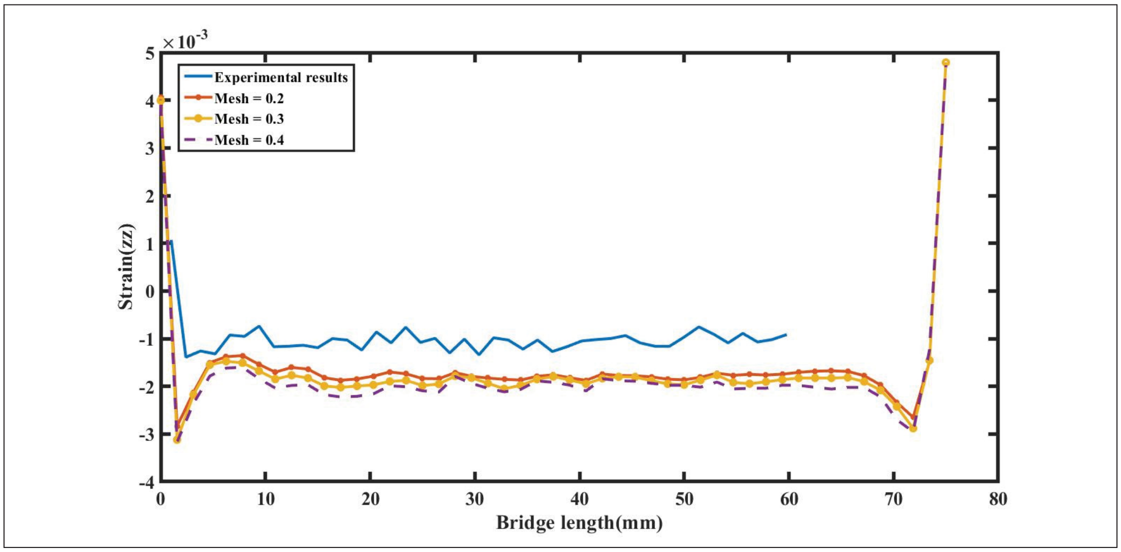

Figure 3.7 Heat transfer during the SLM process

Table 3.2 Discrepancy in different mesh size results

Mesh size (mm)	Relative L2 error Norm	Computation Time(Minutes)
0.4	0.9924	45
0.3	0.9642	60
0.2	0.8588	155

3.3.2 Validation of the Finite Element Model

Using the baseline parameters, the simulation results were validated using two different analyses. In the first case study, the normal residual elastic strains were compared with the experimental results at two specific locations ($z = 9.536 and 2.216$) in the bridge. Figure 3.8 show a comparison of normal strains in the x, y, and z-directions, respectively, at the line $z = 9.536$, whereas Fig 3.9 show that comparison at z = 2.216. The simulation results at both values show a good correlation with the experimental results. It is essential to mention here that the experimental strain results at z = 9.536 were extracted only up to the 60 *mm* length of the bridge. The relative L2 norm error values for the x, y, and z-direction strains at z = 9.536 were 0.4041, 0.6202, and 0.7820, respectively. The small difference in the results may be due to the different scan strategies used in the experimental and numerical simulations.

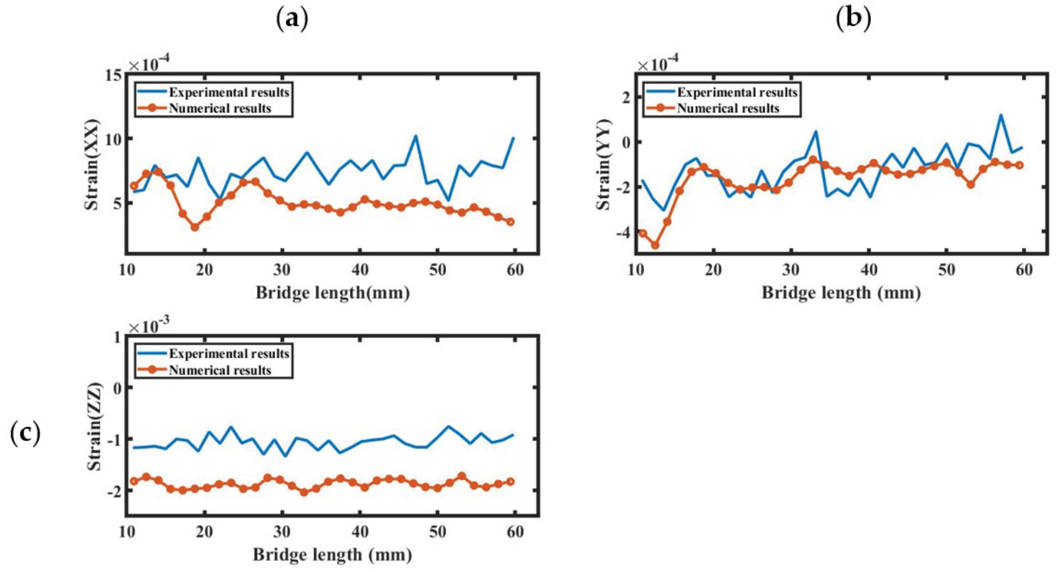

Figure 3.8 The figure a, b and c represents the comparison of experimental and simulation residual strain at z = 9.536 in the x, y, and z-directions respectively

For the second validation case study, we analyzed the deflection of a partially separated bridge from the baseplate as shown in Fig 3.10, in which all 12 bridge legs were separated from the substrate. The partially separated bridge was then allowed to move upwards without any external force, except for the internal residual stresses. The deflection of the bridge in the z-direction was measured at 11 ridges on the bridge's top surface. In Figure 3.11, we show the comparison of the deflection results from a simula-tion and an experimental study. The relative L2 error norm between the simulation and experimental results is 0.0629, proving a good correlation between the results.

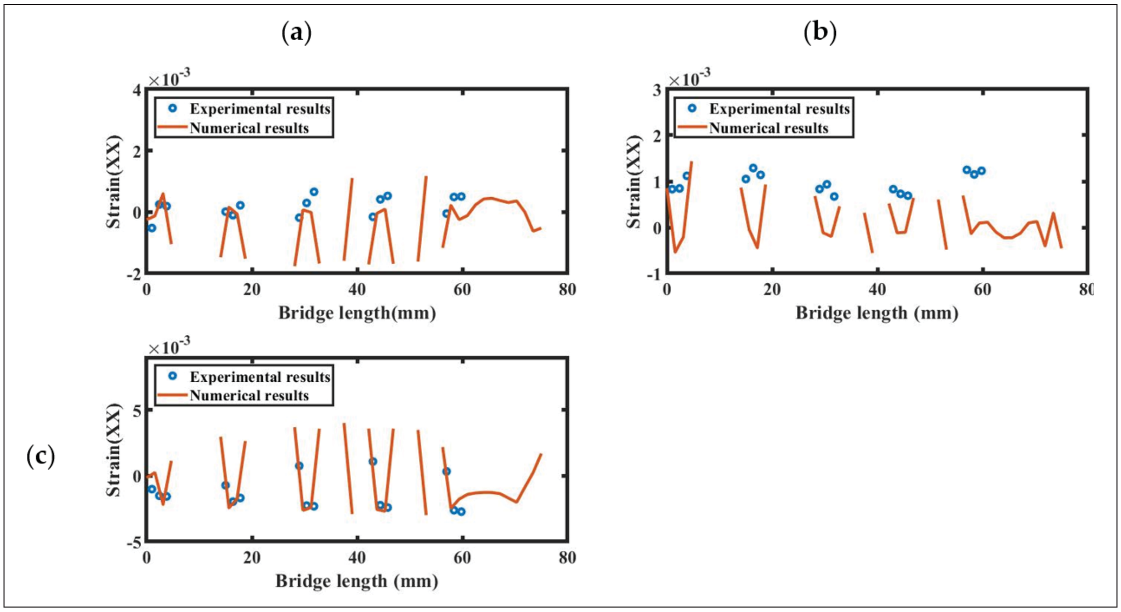

Figure 3.9 The figure a, b and c represents the comparison of experimental and simulation residual strain at z = 2.216 in the x, y, and z-directions respectively

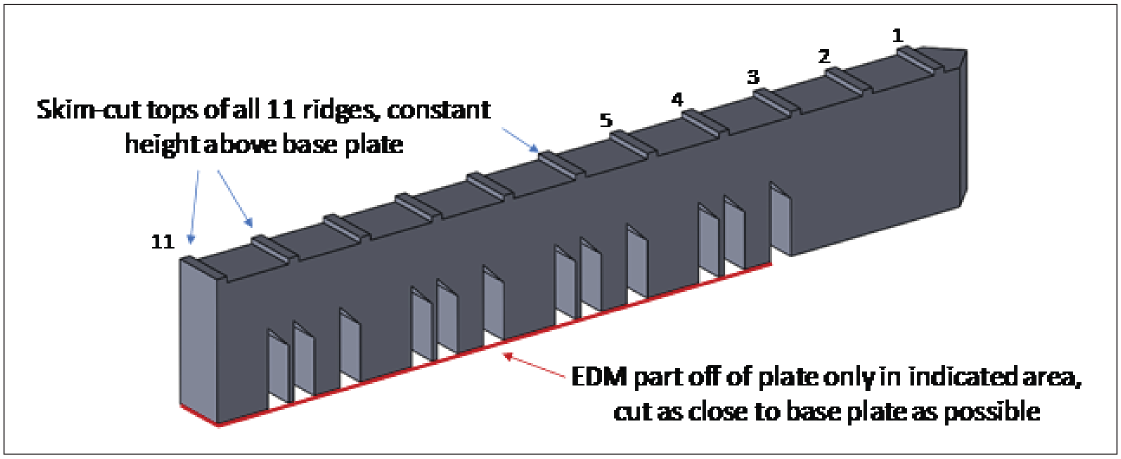

Figure 3.10 The NIST AMB2018-1 bridge geometry

3.3.3 Deep Neural Network (DNN) Surrogate Modeling

A surrogate model was constructed using DNN regression to build a surface map between the input and the output data set. The DNN has six hidden layers, where the first and the last layers

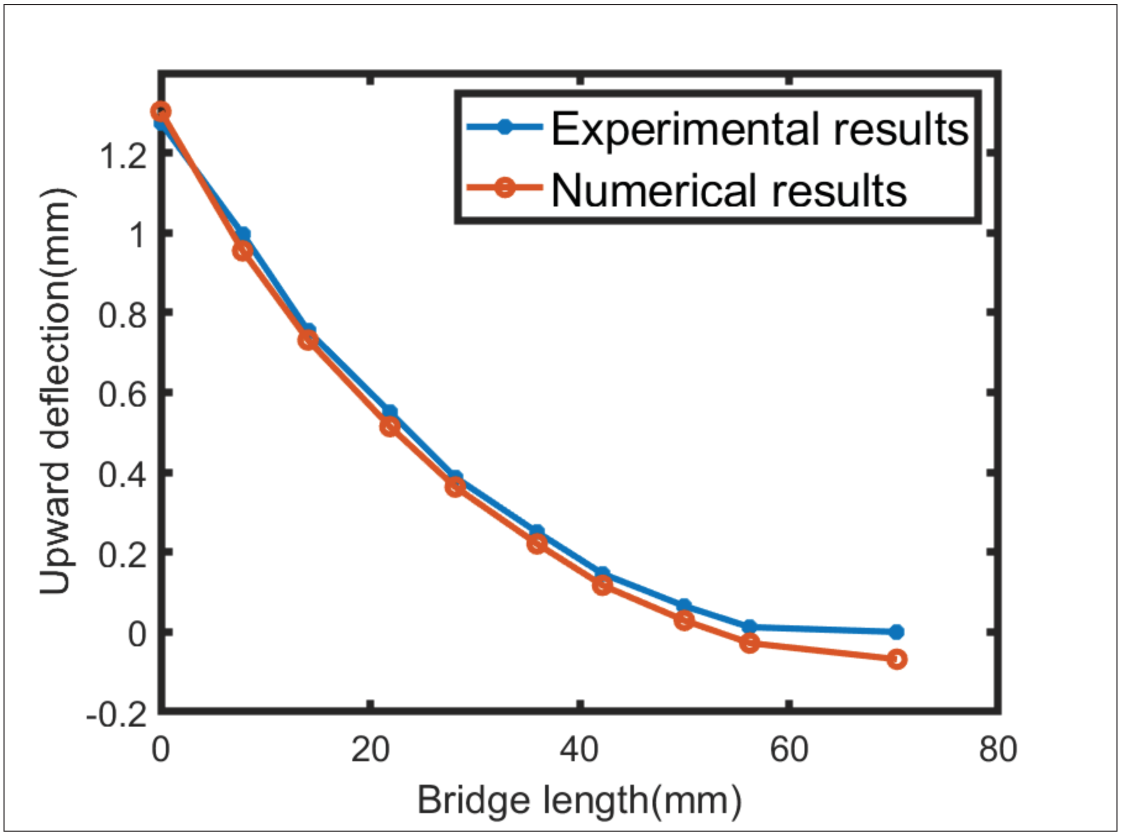

Figure 3.11 Comparison of the part deflection results from experimental and simulation data

have 800 neurons and the middle four layers have 500 neurons each. To construct our DNN model, we used Matlab's deep learning toolbox.

In the present study, we considered five uncertain parameters, where three are the machine parameters and two relate to material properties. To change the values of Young's modulus and the Poisson ratio, we multiplied their baseline values by factors cY and $c\nu$, respectively. The input variables were laser speed, layer thickness, hatch spacing, cY, and $c\nu$. A dataset was generated with a sample of 360 input variables using a Sobol sampling technique. Initially, the sample set responses were obtained using the finite element model, and the normal strains were calculated at z = 9.536 (build direction). Later, the outputs from the 360-sample set were used to construct a DNN model, where 70 percent of the data was used to train the

DNN, 15 percent was used to test it, and another 15 percent was used to validate the DNN model. Fig 3.12 shows the loss drop during training, testing, and validation of the DNN model, and Fig 3.13 shows the plot between the exact and predicted values during training, testing, and validation of the model, using x-strains. The DNN model was developed separately to train and predict the outputs of each normal directional strain at z = 9.536. Fig 3.14 compares the DNN outputs and the simulation outputs for each directional strain at z = 9.536.

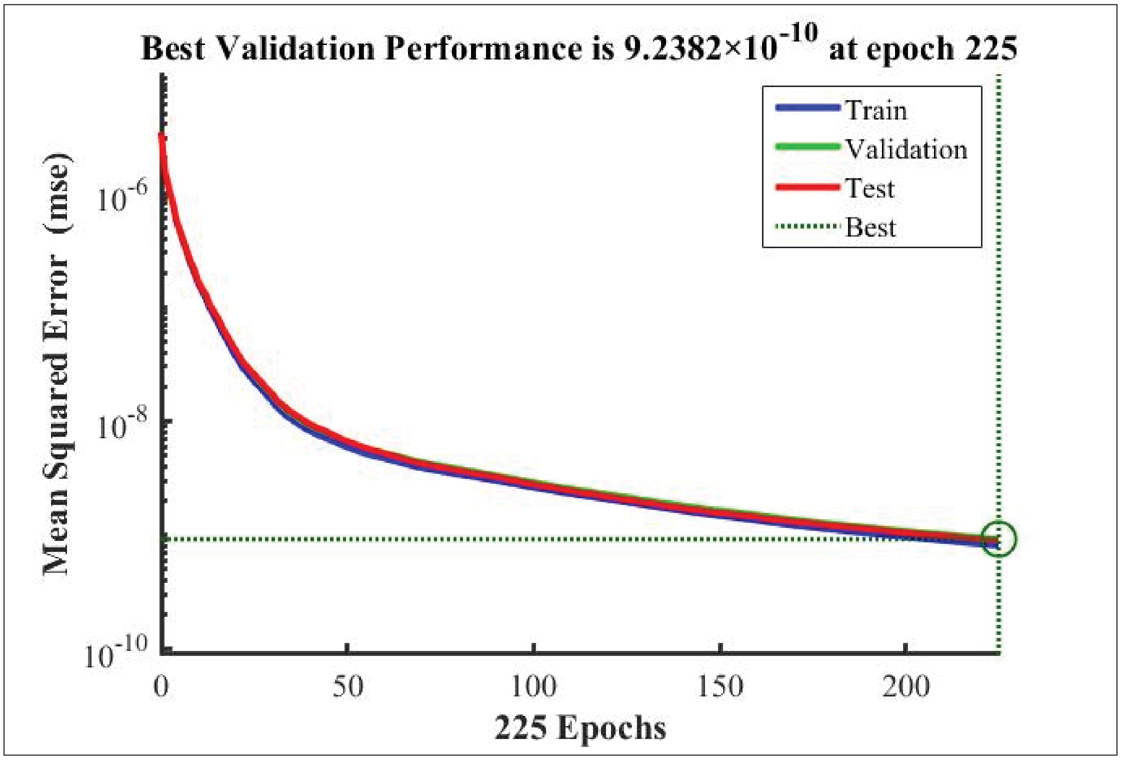

Figure 3.12 Error graph during the training, testing and validation of the DNN model

Once the neural network surrogate model is developed, it can be used to perform statistical and calibration studies. For this purpose, a sample of sufficient size must be generated. We used the Monte Carlo method to perform the convergence analysis using standard deviation (Std) for different numbers of sample sets, including 12, 48, 84, 120, 192, 264, 336, 516, 732, 1020, 1524, 2028, 2532, 3000, 4008, 5016, 8004, and 9588, and the standard deviation was calculated for each sample set. The convergence study was performed for individual directional

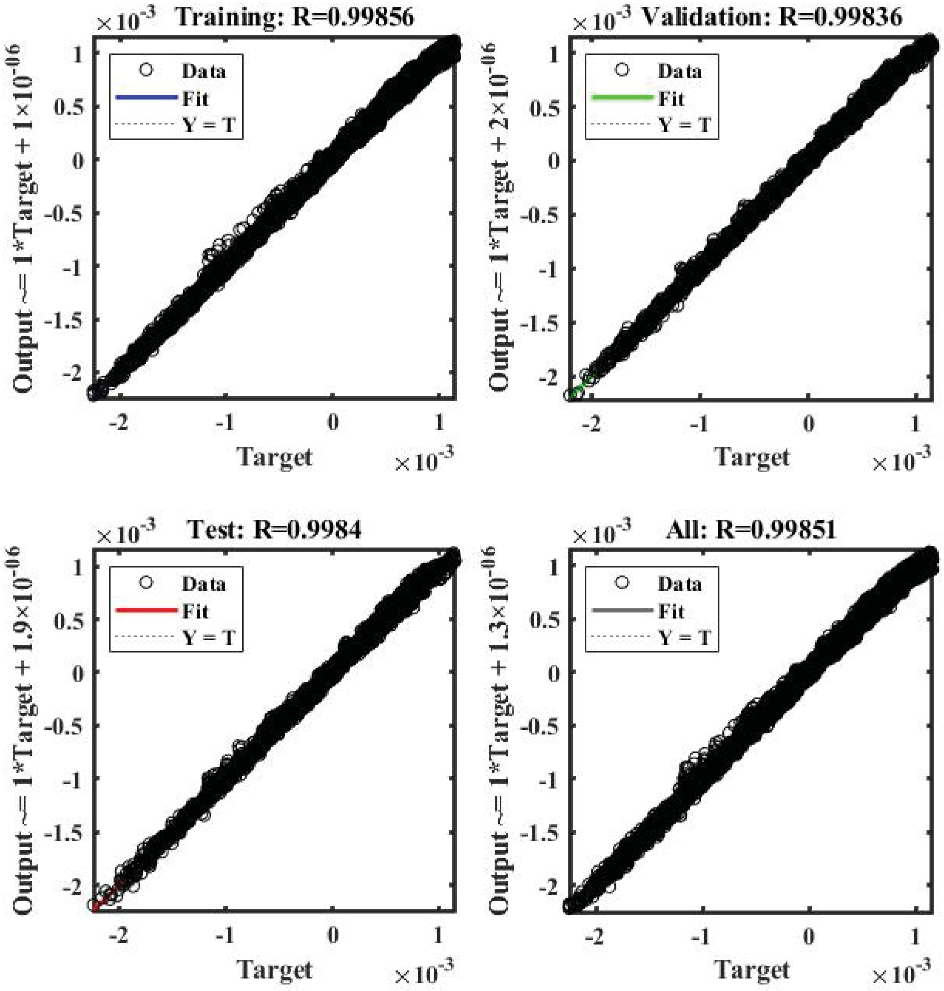

Figure 3.13 Comparison of the exact and predicted results during training, testing and validation of the DNN model

strains at two locations. Fig 3.15a shows the results for the x strain at 15 and 45 mm, while 3.15b and 3.15c present convergence plots for the y and z directional strain at the 15 and 45mm locations, respectively. From the figures, we concluded that a set of 6000 samples was enough to perform the sensitivity and uncertainty analysis for an SLM process, as described in the following sections.

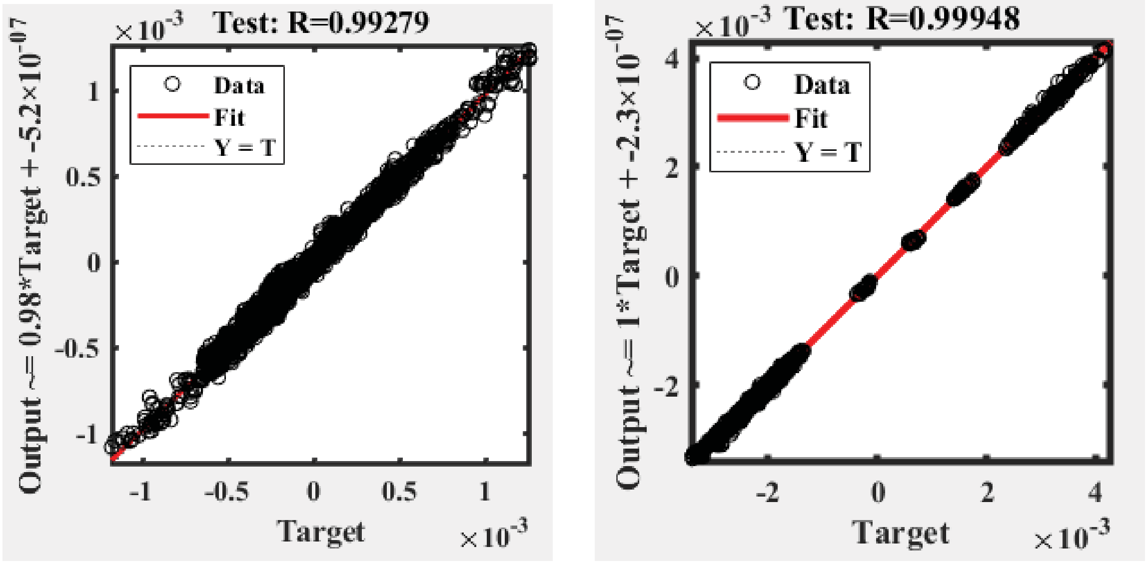

a) DNN Test predictions for y strains

b) DNN test predictions for z strains

Figure 3.14 DNN predictions

3.3.4 Polynomial Chaos Expansion

Along with the DNN, we used a PCE model to construct a surrogate model for our SLM process. We conducted this comparative study to determine the best surrogate model for our problem, one that can simultaneously reduce the computation time and increase the accuracy of the predictions. Thus, similar to the DNN, the PCE was trained and tested with outputs of 360 samples calculated using the Ansys additive software. For the comparison, we generated a data set of 6000 input samples with the Sobol sampling technique, and then used our trained PCE and DNN surrogate models to predict normal strains as outputs for the points at z = 9.536. Fig 3.16 shows a comparison between the DNN and PCE models, and we can conclude that the results are very close to each other. The mean square error between the PCE and the DNN is 7.17×10^{-11}, proving that both models are equally adequate for prediction. In Table 3.3, we present a comparison of the computational cost for both models, and Table 3.4 presents the error between experimental and predicted values. The results show that the PCE is faster than the DNN in training , but almost three times slower than the DNN in prediction. Considering the

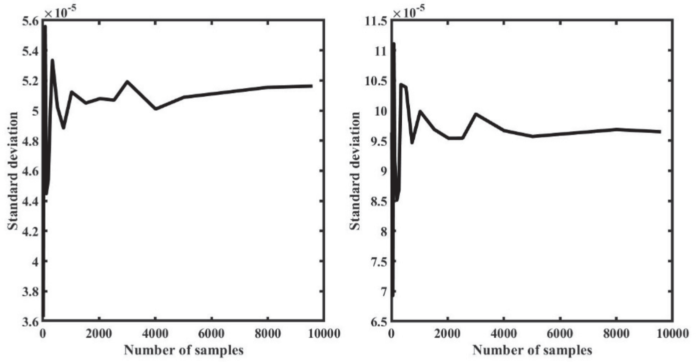

a) Convergence plot at x=15 mm and 45mm for x strains

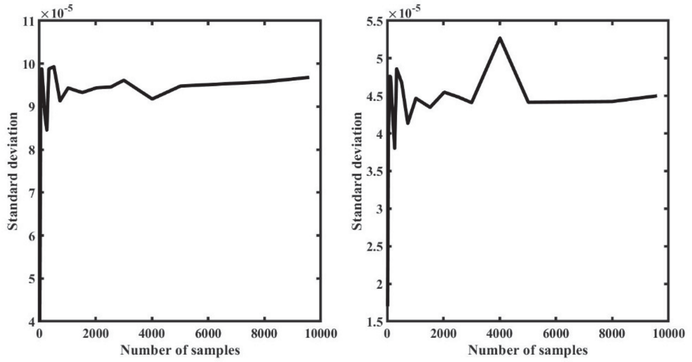

b) Convergence plot at x=15 mm and 45mm for x strains

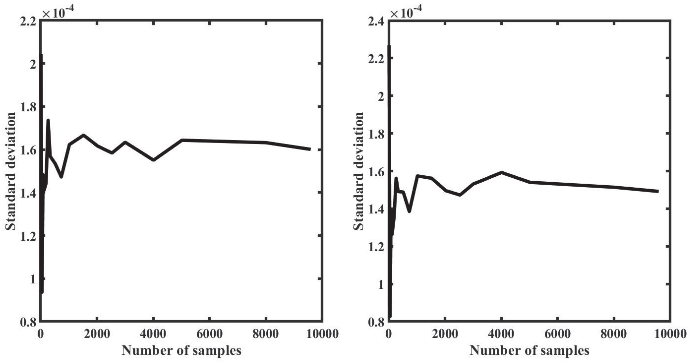

c) Convergence plot at x=15 mm and 45mm for x strains

Figure 3.15 Represent the convergence of standard deviation with the increase in sample size for x, y and z strains

overall time, the DNN is faster than the PCE. Therefore, in conclusion, we proceeded with our investigation using a DNN instead of a PCE.

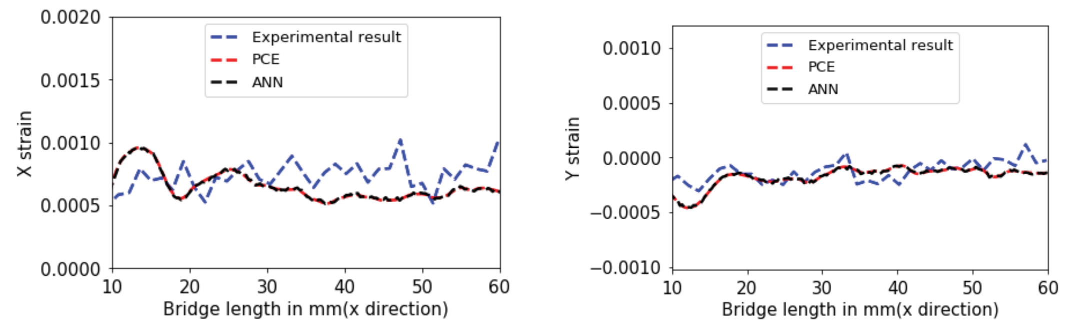

a) PCE and DNN comparison for x strains b) PCE and DNN comparision for z strains

Figure 3.16 Training and prediction time for each model

Table 3.3 Comparison of numerical and experimental results for the vertical prism

	x-strain		**Y-strain**		**Z-strain**	
Methods	Training Time	Prediction Time	Training Time	Prediction Time	Training Time	Prediction Time
ANN	160.09	155.87	115.22	160.81	248.25	156.06
PCE	11.56	515.76	8.14	552.28	7.25	552.26

3.3.5 Uncertainty Quantification

For the uncertainty quantification, we used the normal strains in the x, y, and z directions at z = 9.536. The analysis was conducted using Python libraries, which include Numpy, statistics, and other libraries. To begin, a set of 6000 input samples was generated using a Sobol sampling technique. Next, the trained DNN model was used to calculate the x-directional strains along the line z = 9.536 for these input variables. The samples were generated under ±15% bound on the baseline input values, which are shown in Table 5. As mentioned before, the values of Young's

Table 3.4 L2-error norm between predicted and experimental values

Method	**X-strain**	**Y-strains**	**Z-strains**
ANN	0.2714	0.6583	0.8730
PCE	0.2677	0.6466	0.8640

modulus and the Poisson ratio were modified by multiplying them with the factors cY and $c\nu$, respectively. The values of these factors lie between 0.85 and 1.15, representing ± 15% variation. Figure 18a illustrates the uncertainties in the process outputs, which shows that the mean of the data was very close to the actual results; the grey area represents the confidence interval of 95%. The confidence interval was equal to the ±2x standard deviation. A similar study was performed with y- and z-directional strains at the exact location and their analysis plots are shown in Figure 18b,c, respectively. The L2 error norm between the mean value and the experimental results for Y strains was 0.6662, whereas, for the z strains, the value was 0.8764. The experimental results for Y strains lay in the 95% confidence interval, but for the z strain, they did not. This may be explained by the simplifications and modeling hypotheses used in the numerical software of the model limitations; for example, the model does not consider the anisotropy in the material properties or the laser power.

Table 3.5 Lower and upper bound for the input variables

Input Variables	**Lower Bound**	**Upper Bound**
laser speed	680 mm/s	920 mm/s
layer thickness	0.085 mm	0.115
hatch spacing	0.017 mm	0.023
CY	0.085 mm	0.115
Cν	0.085 mm	0.115

3.3.6 Sensitivity Analysis

For sensitivity analysis, we considered five input parameters: three machine pa-rameters and two material parameters. The study considers the primary parameters of layer thickness, laser speed, hatch spacing, Young's modulus, and Poisson ratio. The input parameters' effects were measured using the normal strains, and by calculating the first-order Sobol indices for each node. Similar to the uncertainty analysis, the normal strains were calculated at z = 9.536 along the bridge direction in each simula-tion.

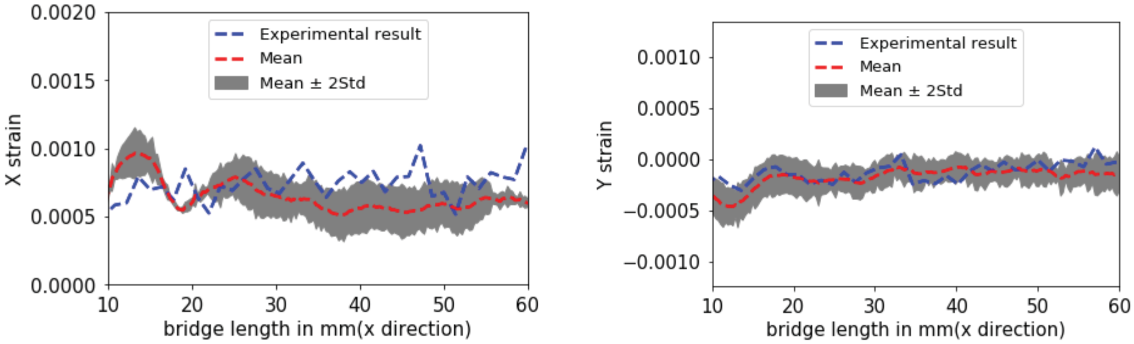

a) Uncertainty propagation along the length of the bridge

b) Uncertainty propagation along the widths of the bridge

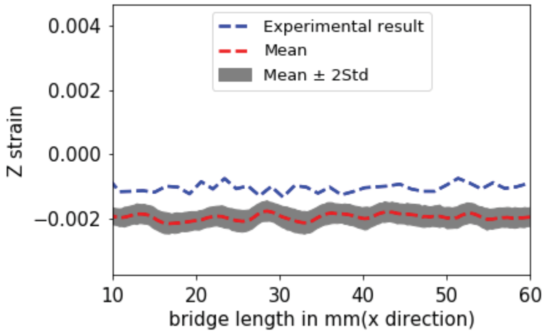

c) Uncertainty propagation along the height of the bridge

Figure 3.17 Uncertainty quantification along the three sides of the AMB2018-01 bridge structure

Fig 3.18 presents the variation in the Sobol indices along the bridge length. A pie chart is provided for each parameter, representing the importance of each parameter as a percentage. From Figure 3.18, we can conclude that the Young modulus and the Poisson ratio are the most critical parameters for the SLM and that hatch spacing is the least important parameter among the five parameters considered. If we consider the x-directional strains, then the Poisson ratio and the Young modulus are the most im-portant parameters. While both parameters' influence changes along the bridge length, both contribute 30% to 65% in the SLM output. The three machine parameters are less influential than the material parameters, but they contribute significantly to the directional strains. Fig 4.8b shows the effect of input variables on y-directional strains, indicating that the Poisson ratio is the most dominating factor among the input varia-bles. The

Poisson ratio contributes between 86 and 90% in the y-directional strains. The other four parameters are equally essential and make contributions of 2 to 5% to the normal strain in the y-direction. However, the situation is the opposite in the case of z strains, where the most dominating factor is Young's modulus instead of the Poisson ratio. Young's modulus is 65 to 68% more important than the other parameters for z strains, while the Poisson ratio is the second most dominant factor.

If we look at all the results we find that the machine parameters are less influen-tial than the material parameters. However, the machine parameters' effects are still significant in the SLM process. Thus, we cannot ignore their importance in the SLM output, and we need to consider these machine parameters to optimize the SLM out-put. In the next section, we consider all five parameters and perform an optimization analysis to find the best configuration of the input variables to obtain the optimal SLM to build-part.

3.3.7 Optimization

We performed an optimization analysis to find the optimized parameters for an SLM process, using GA, PSO, and GE as our optimization algorithms, and the ANN model to generate the required data set for the optimization process, as it is faster than the PCA model. From our sensitivity analysis, we found that all five parameters are es-sential for the process, and so we considered all five parameters as the input variables. We used 100 as the initial population for the GA algorithm, with 0.8 and 0.1 as the crossover and the mutation probability, respectively. However, in the DE, we took 0.6 for the scaling factor and 0.8 for the crossover. Table 3.6 presents the optimized parameters for the SLM process with the different optimization algorithms. From this Table, we can conclude that all the algorithms provide similar fitness values and that the optimized parameters are also very similar. However, the PSO produces results much faster than the other two algorithms. Therefore, using a PSO optimization algorithm with the DNN model to obtain the optimal parameters is highly efficient and less computationally expensive than the

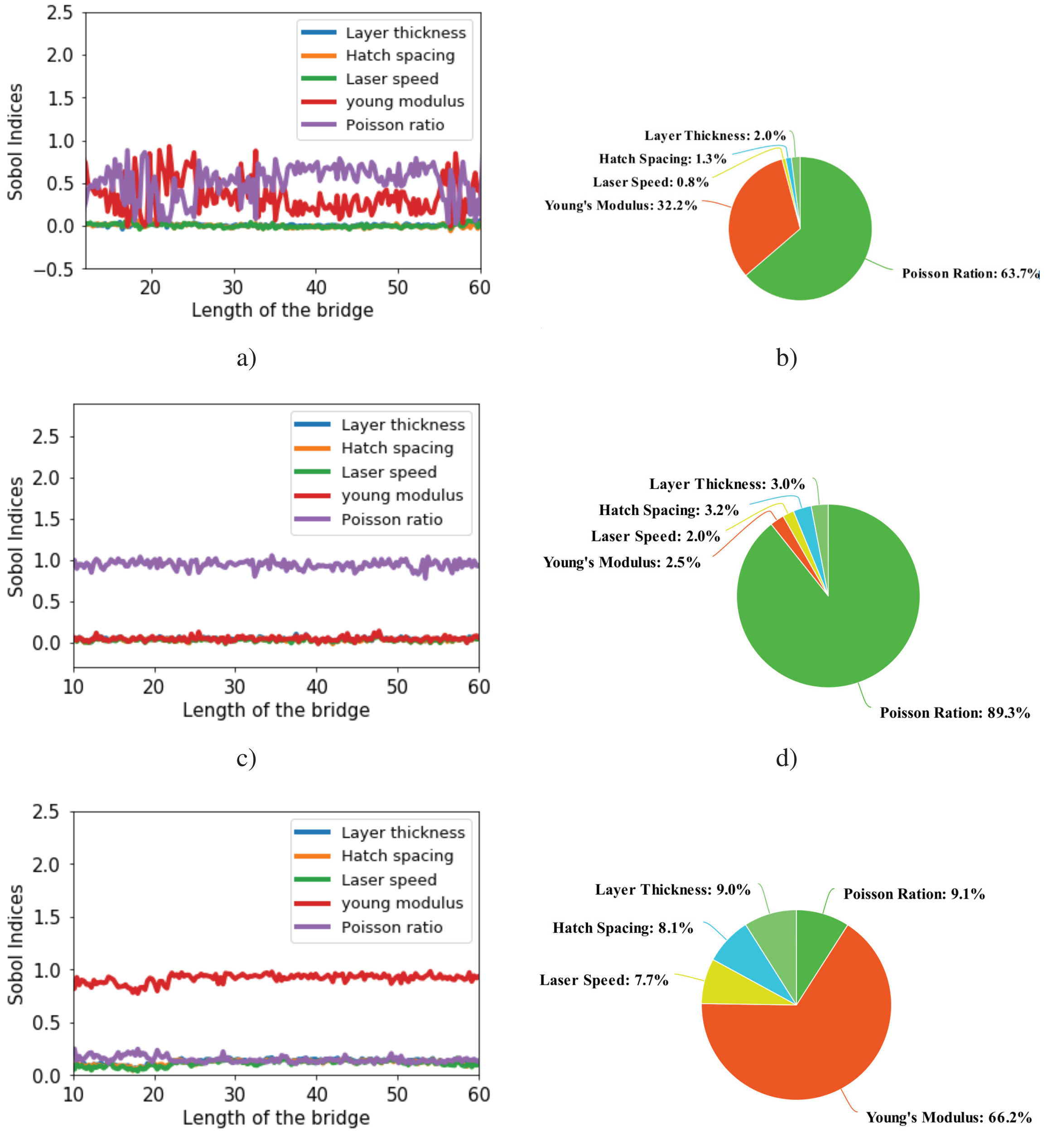

a) b)

c) d)

e) f)

Figure 3.18 Variation in sensitivity indices along the length of the bridge (x-direction) at z = 9.536 are pre-sented in figures (a), (c) and (e) for the x, y, and z-directional strains, respectively. Where-as the figures (b) (d) and (f) represents the importance of each parameter in a percentile form for x, y and z directional strains respectively other options.

In Figure 3.19 we present the SLM outputs for the optimized parameters obtained from all three optimization algorithms. We used Ansys additive simulation for each set of optimized parameters obtained from all three algorithms and plotted the normal strains along with the experimental results. From Figure 3.19a,b, we can conclude that the results are similar and very close to the experimental results. Figure 3.20 compares the optimized output results obtained from the simulation and from the DNN model. The L2 error norm between simulation and a surrogate model is 0.0965 and 0.2264 for x and y directional strains, respectively. The figure proves the efficiency of the DNN model and the optimized results, which lie in the 95% confidence interval.

Table 3.6 Optimized parameters

Parameters	**Layer Thickness**	**hatch spacing**	**Laser Speed**	**n**	**m**	**Fitness Value**	**Time Elapsed(sec)**
GA	0.0170	0.1033	760.1680	1.15	1.15	2.2962×10^{-5}	14,019.56
PSO	0.0170	0.09713	735.3737	1.15	1.1379	2.3043×10^{-5}	75.00
DE	0.0170	0.1032	757.5025	1.15	1.15	2.229402×10^{-5}	13,108.4366

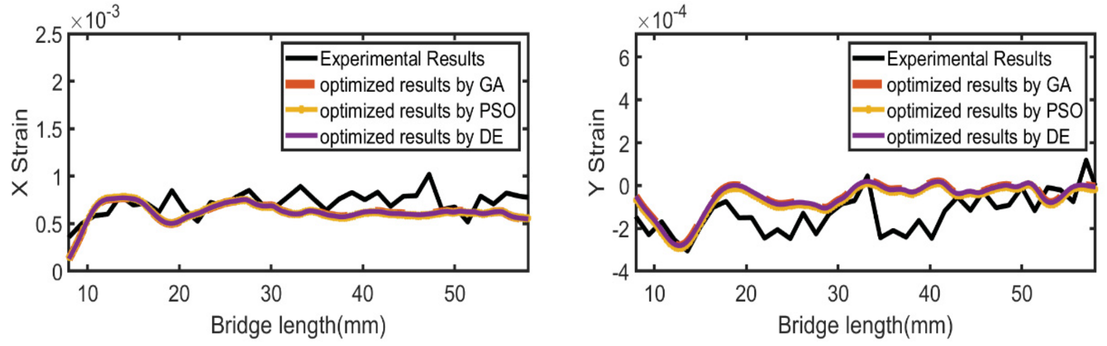

Figure 3.19 Comparison of simulation results from DNN model using the optimized parameters obtained by GA, PSO, and DE

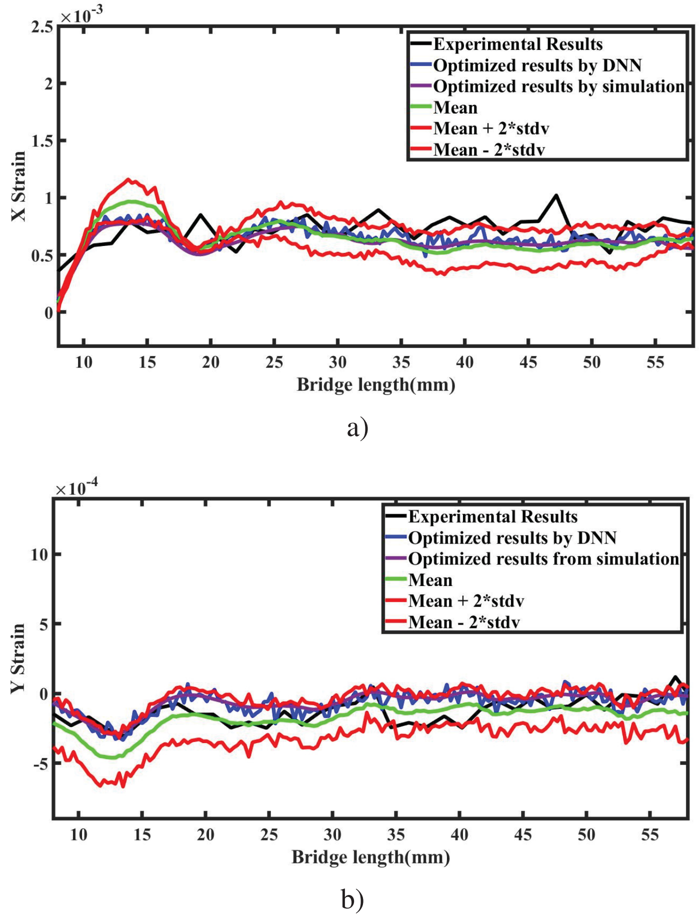

Figure 3.20 Confidence intervals of simulation results from DNN model and for the optimized parameters obtained from PSO. (a,b) represent the x and y strains, respectively

3.4 Conclusions

In this paper, we presented a framework to analyze and optimize the SLM process other than the more widely-used experimental and numerical techniques. We used machine learning (ML) methods with the SLM numerical model to study the sensitivi-ty and uncertainty during the additive process. Neural networks and polynomial chaos expansions were the primary machine learning methods that we considered. The da-taset of full-order numerical solutions was performed using ANSYS additive software and the results were validated using publicly available experimental results. The 3D thermo-mechanical finite element model was used to solve a set of 360 samples created using the Sobol sampling technique. The outputs from the 360 samples were then used to train and test the surrogate models. We found that the deep neural network model was faster than the PCE model, so we adopted the DNN model for the rest of the anal-yses. Once the DNN model was trained, it was combined with the Monte Carlo tech-nique to find the number of simulations needed to perform the sensitivity and uncer-tainty analyses in the SLM process. The standard deviation convergence plots for each sample set helped us to conclude that 6000 samples are sufficient to perform the study. The sensitivity analysis revealed that the Young's modulus and Poisson coefficient are the most critical parameters during the process, while the layer thickness, laser speed, and hatch spacing are less important. However, the machine parameters still hold sig-nificant importance (5% to 10%). As all the parameters hold significant importance in the SLM process, we considered all five parameters for the optimization analysis. The surrogate DNN model was utilized to optimize with three different algorithms: GA, PSO, and DE. The results were compared, and all three algorithms were found to be equally good at calculating the optimal solution; however, PSO took the least time. The combination of DNN and PSO for optimization provided good results and incurred significantly less computation cost. In the future, as an extension of this study, we will work with the physically informed machine learning models to improve results.

CHAPTER 4

DATA-DRIVEN NON-INTRUSIVE REDUCED ORDER MODELLING OF SELECTIVE LASER MELTING ADDITIVE MANUFACTURING PROCESS USING PROPER ORTHOGONAL DECOMPOSITION AND CONVOLUTIONAL AUTOENCODER

Shubham Chaudhry[1] , Azzedine Abdedou[1] , Azzeddine Soulaimani[1]

[1] Département de génie mécanique, École de Technologie Supérieure,
1100 Notre-Dame Ouest, Montréal, Québec, Canada H3C 1K3

Paper submitted in *Computer and Mathermatics with application*, March 2023

Abstract

Two data-driven, non-intrusive, reduced-order models (ROMs): a convolutional autoencoder-multilayer perceptron (CAE-MLP) and a combined proper orthogonal decomposition-artificial neural network (POD-ANN) are proposed and compared for additive manufacturing (AM) processes. The CAE-MLP uses a 1D convolutional autoencoder for spatial dimension reduction of a high-fidelity snapshot matrix constructed from high-fidelity numerical simulations. The reduced latent space after compression is projected to the input variables using a multilayer perceptron (MLP) regression model. The POD-ANN uses proper orthogonal decomposition-based, reduced-order modeling with the artificial neural network to construct a surrogate model between the snapshot matrix and the input parameters. The accuracy and efficiency of both models are compared based on the thermo-mechanical analysis of an AM-built part . A comparison between the statistical moments from the high-fidelity simulations results and the ROMs predictions reveals a good correlation. Additionally, the predictions are compared with the experimental results at different locations. While both models show good comparison with the experimental results, the CAE-MLP predictions have proven to be better performing than those of the POD-ANN.

Keyword

Reduced-order model, Convolution autoencoder, Additive manufacturing, Deep learning.

4.1 Introduction

Laser powder bed fusion (L-PBF) is an Additive manufacturing (AM) technology, in which a 3D part is manufactured by successfully fusing material powder layers with a high-energy beam laser. L-PBF can be divided into two types: Electron beam melting (EBM), wherein a high-energy electron beam melts powder layers, and Selective laser melting (SLM), which uses a high-power photon to bond powder layers together. This technology can help build complex and robust geometries with less material wastage and thereby reduce part manufacturing costs. However, many challenges, including part distortion, built part accuracy, and the premature termination of a built part, still require further investigation. As part of the current study, the SLM process is considered with the evolution of temperature, and the strain in the built part is analysed to understand the building process better.

The SLM process undergoes a high-temperature gradient during the melting process. The melt pool temperature can reach several thousand degrees celsius, whereas the temperature surrounding the solidified regions remains close to that of the environment or the preheat temperature. The cyclic cooling and heating of the powder material leads to residual stresses, resulting in an incompatible built part. The high-temperature gradient is directly attached to the moving high-power laser, and so a highly nonlinear and very fine mesh around the melt pool is required to obtain an accurate numerical model.

Similarly, the process involves several length and time scales, which makes the numerical simulation even more complex. For example, the steep increase in the melt pool's temperature takes a few seconds, whereas the layer-to-layer building method takes several hours or days to finish; the cooling of the built part may take even more time. Other difficulties that must be considered in the SLM simulation are the phase transformations and the latent heat associated with the phase change, which transforms the powder into a liquid and then a solid phase. These challenges in the building process make the SLM thermal analysis complex and computationally expensive. The SLM community is in dire need of an advanced numerical simulation or a new approach that can significantly reduce the computation cost.

A high-fidelity, data-driven machine learning model can provide an alternative approach to studying the SLM process (Meng *et al.*, 2020) (Wang *et al.*, 2020). Ravichander *et al.* (2021) presented a neural network model for the SLM output predictions, where the model was trained over experimental data points and then applied to find a new dataset. Chaudhry & Soulaïmani (2022) presented a framework with machine learning (ML) to construct a surrogate model for SLM and used it to optimize the built part. Similarly, (Francis & Bian, 2019) (Mozaffar *et al.*, 2018) (Rong-Ji *et al.*, 2009) (Zhang, Liu & Shin, 2019a) (Meng & Zhang, 2020) also provided ML models for the additive manufacturing process. However, the complexity is compounded when the dimensionality of a data set expands. For example, in (Chaudhry & Soulaïmani, 2022), the dimension of the data matrix used for training the deep neural network (DNN) model was 360*287. If the dimension of the matrix is increased to 360*97650, then the DNN would not be a likely approach with which to construct a ML model, because the trainable parameters would reach a million or a billion depending upon the depth and the size of the neural network. Recently, reduced-order modelling (ROM) has gained popularity in the computational community as a means to reduce high computation costs without compromising accuracy, especially where dimensionality is a big challenge. ROM gives a faster surrogate model for computationally expensive simulations. Such speed is especially useful for optimizations of real-time tracking tasks that require significantly large model iterations or rapid online predictions in industrial applications and in fundamental science.

One of the more popular ROM methods to convert a high dimensional problem to a low-dimensional problem is proper orthogonal decomposition (POD). POD was initially presented by (Pearson, 1901) in 1901, and has since been developed and improved to provide an effective and efficient technique for ROM analysis for several applications (Xiao *et al.*, 2017). Recent developments have provided many non-intrusive methods to calculate the coefficients of linear POD approximations with the help of data-driven approaches without compromising the governing equations (Chatterjee, 2000). This method consists of a stochastic framework, such as POD with polynomial chaos expansion (POD-PCA) or POD coupled with an artificial neural network (POD-ANN), which constructs a regression framework with the reduced-order modelling between the input parameters and the coefficients of POD basis (El Moçayd *et al.*, 2020) (Abdedou & Soulaïmani, 2021) (Jacquier *et al.*, 2021) (Sun & Choi, 2021) (Abdedou & Soulaimani, 2019).

(Zhao *et al.*, 2021) POD for thermal study of the electron beam melting system. Their investigation used the ABAQUS model and POD to study the temperature distribution of a moving energy source in the EBM process. Likewise, (Gaonkar & Kulkarni, 2015) (Fic *et al.*, 2005) (Białecki *et al.*, 2005) developed POD-based ROM methods to solve the linear and non-linear transit heat transfer problem and presented a good correlation of the standard FEM code and POD-FEM results. The central core of POD application is the building of a high-fidelity snapshot matrix to obtain a small set of eigen modes and the coefficients of the linear basis constructed with these modes. (Liu & Liu, 2023) performed a ROM with POD and generated a map for input parameters and the POD bases with the help of the regression tree method. The constructed map was later used to project the outcomes for a new set of input variables. In two different studies (Abdedou & Soulaïmani, 2021)(Jacquier *et al.*, 2021) POD modes are combined with ML models, including artificial neural networks (ANNs). The POD and ML algorithms have proven effective and productive in analysing large data sets and processes. In our study, we use a POD-ANN method that constructs a regression surrogate model for the ROM to learn and predict the strains in an SLM-built part.

POD has attracted much attention recently, it is a linear procedure. Although linearity is part of the POD method's strength it is also its biggest limitation, as the POD lacks the accuracy to capture complex dynamic systems Abdedou & Soulaimani (2023). To address these limitations, non-linear manifolds have been considered as an alternative for dimensional reduction problems, and some of these approaches are based on deep learning technology (Zhu, Shi, Song, Tan & Tao, 2020a) (Zhu, Shi, Song, Tao & Tan, 2020b). Autoencoder is one such method, consisting of two segments, an encoder and a decoder. (Tan *et al.*, 2019) presented a convolutional neural network (CNN)-based autoencoder (CAE) model to detect anomalies in an AM-built part. CNN autoencoders include different operations like convolution, multilayer perceptron, upscaling and pooling (He *et al.*, 2021) (Gonzalez & Balajewicz, 2018), thereby helping to reduce the number of training parameters required. In similar studies (Shi *et al.*, 2022) (Siddalingappa & Kanagaraj, 2021) (Tang *et al.*, 2021), a CAE is combined with Long Short-Term Memory (LSTM) networks to build a framework for surrogate modelling projections, especially for time dependent predictions in AM-built parts.

The present study proposes a framework of non-intrusive reduced-order models for the parametric analysis of the SLM building process. This data-driven framework uses POD and convolution autoencoders (CAE) in two different approaches to decrease the high-fidelity matrix dimension obtained by finite element numerical solutions. The solution matrices are the normal directional strains calculated using Workbench additive software(ANSYS). It should be noted that the complexities of these models are not the same, and the goal for this comparison is to evaluate how the model designs and the training procedures affect the learned latent modes and the quality of the reconstructions and predictions. In the first approach, the POD bases of the strain matrices are calculated and then a surface is created between the input variables and the POD bases using an artificial neural network. The constructed surrogate model is used to calculate the strains over a new data set of input parameters. In the other approach, the dimensionality of the snapshot matrix is reduced using the CAE method, where the spatial dimension is reduced by encoding the data to create a latent space. The generated latent space is related to the input variables with a multilayer perceptron network (MLP). The decoder part of the 1D autoencoder maps the latent space to the previous dimension. The trained MLP and 1D decoder help to reconstruct the original spatial dimension of the SLM built part from the latent space for the new set of input process parameters. The proposed framework is applied for the stochastic treatment of the benchmark case of an SLM-built part, AMB2018-1, produced by the National Institute of Standards and Technology (NIST) (Phan *et al.*, 2019). The study provides new features for the reduced-order modelling of complex physical problems.

The chapter is divided into the following sections. Section 4.2 presents a short description of the mathematical backgrounds of the POD and the CAE. Section 4.3 evaluates the performance of the proposed framework by comparing the numerical results from the benchmark case. Concluding remarks and recommendations are presented in Section 4.4.

4.2 Mathematical modelling

4.2.1 Proper orthogonal decomposition(POD)

POD initially originated from the turbulence flow field with the concept of forming deterministic functions by decomposing the random vector fields of turbulence fluid motion and representing fluctuating kinetic energy in the flow (Lumley, 1967) (Weiss, 2019).The expectation was that this finite number of deterministic functions, also known as POD modes, would be able to describe the flow structure. This approach has been widely adopted in other fields. The POD compresses two essential properties: optimality and orthogonality. Optimality ensures that the POD provides the most efficient decomposition, which means the leading modes possess the highest possible energy compared to all the linear decompositions during projection over the subspace. Orthogonality indicates that the time series of the coefficients are linearly uncorrelated, an important property for making reduced-order models.

Let us suppose $Y = [y_1, y_2, ...y_n]$ is a real-valued $m \times n$ matrix whose rank is $d \leq min(m, n)$ with columns $y_j \in R^m, 1 \leq j \leq n$. POD is combined with singular value decomposition (SVD) to obtain the reduced order model and a low-rank approximation that is easy to compute. The SVD assures that there are real numbers $\sigma_1 \geq \sigma_2 \geq \ldots\ldots \geq \sigma_d > 0$ and orthogonal matrices $\Psi \in R^{m\times m}$, with columns $\{\Psi_i\}_{i=1}^{m}$, and $\Phi \in R^{n\times n}$, with columns $\{\phi_j\}_{j=1}^{n}$, such that

$$\Psi^T Y \Phi = \begin{pmatrix} D & 0 \\ 0 & 0 \end{pmatrix} \tag{4.1}$$

Here, $D = diag((\sigma_1, \sigma_(2) \ldots \sigma_d) \in R^{d\times d}$. The zero blocks in equation 4.1 have the appropriate dimensions, and T represents the matrix transpose. In addition, $\{\Psi_i\}_{i=1}^{d}$ and $\{\phi_i\}_{j=1}^{d}$ satisfy the properties

$$Y\phi_i = \sigma_i \psi_i \; and \; Y^T \psi = \sigma_i \phi \tag{4.2}$$

where $i = 1, 2, \ldots.d$, and which these are eigenvector of YY^T and $Y^T Y$, respectively, with the eigenvalues $\lambda_i = \sigma_i^2 > 0, i = 1, 2 \ldots .d$. Also, $\{\psi_i\}_{i=d+1}^{m}$ and $\{\phi_i\}_{i=d+1}^{m}$ are eigenvectors with the eigenvalue 0 of YY^T and $Y^T Y$ (if $d < m$ and $d < n$). From equation 4.1 we can write

$$Y = \Psi \begin{pmatrix} D & 0 \\ 0 & 0 \end{pmatrix} \Phi^T \tag{4.3}$$

For a finite number of initial L modes, the truncation criteria are imposed on the singular values as shown below:

$$\frac{\sum_{l=L+1}^{r} \sigma_l^2}{\sum_{l=1}^{r} \sigma_l^2} \leq \delta \tag{4.4}$$

where δ is a small parameter. So, every mode vector V_j may be calculated from the jth column of ϕ as

$$v_j = \frac{1}{\sigma_i} Y \Phi_j \tag{4.5}$$

Thus, the POD mode matrix can be constructed as below

$$V = [V_1|......|V_j|....|v_L] \in R^{m \times L} \tag{4.6}$$

Once the POD modes are obtained, they are then used to calculate the projection coefficients ν for the snapshot matrix as shown:

$$\nu = V^T Y \tag{4.7}$$

Similarly, the POD bases and the projection coefficients can be used to find the approximation matrix of Y:

$$Y^* = V V^T Y = V \nu \tag{4.8}$$

The quality of the compression/expansion process can be captured by the relative projection error shown in the equation:

$$RE_{POD} = \sum_{j=1}^{n} \frac{||y_j - y_j^*||_2}{||Y_j||_2} \tag{4.9}$$

where j represents the jth column of the targeted matrix and $||.||_2$ is the L^2- norm.

4.2.2 Proper orthogonal decomposition and artificial neural network(POD-ANN)

A pictorial representation of the POD-ANN method is shown in Fig 4.1. In the first step, the POD algorithm is used to find the POD modes from the snapshot matrix. These modes are then used to obtain the projection coefficients ν for the snapshot matrix, which are a low-dimensional representation of the original data. Next, an artificial neural network (ANN) is trained to create a mapping between the input variables and the projection coefficients ν. The POD-ANN framework is divided into two parts; the training part is called an offline phase, during which the ANN model is trained and where the input parameters are the physical algorithm variables α and the outputs are the projection coefficients ν. Eighty percent of the data is used to train the model and 20% is used for testing. The other part of the POD-ANN framework is the online phase, where the trained ANN model is used to predict the new projection coefficients ν^* for a new set of physical parameters α^*. The coefficients calculated on the POD basis are then expanded to the original dimension using the format shown in algorithm 4.1.

Algorithm 4.1 Flowchart of the POD-ANN method

```
Function POD-ANN
V ← POD(Y)
$\nu \leftarrow V^T$ Y
$\nu \leftarrow$ ANN($\alpha$)(Training of ANN model with $\alpha$ inputs and $\nu$ outputs)
$\nu^* \leftarrow$ ANN($\alpha^*$)(Predicition)
$Y^* \leftarrow$ V$\nu^*$
Return $Y^*$
```

4.2.3 Convolution autoencoder

An autoencoder is a type of deep neural network that is useful for unsupervised feature extraction. The architecture has the potential for modal decomposition because it provides a framework that includes non-linearity in the mapping by using a nonlinear activation function. However, the modal decomposition of an input field that contains multiscale coherent features is challenging for a neural network autoencoder. This challenge can be overcome by using convolution layers

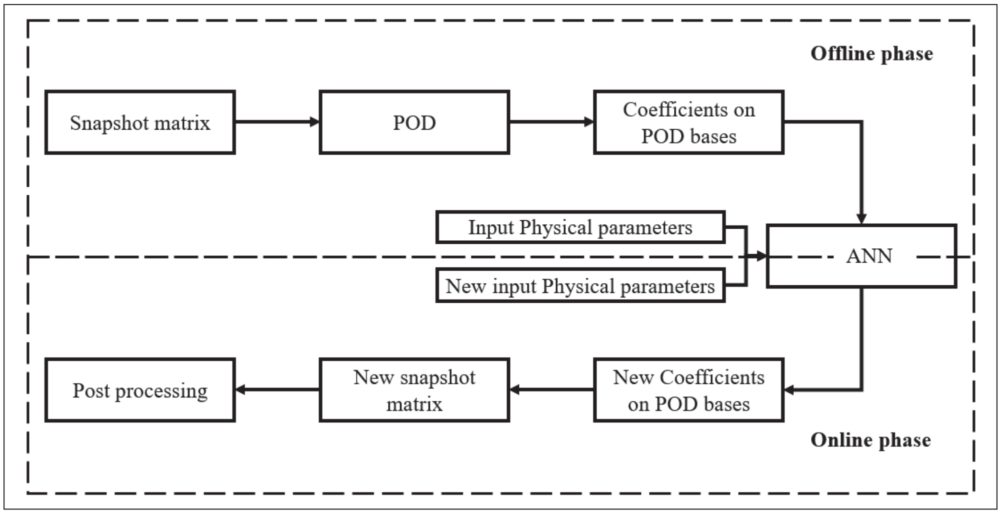

Figure 4.1 Sketch of the POD-ANN process

in the autoencoder to process the input information.

Convolutional autoencoders (CAEs) have gained popularity in image recognition as powerful techniques for non-linear reduced-order modelling. The convolution layers provide an alternative approach to the limitations that a classical autoencoder based on deep neural networks (i.e. fully connected layers) faces for high dimensional inputs (Gonzalez & Balajewicz, 2018). A CAE has two parts, an encoder and a decoder. The encoder part reduces the input matrix's dimension and maps it to a latent space using a composition of convolutions, pooling, and densely connected layers. The decoder uses convolutions, upscaling, and dense layers to map the latent space to the original dimension of the input matrix. The architecture of a CAE is presented in figure 4.2, and a similar CAE approach is applied here for the encoding and decoding of the spatial dimension of the input snapshot matrix.

A convolution layer is a feature map representation in which a selected part of a previous layer is fully connected with each unit of the next layer with the help of an activation function and a kernel. This connection permits the calculation of the most significant features from the input matrix with the help of the kernel. A mathematical representation of a 1D convolution layer is given by (Maulik *et al.*, 2021):

$$h_i^l = \sigma(H^{l-1} * f_i^l + b_i^l) \tag{4.10}$$

in which the $*$ denotes the 1D convolution operator, $h_i^l \in R^{D_l \times 1}$ represents the i^{th} feature of the l^{th}, σ is the nonlinear activation function, $H^{l-1} = [h_1^{l-1}, h_2^{l-1} \dots .h_{N_{f_{l-1}}}^{l-1}]$ represents the convolution layer $l - 1$, b_i^l gives bias value with $i \in N_{f_l}$, f_i^l represents kernel for layer l and $l \in (1, n)$. The depth of the convolution layer is represented by the total number of layers. After each layer, the pooling layers are inserted to decrease the dimension of the features by an amount that is defined by the kernel size of the pooling layer.

As presented in the previous section, the snapshot matrix consists of a set of n high-fidelity solutions obtained from the numerical simulation $Y(\alpha_s) \in R^m, s = 1, \dots .n$. In this solver, α_s is the s^{th} value of the random variable α in its data sample with size n, which follows a probability density function $\varphi(\alpha)$. All these vectors' solutions are combined and form a global snapshot matrix:

$$Y = [y_1 ... y_s ... y_n] \in R^{m \times n} \tag{4.11}$$

Where m is the total number of computational nodes in the spatial domain. The global snapshot matrix created above is divided into two sets, one with 80% and the other with 20% of the data for training and validation, respectively.

The CAE framework is divided into three parts: 1) spatial compression, 2) a regression-based multilayer perceptron (MLP), and 3) online surrogate predictions. The spatial compression provides the dimension reduction of the input data matrix from n to L along the spatial dimension

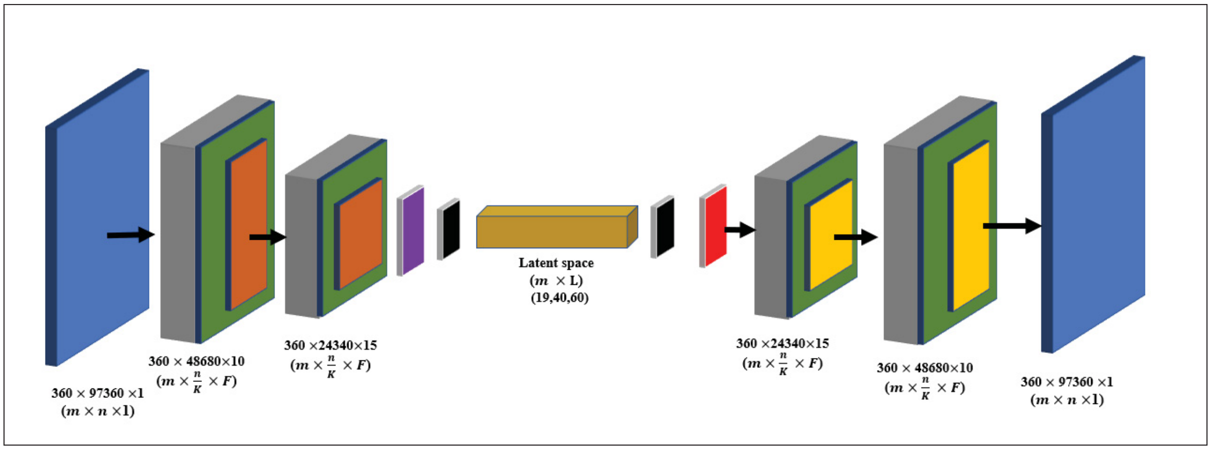

Figure 4.2 Pictorial representation of a1D convolution autoencoder architecture, where K and F represent the maxpool kernel and convolution filters, respectively. The colour coding for each layer is: 1D convo layer, Prelu activation function, max pooling, flatten, dense , reshape upscaling

where L represents the latent space dimension. The snapshot matrix Y is reshaped using the space encoder $F_{x_{enc}}$ part of the CAE along the spatial dimension, as given:

$$V_{xL} = F_{x_{enc}}(Y) \in R^{m \times L} \tag{4.12}$$

where V_{x_L} represents the snapshot matrix with reduced dimension. The detailed structures for every autoencoder in the test set and the benchmark problem are given in appendices I-1 I-2 I-4 I-5. Once the latent space is constructed, the next level of the CAE framework is applied: the implementation of MLP in the latent space. The MLP maps the latent space V_{x_L} to the input variables α. The MLP model consists of multiple fully connected neuron layers. The detailed structures of the MLP applied for each case are given in appendices I-3 and I-6. The compression of the spatial dimension and the MLP are classified as an offline phase of the CAE as shown in fig 4.3. It must be noted that the framework presented here is built using the open source package TensorFlow (Abadi *et al.*, 2016) with the Adam optimizer and its default parameters. The input snapshot parameters are normalized to accelerate the optimization and the convergence of the training process, and the coefficients of the snapshot matrix are normalized between [-0.5 0.5], as:

$$\frac{Y_{si} - min(Y_s)}{max(Y_s) - min(Y_s)} \tag{4.13}$$

where $s = 1, ...n, i = 1.....m$, u_{si} is the normalized outptu for the s^{th} input parameter and the i^{th} mesh node. The final step is the online surrogate prediction of a new data set.

A new set of input variables is constructed using the Latin hypercube sampling (LHS) algorithm (Saliby & Pacheco, 2002). For each value of the new data set, a spatial latent vector ($V^*_{x_L}$) is generated using the trained MLP regression model. The predicted latent space is then transformed back to the original dimension using the spatial decoder function ($F_{x_{dec}}$), $Y^* = F_{x_{dec}}(V^*_{x_L})$. The flowchart of this framework is presented in Fig4.3 and algorithm 4.2.

Algorithm 4.2 Flowchart of the POD-ANN method

```
Function POD-ANN
$V_{xL} \leftarrow F_{x_{enc}}(Y)$ (Encoding snapshot matrix to latent space)
$V_{xL} \leftarrow$ MLP($\alpha$) (Training of MLP model with $\alpha$ inputs and $V_{xL}$ outputs)
$V^*_{xL} \leftarrow$ MLP($\alpha^*$)(Prediction with new input parameters)
$Y^* \leftarrow F_{x_{dec}}(V^*_{xL})$(Decoding latent space to orignal diamension)
Return $Y^*$
```

4.3 Results and Discussion

This section is devoted to the assessment of the POD-ANN and the autoencoder models on a 2D-dimensional heat transfer test case and a 3D additive manufacturing test case. The comparison of the results obtained from the proposed models with the experimental results shows the efficiency and accuracy of the proposed reduced- order models.

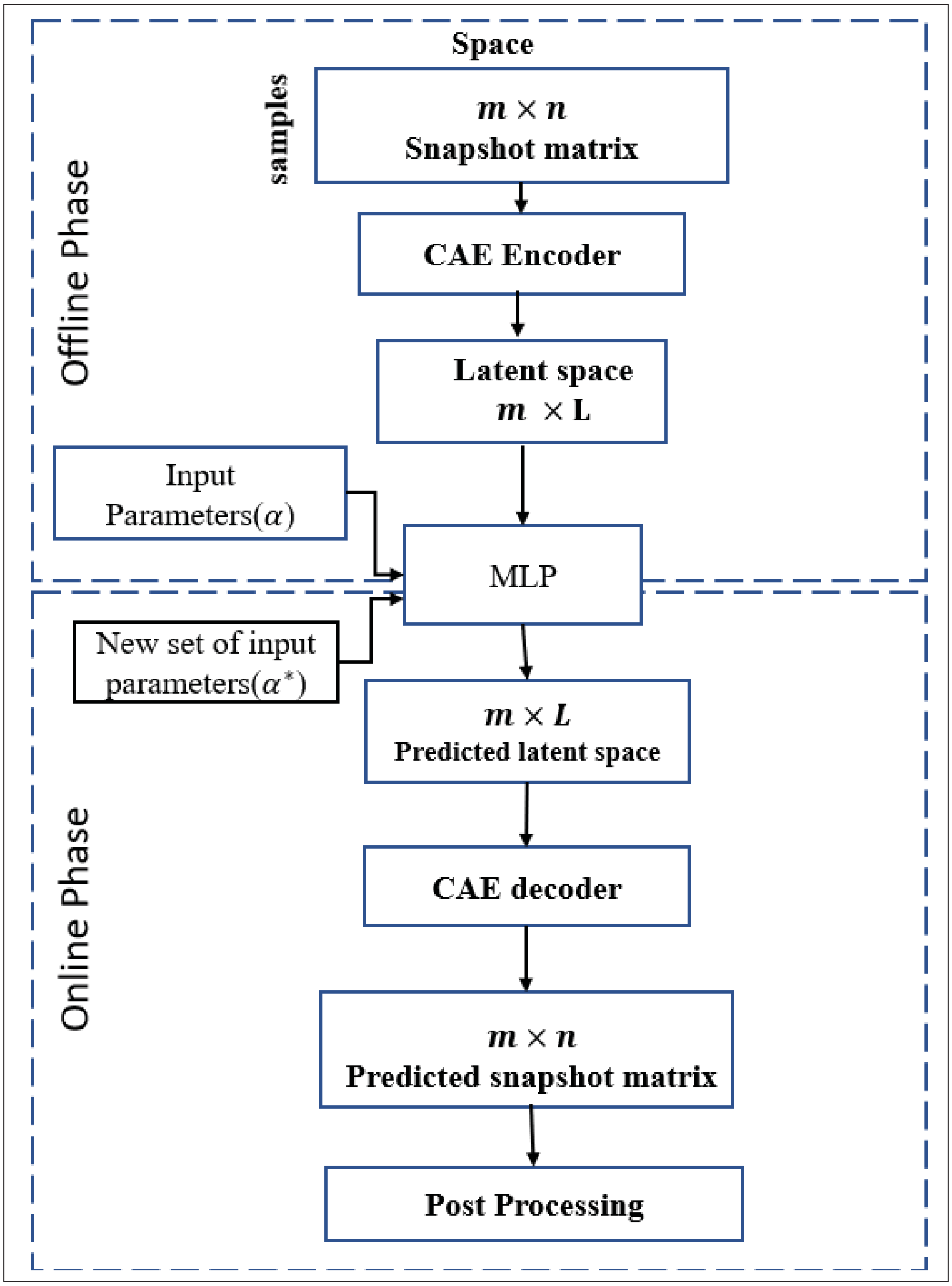

Figure 4.3 Flow chart of the CAE with its online and offline phases

4.3.1 2D heat transfer test case

This simple test case considers the heat transfer over a plate of thickness e in a steady state. The purpose is to validate the implementation of the different algorithms. The governing equation and the boundary conditions are described by the linear heat equation:

$$div(\vec{q}) = \frac{2h}{e}(T_{ex} - T) \tag{4.14}$$

where, $div(\vec{q})$ is the conduction flux given by Fourier's law $div(\vec{q}) = -K\nabla T$ (K is the conductivity, h is the coefficient of convection and $T_{ex} = 100°C$ represents the given temperature at one side. The boundary condition at the edges is $\vec{q}.\vec{n} = h(T - T_{ex})$. The temperature is 22∘C at the base ($x = 0$). In this test case, the coefficients of convection and the conductivity are constant and are considered the input parameters, and the temperature over the whole domain is considered the output. A total of 300 samples were generated for the input parameters using the LHS algorithm, with the samples collected uniformly in the intervals [61, 51] and [57.5, 42.5] for K and h , respectively. For each input set, the heat equation was solved using an in-house code based on the finite element method. The mesh is constituted of quadrilateral elements with a total of 289 nodes as shown in figure 4, and the output snapshot matrix was used to train the POD-ANN and CAE-MLP models. The data set of 300 samples was divided into 80% and 20% for training and testing, respectively. Once the training was completed, the predictions from both models with a new set of input parameters were compared with the original snapshot matrix. A set of 5000 samples was generated, using the LHS method, and the surrogate models (POD-ANN and CAE) were run to obtain new predictions. A statistical analysis of the outputs was then performed.

The POD-ANN model consists of 3 hidden layers with 50 neurons in each layer. The model found that 3 POD modes were sufficient to predict the accurate outputs of the heat transfer problem. The CAE-MLP model transforms the spatial dimension from 288 to the reduced-order latent space dimension of 5. More details on the encoder and decoder structure are presented in table

I-1 I-2. This process produces a total of 140,587 trainable parameters. The constructed spatial latent space is then mapped to the input variables using a multilayer perceptron with 34,053 trainable parameters; the detailed structure is presented in table I-3. The MLP and the CAE are trained for 5000 and 500 epochs, respectively, and the loss convergence graphs are shown in fig 4.5.

The comparison of the CAE-MLP and the POD-ANN with the snapshot matrix is performed using the standard deviation (std) and the mean of the predicted temperature distribution of the whole domain. The outputs are compared in Fig 4.6; the graph shows a good comparison between the temperature profiles predicted from the POD-ANN and the CAE-MLP with the original snapshot matrix. The relative L2 error norm between the mean of the predicted temperature profile for the 300-snapshot matrix and each of the 5000 realizations of the POD-ANN and the CAE-MLP are 2.88e-07 and 5.76e-08, respectively. It is essential to mention that the 5000 realizations are the new input parameters and not those used in the training phase. Fig 4.6a shows the mean temperature variation between 100 and 80$\circ$C over the whole domain, while fig 4.6b indicates the variation of the temperature profile for each node in the set for a given number of input parameters. Both models required similar times to train and predict the outputs; however, the relative L2 error norm for the CAE-MLP is less than that of the POD-ANN. This difference shows that the CAE-MLP predictions are better than those of the POD-ANN. Table4.1 presents more details about each model.

Table 4.1 Comparison between the POD-ANN and the CAE-MLP

	POD mode Latent space	**Training time(sec)**	**Prediction Time(sec)**	**Relative L2 error mean**	**Relative L2 error std**
POD-ANN	3	422.37	4.15	2.8810^{-07}	9.0210^{-05}
CAE-MLP	5	444.743	5.89	2.8810^{-07}	3.0510^{-05}

4.3.2 Additive manufacturing benchmark test

The National Institute of Standards and Technology (NIST) released in 2018 a number of standard benchmark tests for different AM processes to support the community in verifying their

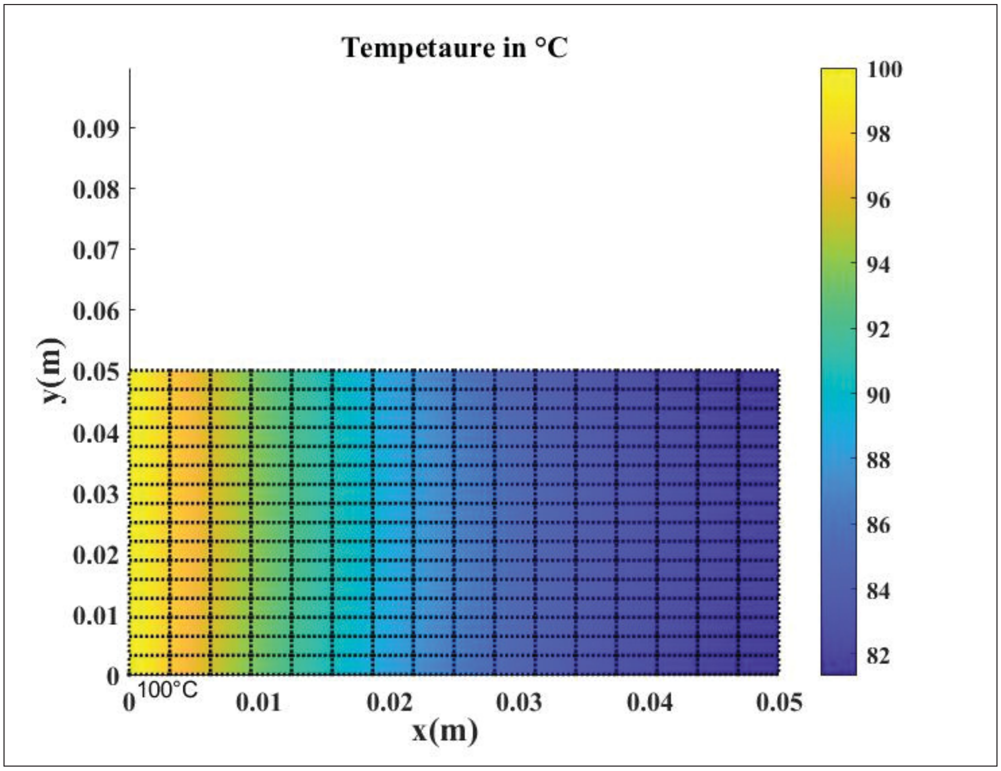

Figure 4.4 Pictorial representation of the mesh structure and temperature distribution throughout the plate

numerical simulations. The AMB2018-01 test is one such case, designed for the selective laser melting process with the material IN625. AMB2018-01 is a bridge structure of 75 ×5 ×12.5 (mm × mm × mm) dimension built over an 81×12.7×11(mm × mm ×mm) substrate as shown in Figure 4.7a and 4.7b. The case study aimed to provide reliable data for the residual stresses, strains and deflections in the built part. The residual stresses and strains were calculated using the neutron diffraction and x-ray methods, whereas the defection was measured after partially cutting the bridge from the base plate. More details on the experimental processor and the geometry can be found on the NIST website (torey.liepa@nist.gov).

The additive manufacturing numerical simulation is constructed using the workbench additive software. The validation of the workbench model was conducted in a previous publication (Chaudhry & Soulaïmani, 2022), for details on the workbench additive model readers are referred

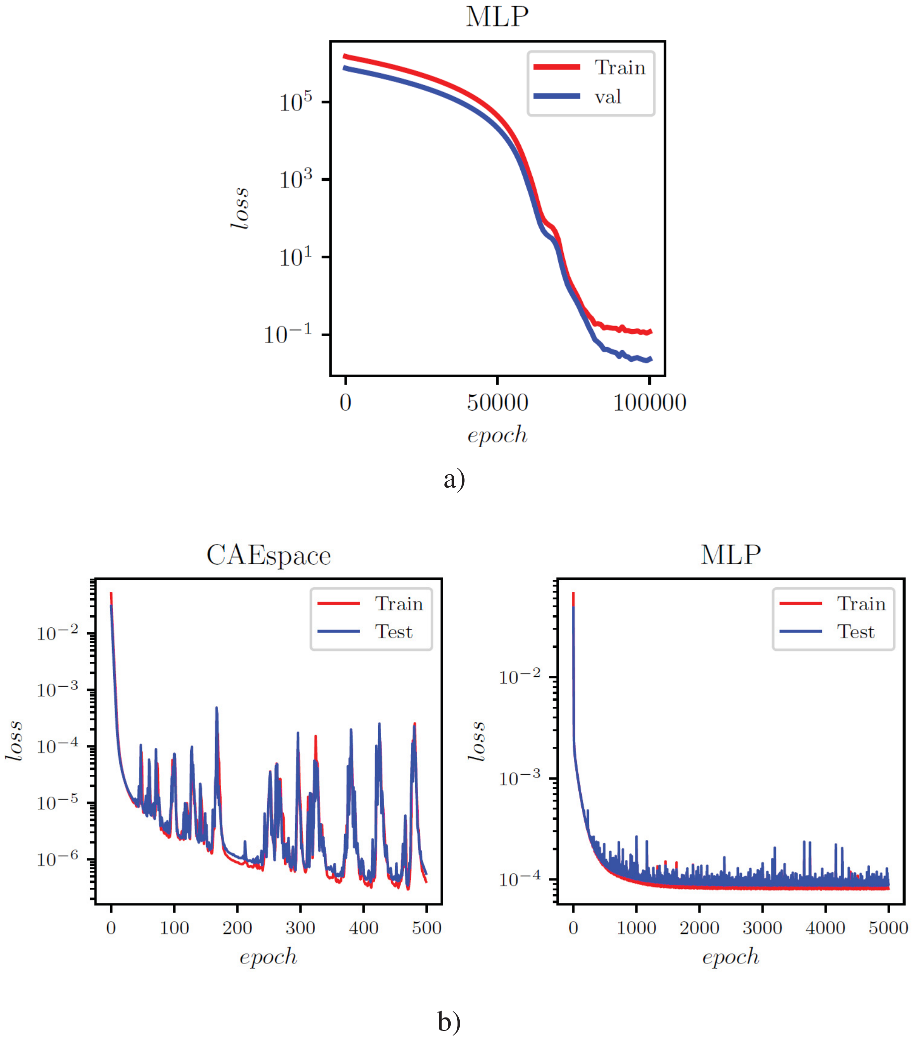

a)

b)

Figure 4.5 Loss function evolution with epochs for the POD-ANN (a), CAE (b) and the MLP (c) networks

to (ANSYS). The simulation took 1 hour on 32 CPUs with an Intel E5-2683 v4 processor. The layer thickness, hatch spacing, laser speed, Poisson's coefficient and Young's modulus were considered the random input parameters, whereas the strain in the whole domain was considered as the output variable. The output strains were calculated over 97360 nodes in the entire three-dimensional mesh, as shown in figure 4.7c. To eliminate edge or boundary error, the nodes near the boundary were not considered. This simplification reduces the number of nodes, which helps to minimize the computation cost. The five input parameters were selected from

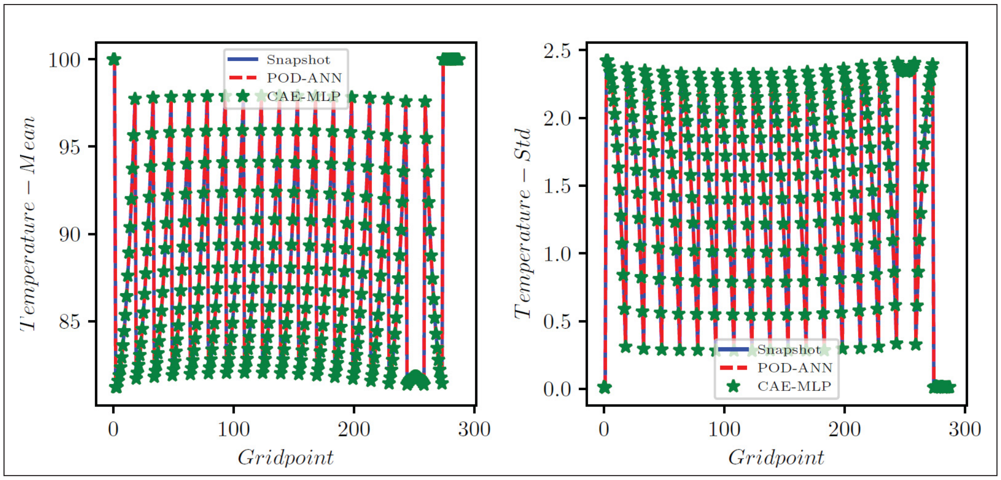

Figure 4.6 Loss function evolution with epochs for the POD-ANN (a), CAE (b) and the MLP (c) networks

within the bounds listed in table 4.7a to create a data space of 360 samples randomly selected by the LHS sampling method. The Young's modulus and the Poisson ratio were multiplied with scaling variables c_1 and c_2 , respectively, which helps in changing the values of these inputs. Also, the normal directional strains over the 97360 nodes were calculated for each input sample and the solutions obtained from each input sample were combined to construct a high-fidelity snapshot matrix which was later used to train the POD-ANN and CAE-MLP models.

Table 4.2 Lower and upper bound for the input variables

Input Variables	**Lower Bound**	**Upper Bound**
laser speed	680 mm/s	920 mm/s
layer thickness	0.085 mm	0.115
hatch spacing	0.017 mm	0.023
CY	0.085 mm	0.115
Cν	0.085 mm	0.115

A total of three snapshot matrices of dimension 360*97360 were generated for the x, y, and z normal strains. For each matrix, the POD-ANN and CAE-MLP models were trained separately. The performance of both models was evaluated by comparing the statistical moments with the original snapshot matrix. Figure 4.8 shows the training and testing of the POD-ANN models for all three normal stains, and figure 4.9 represents the comparisons between the POD-ANN

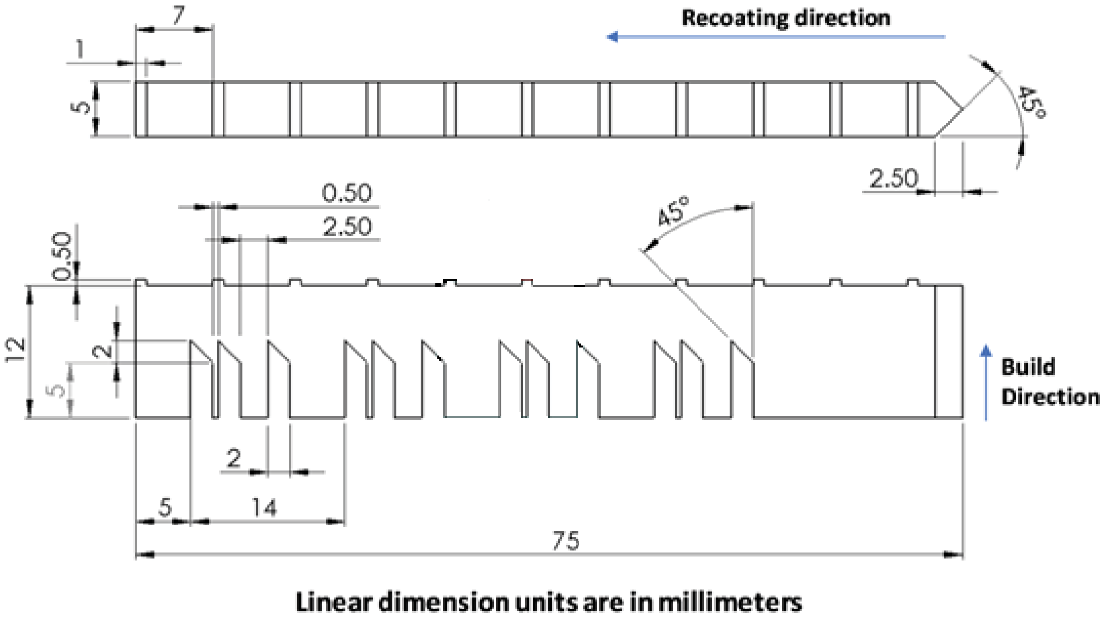

a) 2D representation of the AMB2018-01 bridge geometry from a plan and an elevation view.

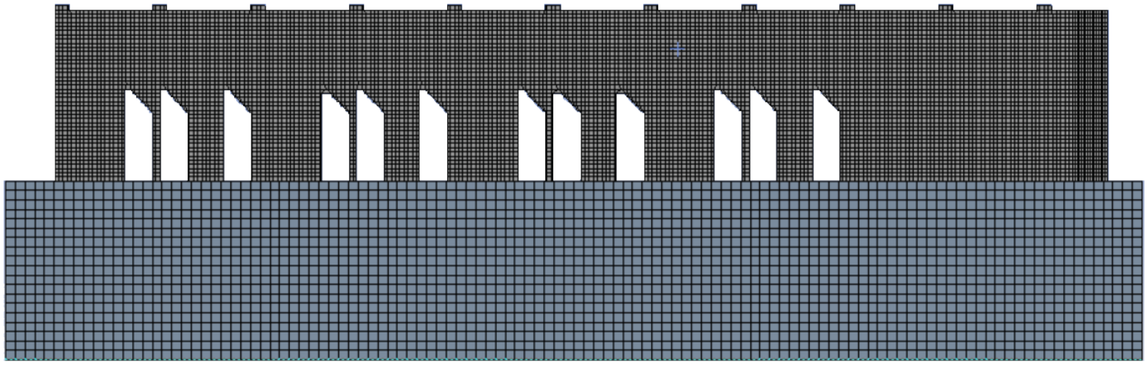

b) Mesh of the bridge and the substrate using workbench additive software.

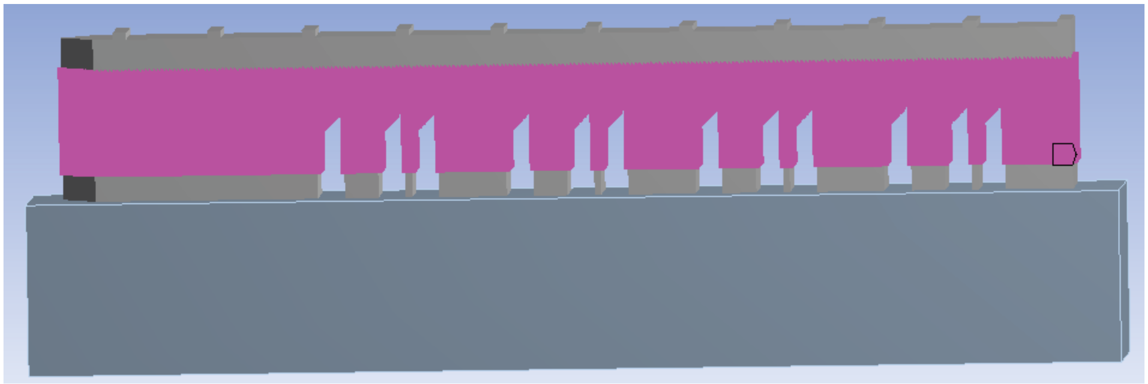

c) Representation of nodes considered to extract the strain results.

Figure 4.7 Pictorial representation AMB2018-01 bridge structure predictions and the snapshot matrix for the whole domain and with different directional strains. The POD-ANN uses the Adam optimizer and the ReLu activation function to get the better results during the learning and prediction phases. The number of POD modes for each normal strain are calculated using the truncation error δ,which is e-05, e-06, and e-07 for the x, y and z directional strains, respectively. It is found that 19, 42 and 66 POD modes are sufficient to make a surrogate model for the given snapshot matrix; the error graph in fig 4.8 proves the same. Figure 4.9 shows that the mean and the std results correlate well with the original snapshot matrix. The strain graphs prove that the body has undergone compression at some locations and expansion in others. The comparison between the mean and std results suggests that the predictions are accurate. This model can be used to calculate the strain at any given point in the geometry and for an unseen input parameter within the training intervals. The results along a random cross-section of the bridge are provided in figure 4.10. Other details related to the POD-ANN structure and effects are presented in table 4.3.

Table 4.3 POD-ANN structure

	POD mode	**Hidden layer of ANN**	**Neurons in each layer**	**Training time(sec)**	**Prediction time(sec)**	**Relative L2 error mean**	**Relative L2 error std**
X strain	19	4	100	413.024	40.96	3.7210-05	0.0148
Y strain	42	5	30	226.7586	39.6269	6.9810-06	0.00871
Z strain	66	5	50	290.95	37.41	1.89810-05	0.0040

Similar to the heat transfer test case, the spatial autoencoder structure is composed of 1D convolution layers with 10 and 15 channels along with the max pooling layers and non-linear activation function (Prelu), which help to reduce the spatial dimension from 97360 to 19, 40 and 60 for the x, y, and z directional strains, respectively. The reduced dimensions represent the spatial latent space and are directly connected to the input parameters with an MLP model. Figure 4.2 shows a working flowchart of the CAE-MLP working model, and the detailed architecture of the CAE-spatial and the MLP are presented in appendix Tables I-4 I-5 and I-6. During the training process, the CAE is trained for 500 epochs, followed by the MLP for 1000 epochs. The convergence history

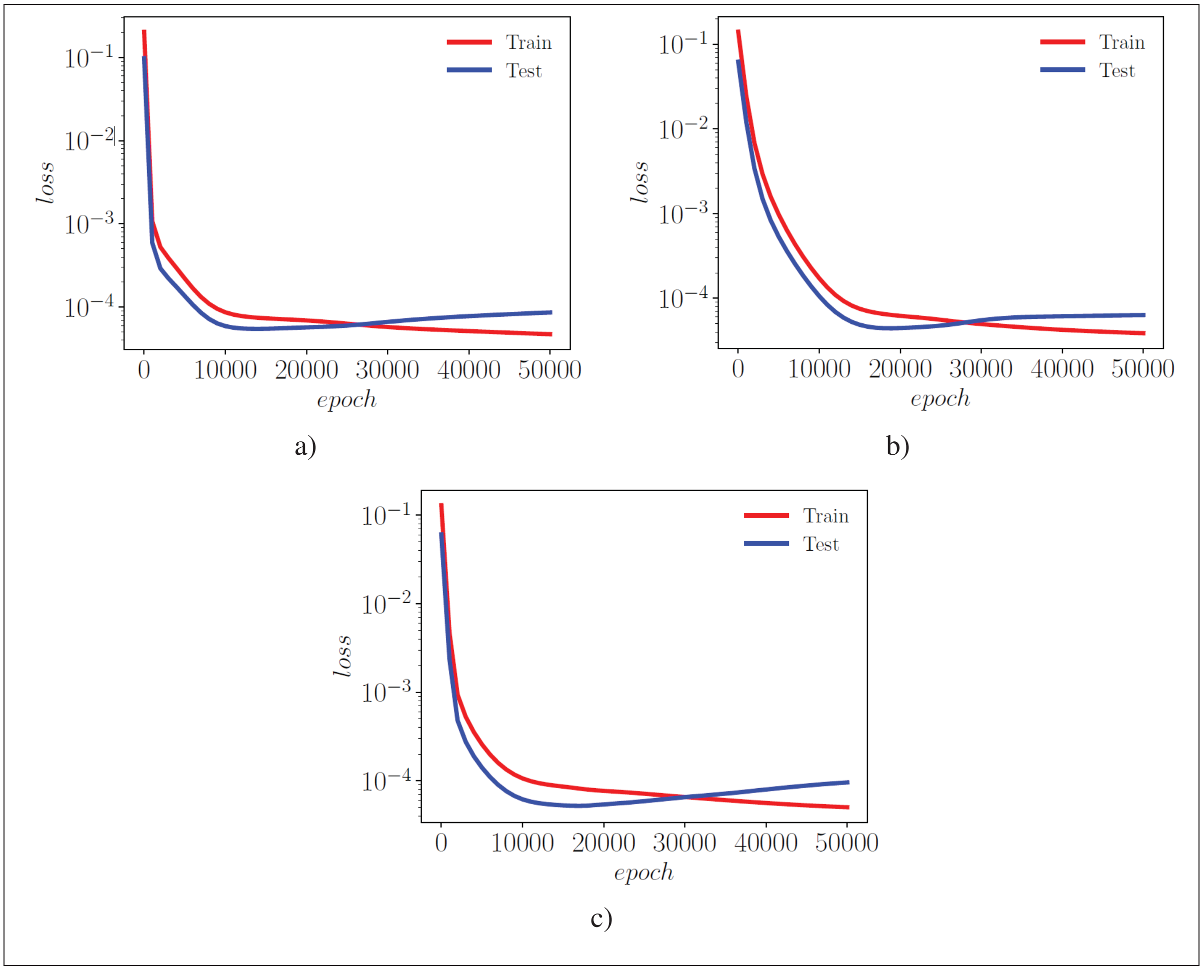

a)

b)

c)

Figure 4.8 Error graphs for the POD-ANN for the x, y and z strains represented by figure (a), (b) and (c), respectively

of the CAE and the MLP for the x, y and z strains is presented in Figures I-1 I-2 I-3 in the appendix.

The CAE-MLP model is trained over the original snapshot matrices for x, y, and z separately, and the calculated outputs are presented in terms of standard deviation and mean. Similar to the POD-ANN process, the trained CAE-MLP model is applied to find the outputs for a new data set of 5000 samples, and the variations in the statistical moments are compared with the original snapshot matrices for each normal strain. Figures 4.9 and 4.10 show the variations in the CAE-MLP predictions, for the original snapshot matrices for the whole domain and for a random cross-section of AMB2018-01, respectively, to better visualize the results. The results from the CAE-MLP are also compared with those of the POD-ANN in figures 4.9 and 4.10, and listed in table 4.4. A complete architecture of the CAE-MLP model for different strains is shown in appendix Tables I-4 I-5 and I-6. Both models are trained with 80% of the initial snapshot matrix; the rest of the information, 20%, is used to test the models. Compared to the POD-ANN, the CAE-MLP model takes more time to train and predict, but the CAE-MLP predictions are better than those of the POD-ANN. The L2 norm between the statistical moments of CAE-MLP predictions and the snapshot matrix is less than the POD-ANN prediction for all the strains. Table 4.4 lists the results of both models for easy comparison.

Table 4.4 Comparison of POD-ANN and CAE-MLP results

	Modes	**Relative L2 error for mean**	**Relative L2 error for std**
POD-ANN x strain	19	0.00037	0.0149
CAE-MLP x strain	19	0.0001	0.0038
POD-ANN y strain	44	0.0006	0.0088
CAE-MLP y strain	40	0.0001	0.0014
POD-ANN z strain	66	0.000017	0.0039
CAE-MLP z strain	60	0.0002	0.00049

4.3.3 Comparison with experimental results

This section compares both the models and the experimental outputs. The means of the 5000 sample outputs from both models are compared with the experimental data at location z = 9.536, as shown in Fig 4.5. These outcomes are also compared with the outputs generated from the DNN model in (Chaudhry & Soulaïmani, 2022) over the same cross-section. Chaudhry & Soulaïmani (2022) constructed a surrogate model using the DNN model for the normal strains over the experimental location z = 9.536 with only 251 nodes. Comparing the three models indicates that the reduced-order models constructed over the whole geometry provide better results than the DNN model built with just a cross-section. The new approaches improve the accuracy of the results by 60%-80%. The CAE-MLP offered significantly better results than the DNN, and even improved on the POD-ANN, providing better results for all three normal strains. The relative

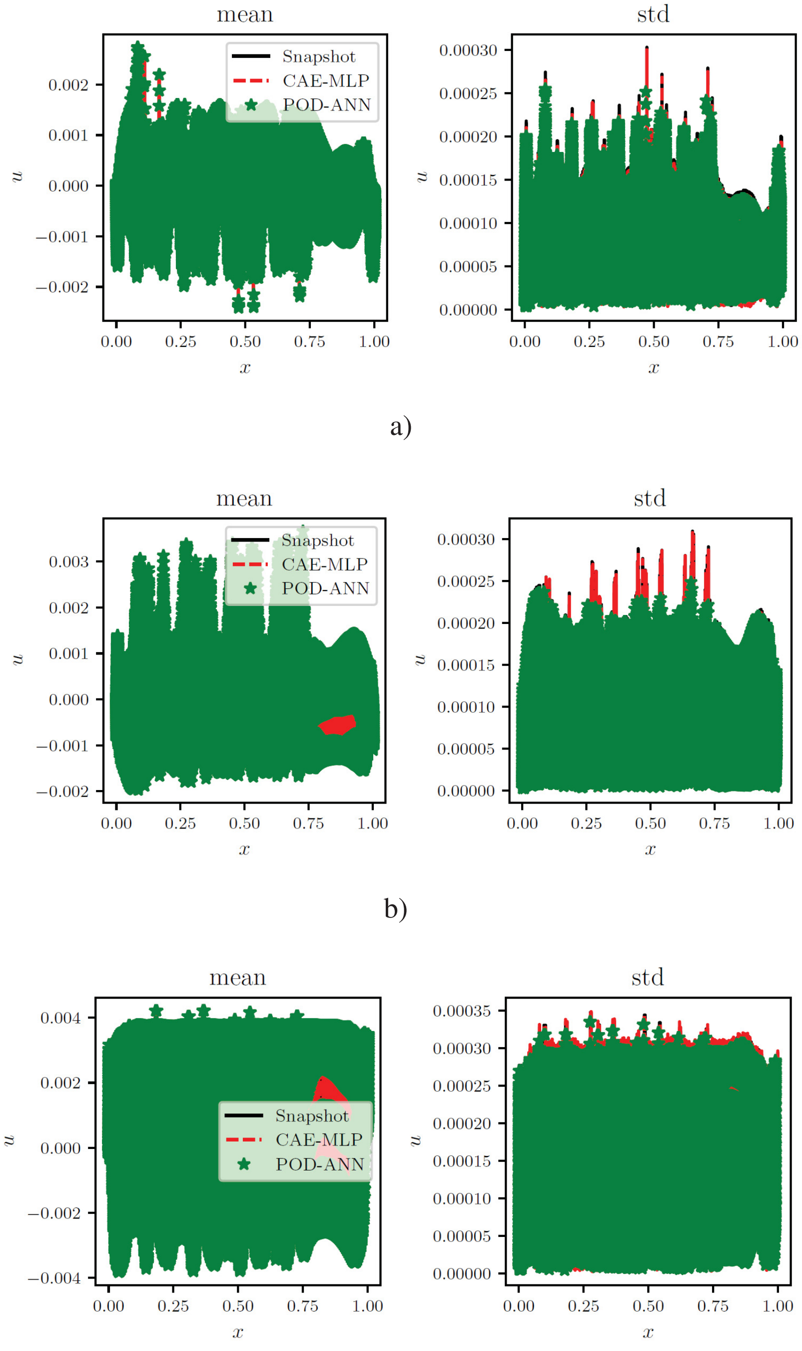

a)

b)

c)

Figure 4.9 Comparison of POD-ANN and CAE-MLP with the snapshot matrices of the x, y and z strain represented in a, b and c, respectively, for the whole domain

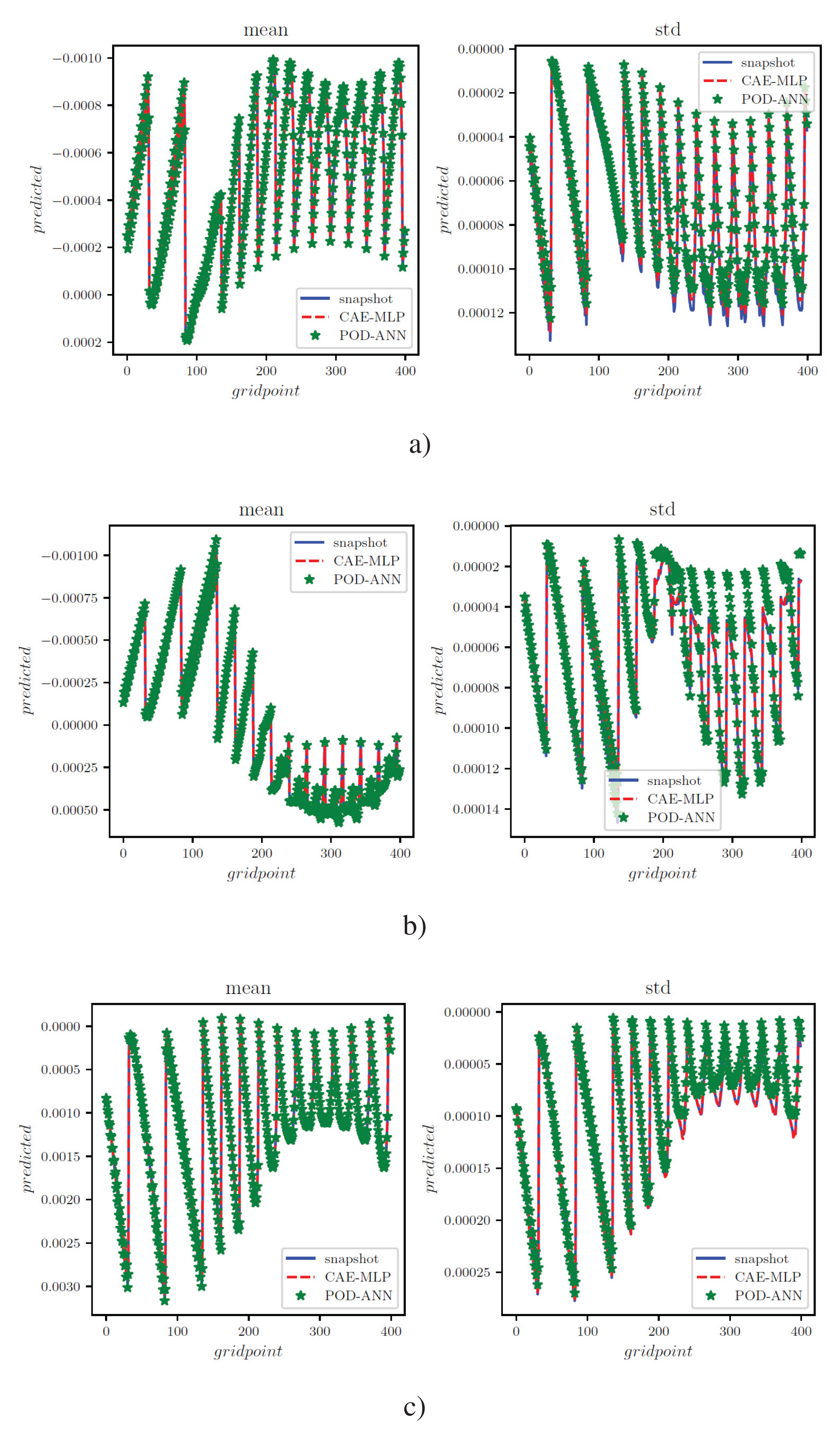

a)

b)

c)

Figure 4.10 Comparison of POD-ANN and CAE-MLP with the snapshot matrices of the x, y and z strain represented in a, b and c, respectively, for a cross-section

L2 norm values for the models and the experimental data are presented in Table 4.5 for each directional strain.

In addition, the prediction results for normal directions with the POD-ANN and CAE-MLP are compared with the experimental results at three different locations. Fig 4.12 shows the good correlation between the experimental outputs and the predictions at z= 8.25 mm, 8.75mm and 9.25mm. These results prove the abilities of the proposed technique to accurately predict strain values across the whole domain.

Table 4.5 Comparison of the POD-ANN and CAE-MLP models with the experimental results for normal strains in the x, y, and z directions

	POD-ANN	**CAE-MLP**	**DNN**
x strain	0.040	0.039	0.271
CAE-MLP x strain	0.234	0.212	0.658
POD-ANN y strain	0.789	0.74	0.873

4.4 Conclusion

This study presented the non-intrusive reduced-order models POD-ANN and CAE-MLP to analyse the selective laser melting process. The use of proper orthogonal decomposition and a deep convolution autoencoder to construct the reduced order models has proven to be efficient and effective approaches.

The models are entirely data-driven and combine several techniques from reduced-order modelling and machine learning. Both models work in two phases, with the first being an offline phase and the other an online phase. The offline phase uses a high-fidelity 97360×360 snapshot matrix of normal strains created using the workbench additive software. In the offline phase, proper orthogonal decomposition for POD-ANN and an autoencoder for the CAE-MLP are used to reduce the snapshot matrix' dimension. The autoencoder consists of two levels; the first is the encoder, which performs the compression along the spatial dimension and generates a low-dimensional latent space of the snapshot matrix. The second level is the decoder, which

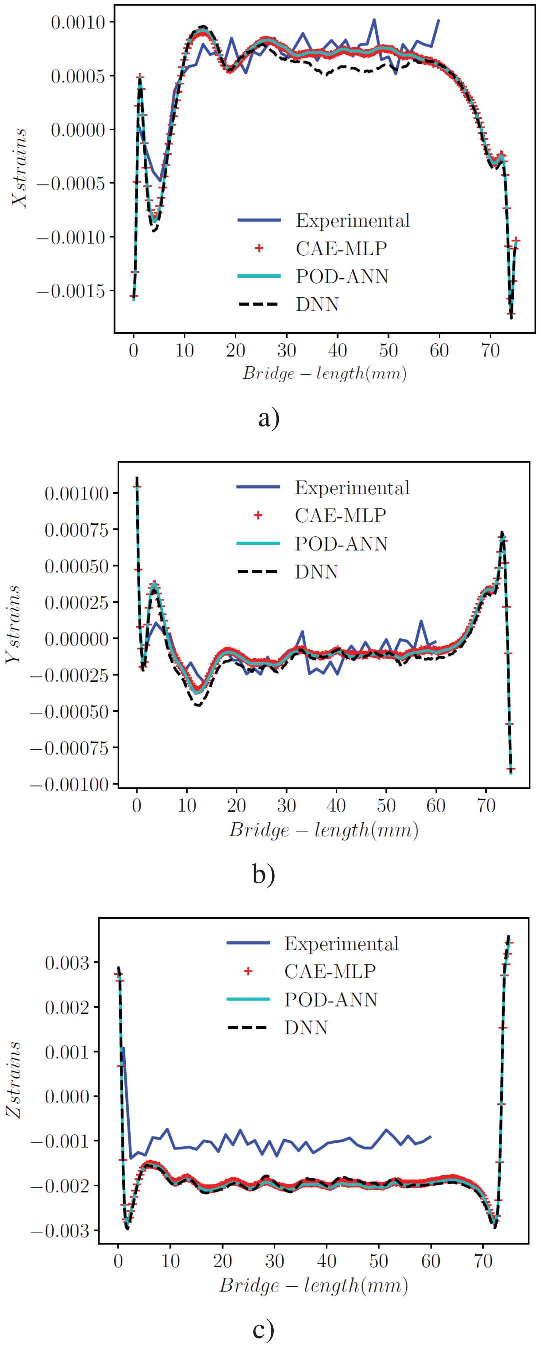

a)

b)

c)

Figure 4.11 Comparison of POD-ANN and CAE-MLP with the snapshot matrices of the x, y and z strain represented in a, b and c, respectively, for a cross-section

converts the latent space back to the original dimension. In the offline phase, the reduced dimension of the latent space is used as an output and is projected to the input variables with

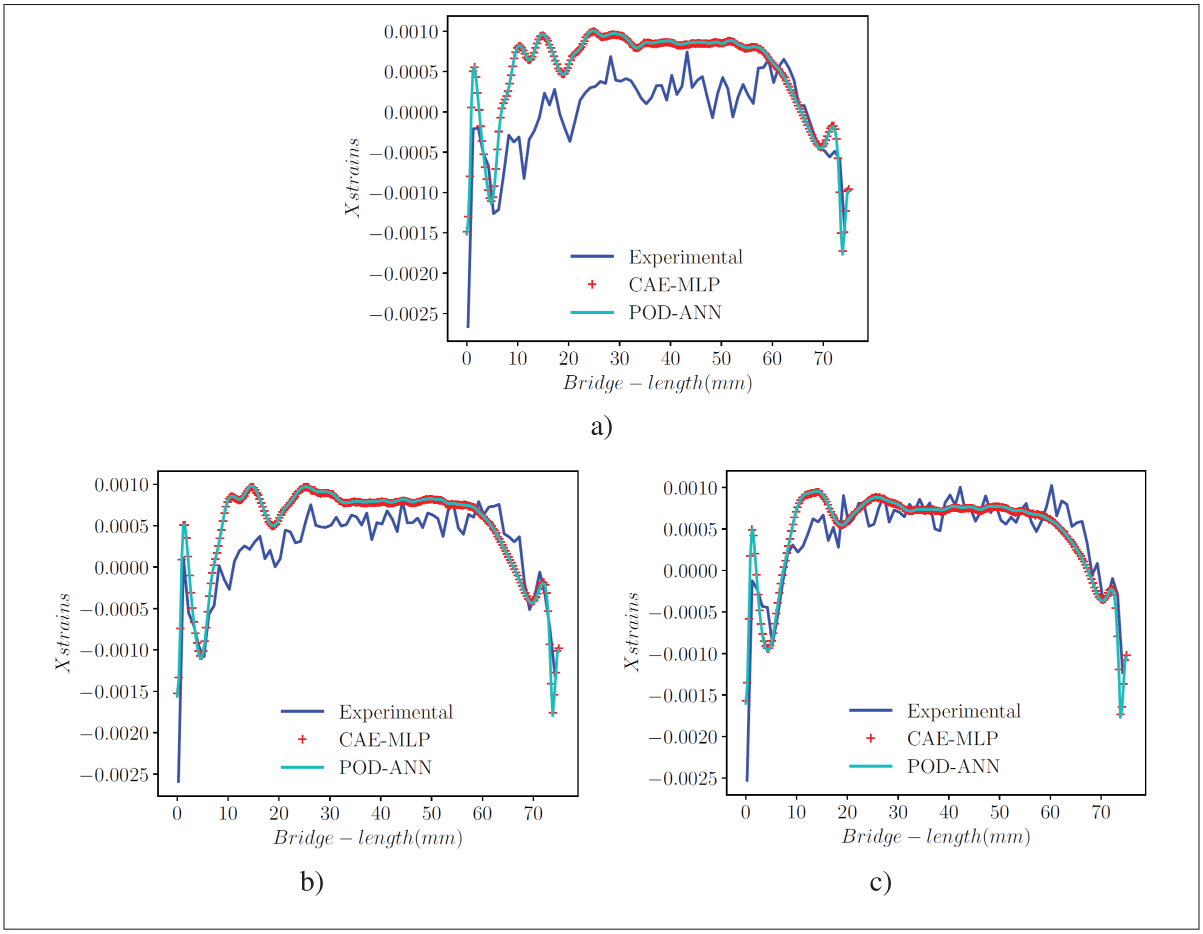

a)

b)

c)

Figure 4.12 Comparison of the x strains found with the POD-ANN and CAE-MLP models with the experimental results at z = 8.25, 8.75 and 9.25, in a, b and c, respectively

the help of the multilayer perceptron (MLP). Once the training is completed in the offline phase, the second, online phase is initiated. The online stage is provided with a new data set of input variables, and the trained offline step is used to predict the outputs on those points. The outputs from the trained MLP are used as inputs for the decoder in the CAE-MLP, and are then transferred from the spatial dimension back to their original dimension.

The efficiency and performance of the proposed approaches are evaluated using a heat transfer test case and an SLM benchmark test case provided by the NIST. Both cases are parameterized with the input variables in a ±15% range. The first test case concerns heat transfer through a fin. The excellent correlation of the POD-ANN and CAE-MLP predictions with the high-fidelity numerical results validates the models' implementation. In the AMB2018-01 SLM benchmark test case, the CAE-MLP provides a satisfactory approximation of the statistical moments with respect to the original snapshot matrix compared to the POD-ANN for a new input set generated with the LHS sampling method. The relative error norm of the CAE-MLP is less than that of the POD-ANN, which further proves its ability to model a nonlinear complex problem. In addition, the statistical moments of the predictions from both approaches were compared with the experimental data and the results were calculated using a DNN model over a single cross-section at z=9.536mm in (Chaudhry & Soulaïmani, 2022). Interestingly, the predictions from both approaches correlate better with the experimental results than the DNN method used in that study (Chaudhry & Soulaïmani, 2022). The new approach increases the prediction accuracy by 60%-80%. The outputs from the predictions are further compared with the other experimental results at different locations, and, as with other studies, both the models provide a good comparison; however, CAE-MLP gives a better comparison than the POD-ANN. Thus, the proposed non-intrusive reduced-order model based on proper orthogonal decomposition and a convolution autoencoder provides a powerful tool with which to study the highly nonlinear and complex physical problem by reducing the problem's dimension. Both models offer better surrogate models with high precision and good efficiency.

CONCLUSION AND RECOMMENDATIONS

The research work presented in this thesis is focused on the construction of numerical modeling and optimization of the selective laser melting (SLM) process using data-driven machine learning methods. The additive manufacturing industry is in need of new techniques or framework to reduce operational costs, and material wastage and increase production with better quality of the built part. Thus, this thesis work contributes multiple advantages to the research community by providing a detailed framework for faster numerical simulation, uncertainty propagation and sensitivity analysis, along with optimizing the SLM process. The framework implements effective procedures and already existing methods and also proposes new approaches whose effectiveness has been demonstrated and whose implementations can be extended to other research areas in engineering.

Initially, a numerical model of SLM process is constructed with the ANSYS additive software to analyze the mechanical properties of the SLM-built part. However, the numerical model works with some hyperparameters, like SSF and anisotropic coefficients, that must be calibrated precisely to construct a better simulation model of an SLM process. A new and efficient calibration technique was introduced, which has the potential to predict the mechanical properties of a given experimental SLM study. The abilities of the proposed method have been assessed by comparing the prediction with three different experimental studies. The new calibration strategy significantly improves the convergence time, and the results are close to the experimental values. The relaxation factor is considered to be 3/4, which helps to consider the deformation history of the product in order to calculate the new SSF and the anisotropic coefficients for the next iteration.

Subsequently, a framework is proposed to analyze and optimize the SLM process other than the more widely used experimental and numerical techniques. The approach combines machine learning (ML) methods with the SLM numerical model to study mechanical properties in the SLM-built part and optimize the process parameters. The neural networks and polynomial chaos expansions (PCE) were considered to be the primary machine learning methods. At first a dataset of full-order numerical solutions was performed using ANSYS workbench additive software. The simulation results were validated using publicly available experimental results. After the validation, the 3D thermo-mechanical finite element model was used to solve a set of 360 samples created using the Sobol sampling technique. A data-driven surrogate model is constructed between the SLM inputs and outputs with the help of data generated from 360 samples. Both the primary ML models were trained and tested with the 80% of and 20% of the constructed simulation results. It was found that the deep neural network model performed better and faster than the PCE model, so the DNN model was adopted for the rest of the analyses.

After the DNN model was selected, it was combined with the Monte Carlo technique to find the number of simulations sufficient to perform the sensitivity and uncertainty analyses in the SLM process. We calculated the standard deviation for each sample set and performed a convergence analysis to find the exact number of samples, which found that a set of 6000 samples was sufficient to perform the study. The sensitivity analysis revealed that the Young's modulus and Poisson coefficient are the most critical parameters during the process, while the layer thickness, laser speed, and hatch spacing are less important. However, the machine parameters still hold significant importance (5% to 10%). So it is advisable not to discard the machine parameters from the process, and we considered all five parameters for the optimization analysis too. In order to perform the reverse analysis for the optimized parameter, the DNN model was taken as a black box for the SLM process and it was incorporated with three different algorithms: GA, PSO, and DE. Firstly, all three algorithms performed equally well at calculating the optimal solution; however, PSO was faster and took the least time. Also, the results with the optimized parameter have shown good correlation with the experimental results too. The limitation of this approach was that we considered only a cross-section of the built part and considered only 251 nodes in the numerical simulation. But, if we have to consider the whole geometry, the number of models will be around 97360. For that, only a DNN model will not be enough to construct a surrogate model between the input parameters and the output parameters as the trainable parameters will reach millions in number, and the calculation will be computationally impossible.

To address this issue, two non-intrusive reduced-order models POD-ANN and CAE-MLP were introduced. The data-driven models combine several techniques from reduced-order modeling and machine learning. The models work in two phases, where the first is the online phase and the second is the offline phase. Initially, a high fidelity 97360×360 snapshot matrix of normal strains was created using the workbench additive software. Then in the offline phase proper orthogonal decomposition for POD-ANN and an autoencoder for the CAE-MLP are used to reduce the snapshot matrix' dimension. The proper orthogonal decomposition constructs the reduced order bases for the snapshot matrix and then an ANN model was developed to create a surrogate model between the input variables and the reduced order bases. In another case, The autoencoder consists of two levels; the first is the encoder, which performs the compression along the spatial dimension and generates a low-dimensional latent space of the snapshot matrix. In the next level, the latent space was converted back to the original dimension. Similar to the POD-ANN process, in the offline phase, the reduced dimension of the latent space is used as an output and is projected to the input variables with the help of the multilayer perceptron (MLP). Once the training is completed in the offline phase, the second online phase is initiated. In the online phase, a new data set of input variables is provided and new predictions are calculated on them. These outputs from the trained MLP were then used as input for the decoder and transferred back to the original dimension.

The performance efficiency of both models was evaluated with a heat transfer test case and an SLM benchmark test case provided by the NIST. In the first case, a heat transfer model of a fin was considered, and the excellent correlation of the statistical moments from POD-ANN and CAE-MLP predictions with the high-fidelity numerical results validates the models' implementation. In the SLM benchmark test case, the CAE-MLP provides a satisfactory approximation of the statistical moments with respect to the original snapshot matrix compared to the POD-ANN for a new input set generated with the LHS sampling method. The relative L2 error norm of the CAE-MLP is less compared to the POD-ANN and thus proves the abilities of non-linear reduced order models to capture nonlinear complex problems. In addition, the statistical moments of the predictions from both approaches were compared with the experimental data and the results were calculated using a DNN model over a single cross-section at z=9.536mm in the previous study (Chaudhry & Soulaïmani, 2022). The predictions from both approaches correlate better with the experimental results than the DNN method used in that study (Chaudhry & Soulaïmani, 2022). The new approach increases the prediction accuracy by 60%-80% and proves that if the nodes for the whole geometry are considered rather than just a cross-section, we can get better predictions from the surrogate models. The predictions from both the models were compared with the other experimental results at different locations, and both models provide a good comparison; however, as proven before, the CAE-MLP gives a better comparison than the POD-ANN. Therefore, the proposed non-intrusive reduced-order model based on a convolution autoencoder and proper orthogonal decomposition provides a powerful tool to study the highly nonlinear and complex physical problem. Thus the proposed methodologies and frameworks in this thesis have proven to be efficient not only for the SLM process but can be used for all the other research fields too.

Future work

In our current thesis work, we proposed a framework to optimize and construct a data-driven non-intrusive surrogate model for SLM to fasten and improve the quality of the built part. However, the study considers the spatial dimension during reduced-order modeling. The future aspect of the work would be to consider the temporal dimension, which will help us monitor the mechanical properties during the construction phase. Also, it will be possible to stop the process in the early stage in case of any defect detection, which will save operational costs and time.

In addition, this research considered only five parameters because of the software limitations. So, using an advanced version of SLM simulation software is recommended, where it is possible to consider more input variables. for example, a specific scan pattern is recommended instead of melting the whole layer at once. Also, the present study didn't consider laser power or intensity, laser diameter, etc., So the laser parameters must be considered for future work. The large number of variables will provide more insights into the SLM process, and the same framework can be used to find the essential parameters for the process and then optimize them for a better SLM output product.

The framework uses ML-based methods to optimize and speed up the procedure. However, there is significant concern about using ML algorithms due to the discrepancy in their predictions, which can lead to AM process loss or vandalism. Thus, robust transferable and big data-driven ML algorithms are suggested to minimize or eliminate any machine and process errors. Another way to eliminate these errors is by considering newly emerged ML algorithms like few-shot learning, which only requires a small dataset and can provide better results.

In general, the experimental approach is time-consuming and expensive; on the other hand, the simulation approach may not provide reliable physics due to the simplification and assumptions that were considered during the simulation process. For the future, an ML-assisted simulation approach is recommended. The synergy of ML-assisted simulation can reduce the computation cost significantly, and it is possible to explore the AM modeling and simulation at a large scale and for more variables. Some examples of such techniques are physics-informed ML models. There are a number of research areas and questions that can be answered with the relationship between AM and ML. Such as

- thermophysical properties
- microstructure prediction
- surface finish
- topology optimization
- material powder effect on SLM output
- support structure optimization

The application of ML for AM is still rarely explored. For example, deep-learning methods have been implemented for AM topology optimization(TO); however, most work is done only in 2D structures. As AM is a group of 3D manufacturing technologies, only TO for 3D geometries is helpful for the process. The methodology and the framework used in current research work can be extended to topology optimization of AM process for 3D geometries. Also, the framework is not only limited to the AM process but it can also be used to explore other research areas too.

APPENDIX I

APPENDIX EXAMPLE

1. Architecture of reduced order modeling

Table-A I-1 CAE space encoder architecture for the heat transfer test case

	Filters	**Activation function**	**Kernel shape**
Input	-	-	-
conv-pooling	32	Prelu	3×2
conv-pooling	68	Prelu	3×2
conv-pooling	128	Prelu	3 ×2
Flatten	-	-	-
Dense	-	Prelu	-
dense(output-L_x)	-	Prelu	-

Table-A I-2 CAE space decoder architecture for the heat transfer test case

	Filters	**Activation function**	**Kernel shape**
Input	-	-	-
Dense	-	Prelu	-
Reshape	-	Prelu	-
conv-upsamp	128	Prelu	3×2
conv-upsam	68	Prelu	3×2
conv-upsamp	32	Prelu	3×2
Output	1	Prelu	3

Table-A I-3 MLP architecture for heat transfer case

Layer type	**Output Size**	**Activation function**
Input layer	2	Prelu
Dense layer	128	Prelu
Dense layer	128	Prelu
Dense layer	128	Prelu
Output layer	L_x=5	Linear

Table-A I-4 CAE space encoder architecture for AMB2018-01 benchmark case

	Filters	**Activation function**	**Kernel shape**
Input	-	-	-
conv-pooling	10	Prelu	3×2
conv-pooling	15	Prelu	3×2
Flatten	-	-	-
Dense	-	Prelu	-
dense(output-L_x)	-	Prelu	-

Table-A I-5 CAE space decoder architecture for AMB2018-01 benchmark case

	Filters	**Activation function**	**Kernel shape**
Input	-	-	-
Dense	-	Prelu	-
Reshape	-	Prelu	-
conv-upsamp	15	Prelu	3×2
conv-upsamp	10	Prelu	3×2
Output	1	Prelu	3

Table-A I-6 MLP architecture for AMB2018-01 benchmark case

Layer type	**Output Size**	**Activation function**
Input layer	5	Prelu
Dense layer	128	Prelu
Dense layer	128	Prelu
Dense layer	128	Prelu
Output layer	$6L_x$=19,40,60	Linear

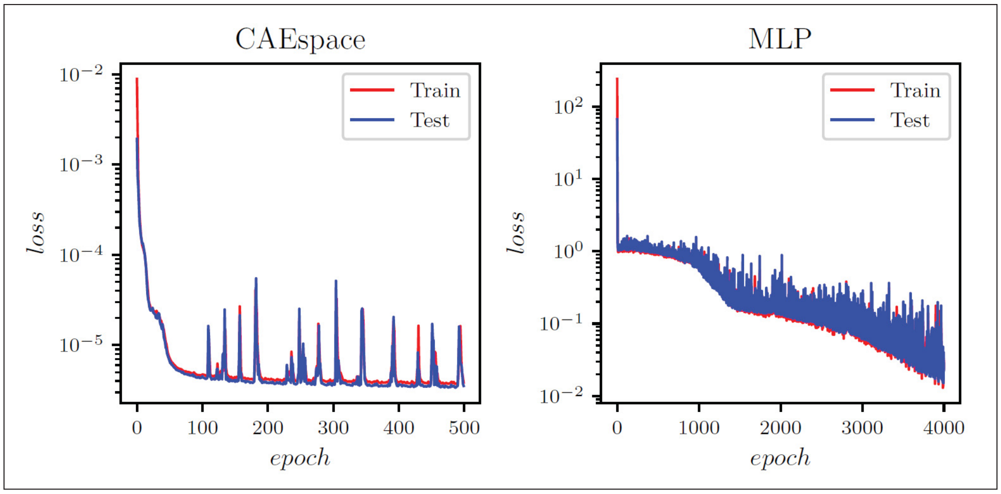

Figure-A I-1 Evolution of the training and validation error for the x-strain in the AMB2018-01 benchmark case

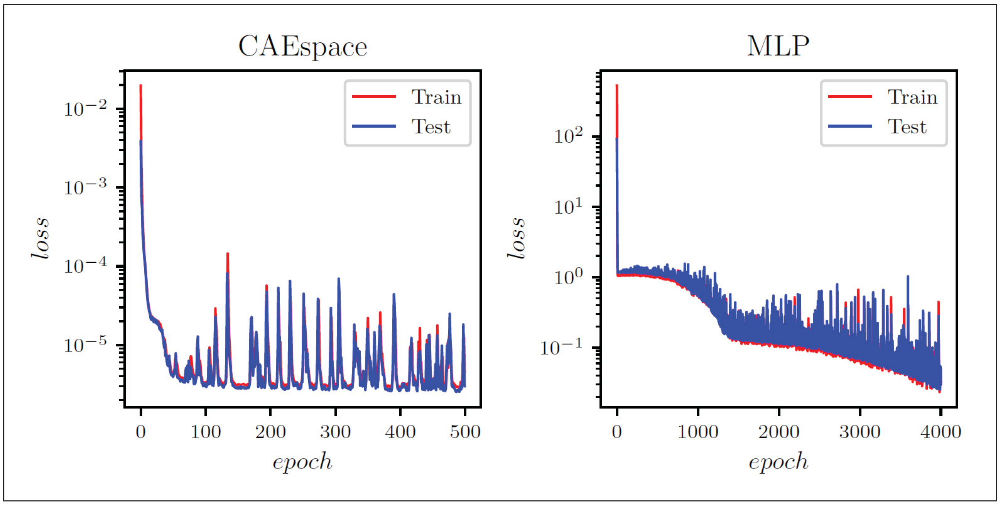

Figure-A I-2 Evolution of the training and validation error for the y-strain in the AMB2018-01 benchmark case

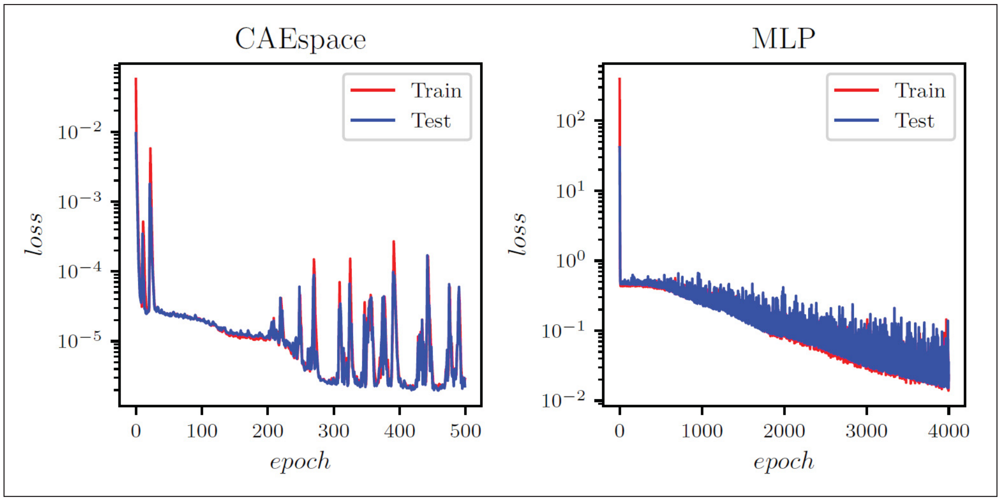

Figure-A I-3 Evolution of the training and validation error for the z-strain in the AMB2018-01 benchmark case

BIBLIOGRAPHY

Abadi, M., Barham, P., Chen, J., Chen, Z., Davis, A., Dean, J., Devin, M., Ghemawat, S., Irving, G., Isard, M. et al. (2016). {TensorFlow}: a system for {Large-Scale} machine learning. *12th USENIX symposium on operating systems design and implementation (OSDI 16)*, pp. 265–283.

Abdedou, A. & Soulaimani, A. (2019). A non-intrusive B-splines Bézier elements-based method for uncertainty propagation. *Computer Methods in Applied Mechanics and Engineering*, 345, 774–804.

Abdedou, A. & Soulaïmani, A. (2021). A non-intrusive reduced-order modeling for uncertainty propagation of time-dependent problems using a b-splines bézier elements-based method and proper orthogonal decomposition: Application to dam-break flows. *Computers & Mathematics with Applications*, 102, 187–205.

Abdedou, A. & Soulaimani, A. (2023). Reduced-order modeling for stochastic large-scale and time-dependent flow problems using deep spatial and temporal convolutional autoencoders. *Advanced Modeling and Simulation in Engineering Sciences*, 10(1), 1–27.

Abdulhameed, O., Al-Ahmari, A., Ameen, W. & Mian, S. H. (2019). Additive manufacturing: Challenges, trends, and applications. *Advances in Mechanical Engineering*, 11(2), 1687814018822880.

Abe, F., Osakada, K., Shiomi, M., Uematsu, K. & Matsumoto, M. (2001). The manufacturing of hard tools from metallic powders by selective laser melting. *Journal of materials processing technology*, 111(1-3), 210–213.

Aboulkhair, N. T., Everitt, N. M., Ashcroft, I. & Tuck, C. (2014). Reducing porosity in AlSi10Mg parts processed by selective laser melting. *Additive manufacturing*, 1, 77–86.

Aboutaleb, A. M., Bian, L., Elwany, A., Shamsaei, N., Thompson, S. M. & Tapia, G. (2017). Accelerated process optimization for laser-based additive manufacturing by leveraging similar prior studies. *IISE Transactions*, 49(1), 31–44.

Afazov, S., Denmark, W. A., Toralles, B. L., Holloway, A. & Yaghi, A. (2017). Distortion prediction and compensation in selective laser melting. *Additive Manufacturing*, 17, 15–22.

Ahn, D.-G. (2021). Directed energy deposition (DED) process: State of the art. *International Journal of Precision Engineering and Manufacturing-Green Technology*, 8, 703–742.

Angelone, R., Caggiano, A., Teti, R., Spierings, A., Staub, A. & Wegener, K. (2020). Bio-intelligent selective laser melting system based on convolutional neural networks for in-process fault identification. *Procedia CIRP*, 88, 612–617.

Ansys. Additive Calibration Plan.pdf.

ANSYS. *Workbench Additive Manufacturing Analysis Guide*.

Arora, R. K. (2015). *Optimization: algorithms and applications*. CRC press.

Asserin, O., Loredo, A., Petelet, M. & Iooss, B. (2011). Global sensitivity analysis in welding simulations—what are the material data you really need? *Finite elements in analysis and design*, 47(9), 1004–1016.

Baghi, A. D., Nafisi, S., Hashemi, R., Ebendorff-Heidepriem, H. & Ghomashchi, R. (2021). Effective post processing of SLM fabricated Ti-6Al-4 V alloy: Machining vs thermal treatment. *Journal of Manufacturing Processes*, 68, 1031–1046.

Ballantyne, K., Van Oorschot, R. & Mitchell, R. (2008). Reduce optimisation time and effort: Taguchi experimental design methods. *Forensic Science International: Genetics Supplement Series*, 1(1), 7–8.

Baturynska, I. (2019). Application of machine learning techniques to predict the mechanical properties of polyamide 2200 (PA12) in additive manufacturing. *Applied Sciences*, 9(6), 1060.

Bauereiß, A., Scharowsky, T. & Körner, C. (2014). Defect generation and propagation mechanism during additive manufacturing by selective beam melting. *Journal of Materials Processing Technology*, 214(11), 2522–2528.

Berger, M. J. & Oliger, J. (1984). Adaptive mesh refinement for hyperbolic partial differential equations. *Journal of computational Physics*, 53(3), 484–512.

Białecki, R., Kassab, A. & Fic, A. (2005). Proper orthogonal decomposition and modal analysis for acceleration of transient FEM thermal analysis. *International journal for numerical methods in engineering*, 62(6), 774–797.

Bian, L., Shamsaei, N. & Usher, J. M. (2017). *Laser-based additive manufacturing of metal parts: modeling, optimization, and control of mechanical properties*. CRC Press.

Bishop, C. M. & Nasrabadi, N. M. (2006). *Pattern recognition and machine learning*. Springer.

Blatman, G. & Sudret, B. (2010). An adaptive algorithm to build up sparse polynomial chaos expansions for stochastic finite element analysis. *Probabilistic Engineering Mechanics*, 25(2), 183–197.

Boschetto, A., Bottini, L., Macera, L. & Veniali, F. (2020). Post-processing of complex SLM parts by barrel finishing. *Applied Sciences*, 10(4), 1382.

Bruna-Rosso. (2018). Selective laser melting finite element modeling: Validation with high-speed imaging and lack of fusion defects prediction. *Materials & Design*, 156, 143–153.

Bruna-Rosso, C., Demir, A. G., Vedani, M. & Previtali, B. (2018). Global sensitivity analyses of a selective laser melting finite element model: influential parameters identification. *The International Journal of Advanced Manufacturing Technology*, 99, 833–843.

Caggiano, A., Zhang, J., Alfieri, V., Caiazzo, F., Gao, R. & Teti, R. (2019). Machine learning-based image processing for on-line defect recognition in additive manufacturing. *CIRP annals*, 68(1), 451–454.

Cai, G. & Mahadevan, S. (2016). Uncertainty quantification of manufacturing process effects on macroscale material properties. *International Journal for Multiscale Computational Engineering*, 14(3).

Caiazzo, F. & Caggiano, A. (2018). Laser direct metal deposition of 2024 Al alloy: trace geometry prediction via machine learning. *Materials*, 11(3), 444.

Cansizoglu, O., Harrysson, O., Cormier, D., West, H. & Mahale, T. (2008). Properties of Ti–6Al–4V non-stochastic lattice structures fabricated via electron beam melting. *Materials Science and Engineering: A*, 492(1-2), 468–474.

Carlberg, K. T., Barone, M. F. & Antil, H. (2015). *Galerkin v. discrete-optimal projection in nonlinear model reduction*.

Carraturo, M., Jomo, J., Kollmannsberger, S., Reali, A., Auricchio, F. & Rank, E. (2020). Modeling and experimental validation of an immersed thermo-mechanical part-scale analysis for laser powder bed fusion processes. *Additive Manufacturing*, 36, 101498.

Chatterjee, A. (2000). An introduction to the proper orthogonal decomposition. *Current science*, 808–817.

Chaudhry, S. & Soulaïmani, A. (2022). A comparative study of machine learning methods for computational modeling of the selective laser melting additive manufacturing process. *Applied Sciences*, 12(5), 2324.

Chen, H. & Zhao, Y. F. (2015). Learning algorithm based modeling and process parameters recommendation system for binder jetting additive manufacturing process. *International Design Engineering Technical Conferences and Computers and Information in Engineering Conference*, 57045, V01AT02A029.

Cheng, B., Shrestha, S. & Chou, K. (2016). Stress and deformation evaluations of scanning strategy effect in selective laser melting. *Additive Manufacturing*, 12, 240–251.

Childs, T., Hauser, C. & Badrossamay, M. (2004). Mapping and modelling single scan track formation in direct metal selective laser melting. *CIRP Annals*, 53(1), 191–194.

Childs, T., Hauser, C. & Badrossamay, M. (2005). Selective laser sintering (melting) of stainless and tool steel powders: experiments and modelling. *Proceedings of the Institution of Mechanical Engineers, Part B: Journal of Engineering Manufacture*, 219(4), 339–357.

Chowdhury, S. & Anand, S. (2016). Artificial neural network based geometric compensation for thermal deformation in additive manufacturing processes. *International Manufacturing Science and Engineering Conference*, 49910, V003T08A006.

Criales, L. E., Arısoy, Y. M. & Özel, T. (2016). Sensitivity analysis of material and process parameters in finite element modeling of selective laser melting of Inconel 625. *The International Journal of Advanced Manufacturing Technology*, 86, 2653–2666.

Dai, D. & Gu, D. (2014). Thermal behavior and densification mechanism during selective laser melting of copper matrix composites: Simulation and experiments. *Materials & Design*, 55, 482–491.

Dai, K. & Shaw, L. (2006). Parametric studies of multi-material laser densification. *Materials Science and Engineering: A*, 430(1-2), 221–229.

Dai, K. & Shaw, L. (2002). Distortion minimization of laser-processed components through control of laser scanning patterns. *Rapid Prototyping Journal*.

Delgado, J., Ciurana, J. & Rodríguez, C. A. (2012). Influence of process parameters on part quality and mechanical properties for DMLS and SLM with iron-based materials. *The International Journal of Advanced Manufacturing Technology*, 60, 601–610.

Deligianni, D. D., Katsala, N., Ladas, S., Sotiropoulou, D., Amedee, J. & Missirlis, Y. (2001). Effect of surface roughness of the titanium alloy Ti–6Al–4V on human bone marrow cell response and on protein adsorption. *Biomaterials*, 22(11), 1241–1251.

Denlinger. (2016). Thermal modeling of Inconel 718 processed with powder bed fusion and experimental validation using in situ measurements. *Additive Manufacturing*, 11, 7–15.

Després, N., Cyr, E., Setoodeh, P. & Mohammadi, M. (2020). Deep learning and design for additive manufacturing: a framework for microlattice architecture. *Jom*, 72, 2408–2418.

El Moçayd, N., Mohamed, M. S., Ouazar, D. & Seaid, M. (2020). Stochastic model reduction for polynomial chaos expansion of acoustic waves using proper orthogonal decomposition. *Reliability Engineering & System Safety*, 195, 106733.

Favaloro, E. & Pipes, R. B. (2017). Simulation of polymeric composites additive manufacturing using Abaqus. *Science in the Age of Experience*, 103–114.

Ferreira, R. d. S. B., Sabbaghi, A. & Huang, Q. (2019). Automated geometric shape deviation modeling for additive manufacturing systems via Bayesian neural networks. *IEEE Transactions on Automation Science and Engineering*, 17(2), 584–598.

Fic, A., Białecki, R. A. & Kassab, A. J. (2005). Solving transient nonlinear heat conduction problems by proper orthogonal decomposition and the finite-element method. *Numerical Heat Transfer, Part B: Fundamentals*, 48(2), 103–124.

Fischer, P., Romano, V., Weber, H.-P., Karapatis, N., Boillat, E. & Glardon, R. (2003). Sintering of commercially pure titanium powder with a Nd: YAG laser source. *Acta Materialia*, 51(6), 1651–1662.

Francis, J. & Bian, L. (2019). Deep learning for distortion prediction in laser-based additive manufacturing using big data. *Manufacturing Letters*, 20, 10–14.

Fu, C. & Guo, Y. (2014). Three-dimensional temperature gradient mechanism in selective laser melting of Ti-6Al-4V. *Journal of Manufacturing Science and Engineering*, 136(6).

Gaonkar, A. & Kulkarni, S. (2015). Application of multilevel scheme and two level discretization for POD based model order reduction of nonlinear transient heat transfer problems. *Computational Mechanics*, 55, 179–191.

Georgioudakis, M. & Plevris, V. (2020). A comparative study of differential evolution variants in constrained structural optimization. *Frontiers in Built Environment*, 6, 102.

Gibson, I., Rosen, D., Stucker, B., Khorasani, M., Gibson, I., Rosen, D., Stucker, B. & Khorasani, M. (2021a). Material extrusion. *Additive Manufacturing Technologies*, 171–201.

Gibson, I., Rosen, D., Stucker, B., Khorasani, M., Gibson, I., Rosen, D., Stucker, B. & Khorasani, M. (2021b). Powder bed fusion. *Additive manufacturing technologies*, 125–170.

Gibson, I., Rosen, D., Stucker, B., Khorasani, M., Gibson, I., Rosen, D., Stucker, B. & Khorasani, M. (2021c). Sheet lamination. *Additive Manufacturing Technologies*, 253–283.

Goldak, J., Chakravarti, A. & Bibby, M. (1984). A new finite element model for welding heat sources. *Metallurgical transactions B*, 15, 299–305.

Gonzalez, F. J. & Balajewicz, M. (2018). Deep convolutional recurrent autoencoders for learning low-dimensional feature dynamics of fluid systems. *arXiv preprint arXiv:1808.01346*.

Goodfellow, I., Bengio, Y. & Courville, A. (2016). *Deep learning*. MIT press.

Gu, D. D., Meiners, W., Wissenbach, K. & Poprawe, R. (2012). Laser additive manufacturing of metallic components: materials, processes and mechanisms. *International materials reviews*, 57(3), 133–164.

Gülcan, O., Günaydın, K. & Tamer, A. (2021). The state of the art of material jetting—a critical review. *Polymers*, 13(16), 2829.

Gusarov, A. & Kovalev, E. (2009). Model of thermal conductivity in powder beds. *Physical Review B*, 80(2), 024202.

Gusarov, A. & Kruth, J.-P. (2005). Modelling of radiation transfer in metallic powders at laser treatment. *International Journal of Heat and Mass Transfer*, 48(16), 3423–3434.

Gusarov, A., Yadroitsev, I., Bertrand, P. & Smurov, I. (2007). Heat transfer modelling and stability analysis of selective laser melting. *Applied Surface Science*, 254(4), 975–979.

He, Y., Shi, H., Tan, S., Song, B. & Zhu, J. (2021). Multiblock temporal convolution network-based temporal-correlated feature learning for fault diagnosis of multivariate processes. *Journal of the Taiwan Institute of Chemical Engineers*, 122, 78–84.

Heinrich, L., Feldhausen, T., Saleeby, K. S., Saldana, C. & Kurfess, T. R. (2021). Prediction of Thermal Conditions of DED With FEA Metal Additive Simulation. *International Manufacturing Science and Engineering Conference*, 85062, V001T01A022.

Hertlein, N., Deshpande, S., Venugopal, V., Kumar, M. & Anand, S. (2020). Prediction of selective laser melting part quality using hybrid Bayesian network. *Additive Manufacturing*, 32, 101089.

Hinton, G. E. & Salakhutdinov, R. R. (2006). Reducing the dimensionality of data with neural networks. *science*, 313(5786), 504–507.

Hodge, N., Ferencz, R. & Solberg, J. (2014). Implementation of a thermomechanical model for the simulation of selective laser melting. *Computational Mechanics*, 54(1), 33–51.

Hodge, N., Ferencz, R. & Vignes, R. (2016). Experimental comparison of residual stresses for a thermomechanical model for the simulation of selective laser melting. *Additive Manufacturing*, 12, 159–168.

Holland, J. H. (1992). *Adaptation in natural and artificial systems: an introductory analysis with applications to biology, control, and artificial intelligence*. MIT press.

Horn, T. J. & Harrysson, O. L. (2012). Overview of current additive manufacturing technologies and selected applications. *Science progress*, 95(3), 255–282.

Hosder, S., Walters, R. & Perez, R. (2006). A non-intrusive polynomial chaos method for uncertainty propagation in CFD simulations. *44th AIAA aerospace sciences meeting and exhibit*, pp. 891.

Hu, Z. & Mahadevan, S. (2017). Uncertainty quantification and management in additive manufacturing: current status, needs, and opportunities. *The International Journal of Advanced Manufacturing Technology*, 93, 2855–2874.

Huang, Y., Khamesee, M. B. & Toyserkani, E. (2016). A comprehensive analytical model for laser powder-fed additive manufacturing. *Additive Manufacturing*, 12, 90–99.

Hussein, A., Hao, L., Yan, C. & Everson, R. (2013). Finite element simulation of the temperature and stress fields in single layers built without-support in selective laser melting. *Materials & Design (1980-2015)*, 52, 638–647.

Ippolito, R., Iuliano, L. & Gatto, A. (1995). Benchmarking of rapid prototyping techniques in terms of dimensional accuracy and surface finish. *CIRP annals*, 44(1), 157–160.

Jacquier, P., Abdedou, A., Delmas, V. & Soulaïmani, A. (2021). Non-intrusive reduced-order modeling using uncertainty-aware deep neural networks and proper orthogonal decomposition: Application to flood modeling. *Journal of Computational Physics*, 424, 109854.

Jandin, G., Bertin, J., Dembinski, L. & Coddet, C. (2005). Manufacture of stainless steel parts by selective laser melting process. *Proceedings of the 2nd International Conference on Advanced Research in Virtual and Rapid Prototyping, Leiria, Portugal*, 28.

Kamath, C. (2016). Data mining and statistical inference in selective laser melting. *The International Journal of Advanced Manufacturing Technology*, 86, 1659–1677.

Khairallah, S. A. & Anderson, A. (2014). Mesoscopic simulation model of selective laser melting of stainless steel powder. *Journal of Materials Processing Technology*, 214(11), 2627–2636.

Kim, K.-K. K., Shen, D. E., Nagy, Z. K. & Braatz, R. D. (2013). Wiener's polynomial chaos for the analysis and control of nonlinear dynamical systems with probabilistic uncertainties [historical perspectives]. *IEEE Control Systems Magazine*, 33(5), 58–67.

King, W. E., Barth, H. D., Castillo, V. M., Gallegos, G. F., Gibbs, J. W., Hahn, D. E., Kamath, C. & Rubenchik, A. M. (2014). Observation of keyhole-mode laser melting in laser powder-bed fusion additive manufacturing. *Journal of Materials Processing Technology*, 214(12), 2915–2925.

Koeppe, A., Padilla, C. A. H., Voshage, M., Schleifenbaum, J. H. & Markert, B. (2018). Efficient numerical modeling of 3D-printed lattice-cell structures using neural networks. *Manufacturing Letters*, 15, 147–150.

Kolossov, S., Boillat, E., Glardon, R., Fischer, P. & Locher, M. (2004). 3D FE simulation for temperature evolution in the selective laser sintering process. *International Journal of Machine Tools and Manufacture*, 44(2-3), 117–123.

Körner, C., Attar, E. & Heinl, P. (2011). Mesoscopic simulation of selective beam melting processes. *Journal of Materials Processing Technology*, 211(6), 978–987.

Kruth, J.-P., Badrossamay, M., Yasa, E., Deckers, J., Thijs, L. & Van Humbeeck, J. (2010). Part and material properties in selective laser melting of metals. *Proceedings of the 16th International Symposium on Electromachining (ISEM XVI)*, pp. 3–14.

Kusano, M., Miyazaki, S., Watanabe, M., Kishimoto, S., Bulgarevich, D. S., Ono, Y. & Yumoto, A. (2020). Tensile properties prediction by multiple linear regression analysis for selective laser melted and post heat-treated Ti-6Al-4V with microstructural quantification. *Materials Science and Engineering: A*, 787, 139549.

Lasi, H., Fettke, P., Kemper, H.-G., Feld, T. & Hoffmann, M. (2014). Industry 4.0. *Business & information systems engineering*, 6, 239–242.

Lewandowski, J. J. & Seifi, M. (2016). Metal additive manufacturing: a review of mechanical properties. *Annual review of materials research*, 46, 151–186.

Li, J., Liang, X., Liou, F. & Park, J. (2018). Macro-/micro-controlled 3D lithium-ion batteries via additive manufacturing and electric field processing. *Scientific reports*, 8(1), 1846.

Li, X.-f., Dong, J.-h. & Zhang, Y.-z. (2009). Modeling and applying of RBF neural network based on fuzzy clustering and pseudo-inverse method. *2009 International Conference on Information Engineering and Computer Science*, pp. 1–4.

Liu, B., Fang, G. & Lei, L. (2021). An analytical model for rapid predicting molten pool geometry of selective laser melting (SLM). *Applied Mathematical Modelling*, 92, 505–524.

Liu, Q., Wu, H., Paul, M. J., He, P., Peng, Z., Gludovatz, B., Kruzic, J. J., Wang, C. H. & Li, X. (2020). Machine-learning assisted laser powder bed fusion process optimization for AlSi10Mg: New microstructure description indices and fracture mechanisms. *Acta Materialia*, 201, 316–328.

Liu, X. & Liu, X. (2023). Regression Trees on Grassmann Manifold for Adapting Reduced-Order Models. *AIAA Journal*, 61(3), 1318–1333.

Lo, Y.-L., Liu, B.-Y. & Tran, H.-C. (2019). Optimized hatch space selection in double-scanning track selective laser melting process. *The International Journal of Advanced Manufacturing Technology*, 105, 2989–3006.

Löber, L., Flache, C., Petters, R., Kühn, U. & Eckert, J. (2013). Comparison of different post processing technologies for SLM generated 316l steel parts. *Rapid Prototyping Journal*, 19(3), 173–179.

Lopez, F., Witherell, P. & Lane, B. (2016). Identifying uncertainty in laser powder bed fusion additive manufacturing models. *Journal of Mechanical Design*, 138(11).

Lumley, J. L. (1967). The structure of inhomogeneous turbulent flows. *Atmospheric turbulence and radio wave propagation*, 166–178.

Luo, Z. & Zhao, Y. (2018). A survey of finite element analysis of temperature and thermal stress fields in powder bed fusion additive manufacturing. *Additive Manufacturing*, 21, 318–332.

Markl, M. & Körner, C. (2016). Multiscale modeling of powder bed–based additive manufacturing. *Annual Review of Materials Research*, 46, 93–123.

Masoomi. (2018). A numerical and experimental investigation of convective heat transfer during laser-powder bed fusion. *Additive Manufacturing*, 22, 729–745.

Masubuchi, K. (2013). *Analysis of welded structures: residual stresses, distortion, and their consequences*. Elsevier.

Matsumoto, M., Shiomi, M., Osakada, K. & Abe, F. (2002). Finite element analysis of single layer forming on metallic powder bed in rapid prototyping by selective laser processing. *International Journal of Machine Tools and Manufacture*, 42(1), 61–67.

Maulik, R., Lusch, B. & Balaprakash, P. (2021). Reduced-order modeling of advection-dominated systems with recurrent neural networks and convolutional autoencoders. *Physics of Fluids*, 33(3).

Meng, L. & Zhang, J. (2020). Process design of laser powder bed fusion of stainless steel using a Gaussian process-based machine learning model. *Jom*, 72(1), 420–428.

Meng, L., McWilliams, B., Jarosinski, W., Park, H.-Y., Jung, Y.-G., Lee, J. & Zhang, J. (2020). Machine learning in additive manufacturing: a review. *Jom*, 72, 2363–2377.

Moser, D., Fish, S., Beaman, J. & Murthy, J. (2014). Multi-layer computational modeling of selective laser sintering processes. *ASME International Mechanical Engineering Congress and Exposition*, 46438, V02AT02A008.

Mozaffar, M., Paul, A., Al-Bahrani, R., Wolff, S., Choudhary, A., Agrawal, A., Ehmann, K. & Cao, J. (2018). Data-driven prediction of the high-dimensional thermal history in directed energy deposition processes via recurrent neural networks. *Manufacturing letters*, 18, 35–39.

Nagy, Z. K. & Braatz, R. D. (2007). Distributional uncertainty analysis using power series and polynomial chaos expansions. *Journal of Process Control*, 17(3), 229–240.

Najm, H. N. (2009). Uncertainty quantification and polynomial chaos techniques in computational fluid dynamics. *Annual review of fluid mechanics*, 41, 35–52.

Neugebauer, F., Keller, N., Xu, H., Kober, C., Ploshikhin, V. et al. (2014). Simulation of selective laser melting using process specific layer based meshing. *Proc. Fraunhofer Direct Digital Manufacturing Conf.(DDMC 2014), Axel Demmer, Aachen, Germany*, pp. 297–302.

Ngo, T. D., Kashani, A., Imbalzano, G., Nguyen, K. T. & Hui, D. (2018). Additive manufacturing (3D printing): A review of materials, methods, applications and challenges. *Composites Part B: Engineering*, 143, 172–196.

Ning, J., Mirkoohi, E., Dong, Y., Sievers, D. E., Garmestani, H. & Liang, S. Y. (2019). Analytical modeling of 3D temperature distribution in selective laser melting of Ti-6Al-4V considering part boundary conditions. *Journal of Manufacturing Processes*, 44, 319–326.

Özel, T., Altay, A., Kaftanoğlu, B., Leach, R., Senin, N. & Donmez, A. (2020). Focus variation measurement and prediction of surface texture parameters using machine learning in laser powder bed fusion. *Journal of manufacturing science and engineering*, 142(1), 011008.

O'Hagan, A. et al. (2013). Polynomial chaos: A tutorial and critique from a statistician's perspective. *SIAM/ASA J. Uncertainty Quantification*, 20, 1–20.

Padhye, N. & Deb, K. (2011). Multi-objective optimisation and multi-criteria decision making in SLS using evolutionary approaches. *Rapid Prototyping Journal*.

Pal, D., Patil, N., Kutty, K. H., Zeng, K., Moreland, A., Hicks, A., Beeler, D. & Stucker, B. (2016). A generalized feed-forward dynamic adaptive mesh refinement and derefinement finite-element framework for metal laser sintering—Part II: Nonlinear thermal simulations and validations. *Journal of Manufacturing Science and Engineering*, 138(6).

Panwisawas, C., Qiu, C., Sovani, Y., Brooks, J., Attallah, M. & Basoalto, H. (2015). On the role of thermal fluid dynamics into the evolution of porosity during selective laser melting. *Scripta Materialia*, 105, 14–17.

Patil, N., Pal, D., Khalid Rafi, H., Zeng, K., Moreland, A., Hicks, A., Beeler, D. & Stucker, B. (2015). A generalized feed forward dynamic adaptive mesh refinement and derefinement finite element framework for metal laser sintering—part I: formulation and algorithm development. *Journal of Manufacturing Science and Engineering*, 137(4).

Pearson, K. (1901). LIII. On lines and planes of closest fit to systems of points in space. *The London, Edinburgh, and Dublin philosophical magazine and journal of science*, 2(11), 559–572.

Peligrad, A., Zhou, E., Morton, D. & Li, L. (2001). A melt depth prediction model for quality control of laser surface glazing of inhomogeneous materials. *Optics & Laser Technology*, 33(1), 7–13.

Phan, T. Q., Strantza, M., Hill, M. R., Gnaupel-Herold, T. H., Heigel, J., D'Elia, C. R., DeWald, A. T., Clausen, B., Pagan, D. C., Peter Ko, J. et al. (2019). Elastic residual strain and stress measurements and corresponding part deflections of 3D additive manufacturing builds of IN625 AM-bench artifacts using neutron diffraction, synchrotron X-ray diffraction, and contour method. *Integrating Materials and Manufacturing Innovation*, 8, 318–334.

Prabhakar, A., Fisher, J. & Bhattacharya, R. (2010). Polynomial chaos-based analysis of probabilistic uncertainty in hypersonic flight dynamics. *Journal of guidance, control, and dynamics*, 33(1), 222–234.

Qiu, C., Panwisawas, C., Ward, M., Basoalto, H. C., Brooks, J. W. & Attallah, M. M. (2015). On the role of melt flow into the surface structure and porosity development during selective laser melting. *Acta Materialia*, 96, 72–79.

Quarteroni, A., Rozza, G. et al. (2014). *Reduced order methods for modeling and computational reduction*. Springer.

Ravichander, B. B., Rahimzadeh, A., Farhang, B., Shayesteh Moghaddam, N., Amerinatanzi, A. & Mehrpouya, M. (2021). A Prediction Model for Additive Manufacturing of Inconel 718 Superalloy. *Applied Sciences*, 11(17), 8010.

Ravindran, S. S. (2000). A reduced-order approach for optimal control of fluids using proper orthogonal decomposition. *International journal for numerical methods in fluids*, 34(5), 425–448.

Razvi, S. S., Feng, S., Narayanan, A., Lee, Y.-T. T. & Witherell, P. (2019). A review of machine learning applications in additive manufacturing. *International design engineering technical conferences and computers and information in engineering conference*, 59179, V001T02A040.

Roberts, I. A., Wang, C., Esterlein, R., Stanford, M. & Mynors, D. (2009). A three-dimensional finite element analysis of the temperature field during laser melting of metal powders in additive layer manufacturing. *International Journal of Machine Tools and Manufacture*, 49(12-13), 916–923.

Rong-Ji, W., Xin-Hua, L., Qing-Ding, W. & Lingling, W. (2009). Optimizing process parameters for selective laser sintering based on neural network and genetic algorithm. *The International Journal of Advanced Manufacturing Technology*, 42, 1035–1042.

Salem, H., Carter, L., Attallah, M. & Salem, H. (2019). Influence of processing parameters on internal porosity and types of defects formed in Ti6Al4V lattice structure fabricated by selective laser melting. *Materials Science and Engineering: A*, 767, 138387.

Saliby, E. & Pacheco, F. (2002). An empirical evaluation of sampling methods in risk analysis simulation: quasi-Monte Carlo, descriptive sampling, and Latin hypercube sampling. *Proceedings of the winter simulation conference*, 2, 1606–1610.

Salonitis, K., Chantzis, D. & Kappatos, V. (2017). A hybrid finite element analysis and evolutionary computation method for the design of lightweight lattice components with optimized strut diameter. *The International Journal of Advanced Manufacturing Technology*, 90, 2689–2701.

Saltelli, A., Annoni, P., Azzini, I., Campolongo, F., Ratto, M. & Tarantola, S. (2010). Variance based sensitivity analysis of model output. Design and estimator for the total sensitivity index. *Computer physics communications*, 181(2), 259–270.

Samie Tootooni, M., Dsouza, A., Donovan, R., Rao, P. K., Kong, Z. & Borgesen, P. (2017). Classifying the dimensional variation in additive manufactured parts from laser-scanned three-dimensional point cloud data using machine learning approaches. *Journal of Manufacturing Science and Engineering*, 139(9), 091005.

Sankararaman, S., Ling, Y. & Mahadevan, S. (2011). Uncertainty quantification and model validation of fatigue crack growth prediction. *Engineering Fracture Mechanics*, 78(7), 1487–1504.

Schoinochoritis, B., Chantzis, D. & Salonitis, K. (2017). Simulation of metallic powder bed additive manufacturing processes with the finite element method: A critical review. *Proceedings of the Institution of Mechanical Engineers, Part B: Journal of Engineering Manufacture*, 231(1), 96–117.

Scime, L. & Beuth, J. (2018). A multi-scale convolutional neural network for autonomous anomaly detection and classification in a laser powder bed fusion additive manufacturing process. *Additive Manufacturing*, 24, 273–286.

Shen, X., Yao, J., Wang, Y. & Yang, J. (2004). Density prediction of selective laser sintering parts based on artificial neural network. *Advances in Neural Networks-ISNN 2004: International Symposium on Neural Networks, Dalian, China, August 19-21, 2004, Proceedings, Part II 1*, pp. 832–840.

Shen, Z., Shang, X., Zhao, M., Dong, X., Xiong, G. & Wang, F.-Y. (2019). A learning-based framework for error compensation in 3D printing. *IEEE transactions on cybernetics*, 49(11), 4042–4050.

Shevchik, S. A., Kenel, C., Leinenbach, C. & Wasmer, K. (2018). Acoustic emission for in situ quality monitoring in additive manufacturing using spectral convolutional neural networks. *Additive Manufacturing*, 21, 598–604.

Shi, Z., Mamun, A. A., Kan, C., Tian, W. & Liu, C. (2022). An LSTM-autoencoder based online side channel monitoring approach for cyber-physical attack detection in additive manufacturing. *Journal of Intelligent Manufacturing*, 1–17.

Siddalingappa, R. & Kanagaraj, S. (2021). Anomaly detection on medical images using autoencoder and convolutional neural network. *International Journal of Advanced Computer Science and Applications*, (7).

Singh, A. K. & Prakash, R. S. (2009). Simulation based two level factorial designed experiments for optimisation of selective laser sintering process. *International Journal of Computer Aided Engineering and Technology*, 1(3), 322–337.

Singh, G., Pal, M., Yadav, Y. & Singla, T. (2020). Deep neural network-based predictive modeling of road accidents. *Neural Computing and Applications*, 32, 12417–12426.

Singhal, S., Jain, P. K., Pandey, P. M. & Nagpal, A. (2009). Optimum part deposition orientation for multiple objectives in SL and SLS prototyping. *International journal of production research*, 47(22), 6375–6396.

Skoog, S. A., Goering, P. L. & Narayan, R. J. (2014). Stereolithography in tissue engineering. *Journal of Materials Science: Materials in Medicine*, 25, 845–856.

Smith, J., Xiong, W., Yan, W., Lin, S., Cheng, P., Kafka, O. L., Wagner, G. J., Cao, J. & Liu, W. K. (2016). Linking process, structure, property, and performance for metal-based additive manufacturing: computational approaches with experimental support. *Computational Mechanics*, 57, 583–610.

Srinivasan, S., Swick, B. & Groeber, M. A. (2020). Laser powder bed fusion parameter selection via machine-learning-augmented process modeling. *Jom*, 72, 4393–4403.

Storn, R. & Price, K. (1995). DE-a simple and efficient adaptive scheme for global optimization over continuous space. *Technical report*, 25(6), 95–102.

Storn, R. & Price, K. (1997). Differential evolution–a simple and efficient heuristic for global optimization over continuous spaces. *Journal of global optimization*, 11, 341–359.

Strano, G., Hao, L., Everson, R. M. & Evans, K. E. (2013). Surface roughness analysis, modelling and prediction in selective laser melting. *Journal of Materials Processing Technology*, 213(4), 589–597.

Sun, M.-s., Nelson, C., Beaman, J. J. & Barlow, J. J. (1991). A model for partial viscous sintering. *1991 International Solid Freeform Fabrication Symposium*.

Sun, X. & Choi, J.-I. (2021). Non-intrusive reduced-order modeling for uncertainty quantification of space–time-dependent parameterized problems. *Computers & Mathematics with Applications*, 87, 50–64.

Tan, Y., Jin, B., Nettekoven, A., Chen, Y., Yue, Y., Topcu, U. & Sangiovanni-Vincentelli, A. (2019). An encoder-decoder based approach for anomaly detection with application in additive manufacturing. *2019 18th IEEE international conference on machine learning and applications (ICMLA)*, pp. 1008–1015.

Tang, W., Vian, C. M., Tang, Z. & Yang, B. (2021). Anomaly detection of core failures in die casting X-ray inspection images using a convolutional autoencoder. *Machine Vision and Applications*, 32(4), 102.

Tapia, G., Elwany, A. H. & Sang, H. (2016). Prediction of porosity in metal-based additive manufacturing using spatial Gaussian process models. *Additive Manufacturing*, 12, 282–290.

Tapia, G. & Elwany, A. (2014). A review on process monitoring and control in metal-based additive manufacturing. *Journal of Manufacturing Science and Engineering*, 136(6), 060801.

Tapia, G., Khairallah, S., Matthews, M., King, W. E. & Elwany, A. (2018). Gaussian process-based surrogate modeling framework for process planning in laser powder-bed fusion additive manufacturing of 316L stainless steel. *The International Journal of Advanced Manufacturing Technology*, 94, 3591–3603.

Teng, C., Gong, H., Szabo, A., Dilip, J., Ashby, K., Zhang, S., Patil, N., Pal, D. & Stucker, B. (2017). Simulating melt pool shape and lack of fusion porosity for selective laser melting of cobalt chromium components. *Journal of Manufacturing Science and Engineering*, 139(1).

Thijs, L., Kempen, K., Kruth, J.-P. & Van Humbeeck, J. (2013). Fine-structured aluminium products with controllable texture by selective laser melting of pre-alloyed AlSi10Mg powder. *Acta Materialia*, 61(5), 1809–1819.

Tolochko, N. K., Arshinov, M. K., Gusarov, A. V., Titov, V. I., Laoui, T. & Froyen, L. (2003). Mechanisms of selective laser sintering and heat transfer in Ti powder. *Rapid prototyping journal*, 9(5), 314–326.

Tolosa, I., Garciandía, F., Zubiri, F., Zapirain, F. & Esnaola, A. (2010). Study of mechanical properties of AISI 316 stainless steel processed by “selective laser melting”, following different manufacturing strategies. *The International Journal of Advanced Manufacturing Technology*, 51, 639–647.

torey.liepa@nist.gov. [Last Modified: 2020-07-09T14:15-04:00]. Benchmark Test Data [text]. Retrieved on 2021-12-22 from: https://www.nist.gov/ambench/benchmark-test-data.

Tupac-Yupanqui, H. & Armani, A. (2021). Additive manufacturing of functional Inconel 718 parts from recycled materials. *Journal of Materials Engineering and Performance*, 30, 1177–1187.

Tveito, A. & Bruaset, A. M. (2006). *Numerical solution of partial differential equations on parallel computers*. Springer.

Unger, B. & Gugercin, S. (2019). Kolmogorov n-widths for linear dynamical systems. *Advances in Computational Mathematics*, 45(5-6), 2273–2286.

Wang, C., Tan, X., Tor, S. B. & Lim, C. (2020). Machine learning in additive manufacturing: State-of-the-art and perspectives. *Additive Manufacturing*, 36, 101538.

Wang, D., Yang, Y., Yi, Z. & Su, X. (2013). Research on the fabricating quality optimization of the overhanging surface in SLM process. *The International Journal of Advanced Manufacturing Technology*, 65, 1471–1484.

Wang, F. (2012). Mechanical property study on rapid additive layer manufacture Hastelloy® X alloy by selective laser melting technology. *The International Journal of Advanced Manufacturing Technology*, 58, 545–551.

Weinhold, B., Heck, B., Albright, A., Wang, K., Grote, J.-M., Adeniji, E., Masoomi, M. & Thompson, S. (2021). Simulation of the Laser-Powder Bed Fusion Process for Determining the Effects of Part-to-Substrate Location and Orientation on Distortion in a Connecting Rod. *2021 International Solid Freeform Fabrication Symposium*.

Weiss, J. A Tutorial on the Proper Orthogonal Decomposition. *AIAA Aviation 2019 Forum*. doi: 10.2514/6.2019-3333.

Weiss, J. (2019). A tutorial on the proper orthogonal decomposition. *AIAA aviation 2019 forum*, pp. 3333.

Wilson, P. & Mantooth, H. A. (2013). *Model-based engineering for complex electronic systems*. Newnes.

Wohler, T. (2013). Additive manufacturing and 3D printing—state of the industry annual worldwide progress report 2014, Wohler's associates. *Inc., Fort Collins, CO*.

Wu, A. S., Brown, D. W., Kumar, M., Gallegos, G. F. & King, W. E. (2014). An experimental investigation into additive manufacturing-induced residual stresses in 316L stainless steel. *Metallurgical and Materials Transactions A*, 45, 6260–6270.

Xiao, D., Fang, F., Pain, C. & Navon, I. (2017). A parameterized non-intrusive reduced order model and error analysis for general time-dependent nonlinear partial differential equations and its applications. *Computer Methods in Applied Mechanics and Engineering*, 317, 868–889.

Xiong, J., Zhang, G., Hu, J. & Wu, L. (2014). Bead geometry prediction for robotic GMAW-based rapid manufacturing through a neural network and a second-order regression analysis. *Journal of Intelligent Manufacturing*, 25, 157–163.

Yagi, S. & Kunii, D. (1957). Studies on effective thermal conductivities in packed beds. *AIChE Journal*, 3(3), 373–381.

Yang, H.-J., Hwang, P.-J. & Lee, S.-H. (2002). A study on shrinkage compensation of the SLS process by using the Taguchi method. *International Journal of Machine Tools and Manufacture*, 42(11), 1203–1212.

Yang, Y., Knol, M., Van Keulen, F. & Ayas, C. (2018). A semi-analytical thermal modelling approach for selective laser melting. *Additive Manufacturing*, 21, 284–297.

Yang, Y. & Ayas, C. (2017). Point, surface and volumetric heat sources in the thermal modelling of selective laser melting. *AIP conference proceedings*, 1896(1).

Yap, C. Y., Chua, C. K., Dong, Z. L., Liu, Z. H., Zhang, D. Q., Loh, L. E. & Sing, S. L. (2015). Review of selective laser melting: Materials and applications. *Applied physics reviews*, 2(4).

Ye, D., Hong, G. S., Zhang, Y., Zhu, K. & Fuh, J. Y. H. (2018). Defect detection in selective laser melting technology by acoustic signals with deep belief networks. *The International Journal of Advanced Manufacturing Technology*, 96, 2791–2801.

Yin, J., Zhu, H., Ke, L., Lei, W., Dai, C. & Zuo, D. (2012). Simulation of temperature distribution in single metallic powder layer for laser micro-sintering. *Computational Materials Science*, 53(1), 333–339.

Zaeh, M. F. & Branner, G. (2010). Investigations on residual stresses and deformations in selective laser melting. *Production Engineering*, 4(1), 35–45.

Zäh, M. F. & Lutzmann, S. (2010). Modelling and simulation of electron beam melting. *Production Engineering*, 4(1), 15–23.

Zhang, B., Li, Y. & Bai, Q. (2017). Defect formation mechanisms in selective laser melting: a review. *Chinese Journal of Mechanical Engineering*, 30, 515–527.

Zhang, B., Liu, S. & Shin, Y. C. (2019a). In-Process monitoring of porosity during laser additive manufacturing process. *Additive Manufacturing*, 28, 497–505.

Zhang, J., Li, D., Li, J. & Zhao, L. (2011). Numerical simulation of temperature field in selective laser sintering. *Computer and Computing Technologies in Agriculture IV: 4th IFIP TC 12 Conference, CCTA 2010, Nanchang, China, October 22-25, 2010, Selected Papers, Part IV 4*, pp. 474–479.

Zhang, J., Wang, P. & Gao, R. X. (2019b). Deep learning-based tensile strength prediction in fused deposition modeling. *Computers in industry*, 107, 11–21.

Zhang, Y., Harik, R., Fadel, G. & Bernard, A. (2018a). A statistical method for build orientation determination in additive manufacturing. *Rapid Prototyping Journal*, 25(1), 187–207.

Zhang, Y., Yang, S., Dong, G. & Zhao, Y. F. (2021). Predictive manufacturability assessment system for laser powder bed fusion based on a hybrid machine learning model. *Additive Manufacturing*, 41, 101946.

Zhang, Y., Hong, G. S., Ye, D., Zhu, K. & Fuh, J. Y. (2018b). Extraction and evaluation of melt pool, plume and spatter information for powder-bed fusion AM process monitoring. *Materials & Design*, 156, 458–469.

Zhao, X., An, N., Yang, G., Wang, J., Tang, H., Li, M. & Zhou, J. (2021). Enhancing standard finite element codes with POD for reduced order thermal analysis: Application to electron beam melting of pure tungsten. *Materials Today Communications*, 29, 102796.

Zhu, J., Shi, H., Song, B., Tan, S. & Tao, Y. (2020a). Deep neural network based recursive feature learning for nonlinear dynamic process monitoring. *The Canadian Journal of Chemical Engineering*, 98(4), 919–933.

Zhu, J., Shi, H., Song, B., Tao, Y. & Tan, S. (2020b). Information concentrated variational auto-encoder for quality-related nonlinear process monitoring. *Journal of Process Control*, 94, 12–25.

Zhu, Z., Anwer, N., Huang, Q. & Mathieu, L. (2018). Machine learning in tolerancing for additive manufacturing. *CIRP annals*, 67(1), 157–160.

Ziaee, M. & Crane, N. B. (2019). Binder jetting: A review of process, materials, and methods. *Additive Manufacturing*, 28, 781–801.

Zouhri, W., Dantan, J.-Y., Häfner, B., Eschner, N., Homri, L., Lanza, G., Theile, O. & Schäfer, M. (2021). Characterization of laser powder bed fusion (L-PBF) process quality: A novel approach based on statistical features extraction and support vector machine. *Procedia CIRP*, 99, 319–324.